9-1-2020

MARKET-CONSCIOUS STRATEGIES TO IMPROVE THE PERFORMANCE AND STABILITY OF PLANAR, p-i-n HYBRID ORGANIC-INORGANIC METAL HALIDE PEROVSKITE SOLAR CELLS

Brandon Dunham
University of Massachusetts Amherst

MARKET-CONSCIOUS STRATEGIES TO IMPROVE THE PERFORMANCE AND STABILITY OF PLANAR, p-i-n HYBRID ORGANIC-INORGANIC METAL HALIDE PEROVSKITE SOLAR CELLS

A Dissertation Presented

by

BRANDON JAMES DUNHAM

Submitted to the Graduate School of the

University of Massachusetts Amherst in partial fulfillment

of the requirements for the degree of

DOCTOR OF PHILOSOPHY

September 2020

Chemical Engineering

MARKET-CONSCIOUS STRATEGIES TO IMPROVE THE PERFORMANCE AND STABILITY OF PLANAR, p-i-n HYBRID ORGANIC-INORGANIC METAL HALIDE PEROVSKITE SOLAR CELLS

A Dissertation Presented

by

BRANDON JAMES DUNHAM

Approved as to style and content by:

_____
Christos Dimitrakopoulos, Chair

_____
Dimitrios Maroudas, Member

_____
Dhandapani Venkataraman, Member

_____
John Klier, Department Head
Chemical Engineering

DEDICATION

To my patient and loving wife, Nicole.

ACKNOWLEDGMENTS

This work was supported in part by Federal Award No.: W911NF15-2-0026//Army Research Office and by a Graduate School Predissertation Research Grant from the University of Massachusetts Amherst. Device fabrication and characterization were performed in the Laboratory for Electronic Materials and Devices of the Institute for Applied Life Sciences at the University of Massachusetts Amherst. I acknowledge the use of instrumentation at the Polymer W.M. Keck Electron Microscopy, Mass Spectrometry, and X-Ray Scattering facilities, under the umbrella of the Institute for Applied Life Sciences at the University of Massachusetts Amherst.

I would like to thank Dr. Jun Yan and his research group for their help with graphene characterization via Raman spectroscopy; Dr. Todd Emrick and his research group for providing the C_{60}-N cathode interlayer for Chapter 5 of this study; Dr. Volodimyr Duzhko for his help with device fabrication and characterization instrument training; Dr. Steven Eyles for his assistance with Inductively Coupled Plasma Mass Spectroscopy; the Venkataraman research group for their help with perovskite-related characterization; and Dr. Alexander Ribbe, Lou Raboin, and Dr. Vivek Vattipalli for their help and guidance with Scanning Electron Microscopy.

Lastly, I would like to extend a special thanks to my advisor, Dr. Christos Dimitrakopoulos; to my committee members, Dr. Dhandapani Venkataraman and Dr. Dimitrios Maroudas; to the faculty and staff in UMass Chemical Engineering Department; and to my family and friends, especially my wife, Nicole. I could not have done this without the endless encouragement, support, and ideas that each and every one of them offered me throughout this entire doctoral journey.

ABSTRACT

MARKET-CONSCIOUS STRATEGIES TO IMPROVE THE PERFORMANCE AND STABILITY OF PLANAR, p-i-n HYBRID ORGANIC-INORGANIC METAL HALIDE PEROVSKITE SOLAR CELLS

SEPTEMBER 2020

BRANDON JAMES DUNHAM

B.A. CHEMISTRY, STONEHILL COLLEGE

B.S. CHEMICAL ENGINEERING, UNIVERSITY OF NOTRE DAME

Ph.D. CHEMICAL ENGINEERING, UNIVERSITY OF MASSACHUSETTS AMHERST

Directed by: Professor Christos Dimitrakopoulos

Planar, p-i-n (inverted) hybrid organic-inorganic perovskite solar cells that use low-temperature, solution-processable charge-transport layers have garnered much attention due to their direct compatibility with flexible substrates and cost-effective roll-to-roll manufacturing. Nevertheless, this architecture has failed to repeatedly achieve the superior power conversion efficiencies frequently attained by its n-i-p counterpart. Additionally, the perovskite active layer has poor stability in the presence of prolonged light exposure, high temperatures, and moisture. In this study, we propose commercially viable strategies to improve the performance and stability of inverted methylammonium lead iodide perovskite solar cells. First, we show that a simple two-step method comprising evaporation-induced self-assembly of a lead iodide intermediate film coupled with the intermolecular exchange of methylammonium iodide can yield high-quality methylammonium lead iodide perovskite films on non-ideal surfaces. Complete inverted devices with the perovskite active layer formed via this method outperformed those devices with a perovskite layer produced using a conventional method. Second, we successfully replace the commonly used but environmentally unstable calcium-aluminum electrode with a more stable silver electrode in inverted perovskite devices via interfacial engineering without compromising device performance. By introducing a solution-processable, thickness-tolerant n-doped zwitterionic fulleropyrrolidine interlayer between the phenyl-C61-butyric acid methyl ester electron-transporting layer and the silver electrode, we successfully lower the work function of the silver and improve charge transport, which led to an increase in device performance compared to those devices with a calcium-aluminum electrode. Third, we examine the use of copper-based hole-transport materials in inverted perovskite solar cells as a replacement for the more commonly used but less stable poly(3,4-ethylenedioxythiophene) polystyrene sulfonate hole-transport material. We show that in

most cases devices with a copper-based hole-transport material outperform those with a poly(3,4-ethylenedioxythiophene) polystyrene sulfonate hole-transport material due to the additive benefits from all relevant film/material properties (i.e. morphology, optics, crystallinity/charge transport potential, and electronic band level alignment). Finally, we present a procedure to effectively transfer monolayer CVD graphene onto a perovskite surface without damaging or degrading the perovskite. We show that the incorporation of graphene significantly improves perovskite film and inverted device stability in the presence of moisture and heat without sacrificing the overall device performance.

TABLE OF CONTENTS

Page

LIST OF TABLES

Table Page

LIST OF FIGURES

Figure Page

CHAPTER 1

SOLAR ENERGY: MOTIVATION AND HISTORY

1.1 Global Warming and Climate Change

When fossil fuels such as coal and oil are burned at an unsustainable rate, the emitted greenhouse gases (e.g. carbon dioxide, CO_2) accumulate in the atmosphere. As the concentration of greenhouse gases in the atmosphere increases, it becomes progressively more difficult for heat radiated from the Earth's surface to escape into space, which causes the average temperature of the planet to rise. This phenomenon, referred to as Global Warming, is a direct cause of Climate Change, one of the greatest threats the world faces today. According to the Mauna Loa Observatory, the atmospheric CO_2 concentration has already exceeded 400 ppm (Figure 1).[1]

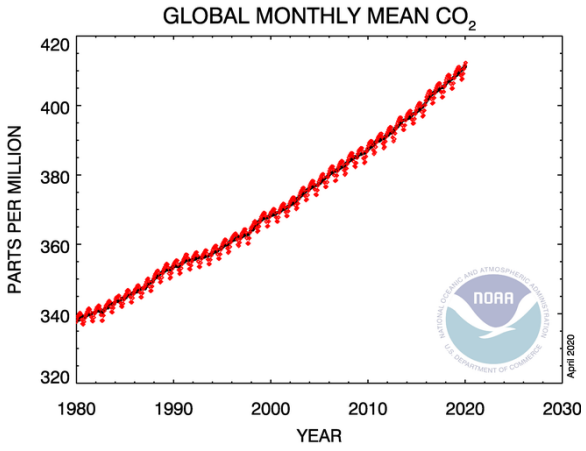

Figure 1. Global monthly mean atmospheric CO_2 since 1980. As of January 2020, the average atmospheric CO_2 level was 412.3 ppm. Reproduced from Reference [1].

In order to help avoid any further progression of Climate Change, the world must look to adopt renewable sources of energy that emit fewer to no greenhouse gases into the atmosphere when used.

1.2 World Energy Demand

As the world population continues to increase, so too does the amount of energy used. An overview of the sources of energy used and the amount of power each source supplies is given in Figure 2. The world currently consumes around 16 TW of energy[2], and it is estimated that this number will increase nearly 30% by 2040.[3] To meet this increase in demand, the world must find additional large scale, affordable, and, preferably, sustainable energy sources. The radiation from the sun supplies about 23,000 TW of power to the Earth[2], making it an efficient and feasible energy source to harvest and convert to electrical energy. While it is not possible to collect all this energy, photovoltaic (PV) technology like solar cells, which harvest and convert sunlight to electricity, are still a very viable alternative to help meet the world energy demand.

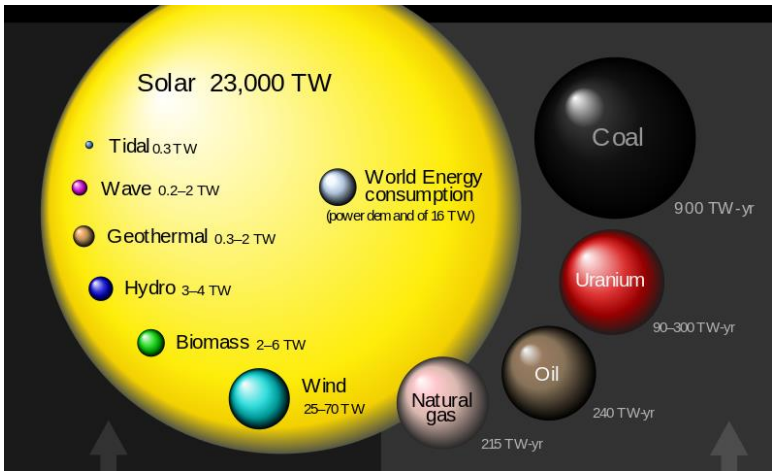

Figure 2. Available power from various renewable and nonrenewable energy sources. Also shown is the approximate world energy demand. Reproduced from Reference [2].

1.3 Brief Photovoltaic Technology Review

Current PV technology can be divided into three main categories: first generation solar cells, second generation solar cells, and third generation solar cells. First generation solar cells are those comprised of crystalline silicon (monocrystalline or polycrystalline).

Originally invented by Bell Labs in 1954 for use in satellites[4], silicon-based solar cells eventually emerged as the dominate technology in the commercial solar market (and continue to be so) due to their exceptional ambient stability and sunlight-to-electricity power conversion efficiency (PCE). According to the National Renewable Energy Laboratory (NREL), laboratory-scale monocrystalline and polycrystalline silicon solar cells have achieved PCEs of 26.1-26.6% and 22.3%, respectively.[5] A chart listing the best certified efficiencies for laboratory scale solar cells is given in Figure 3.

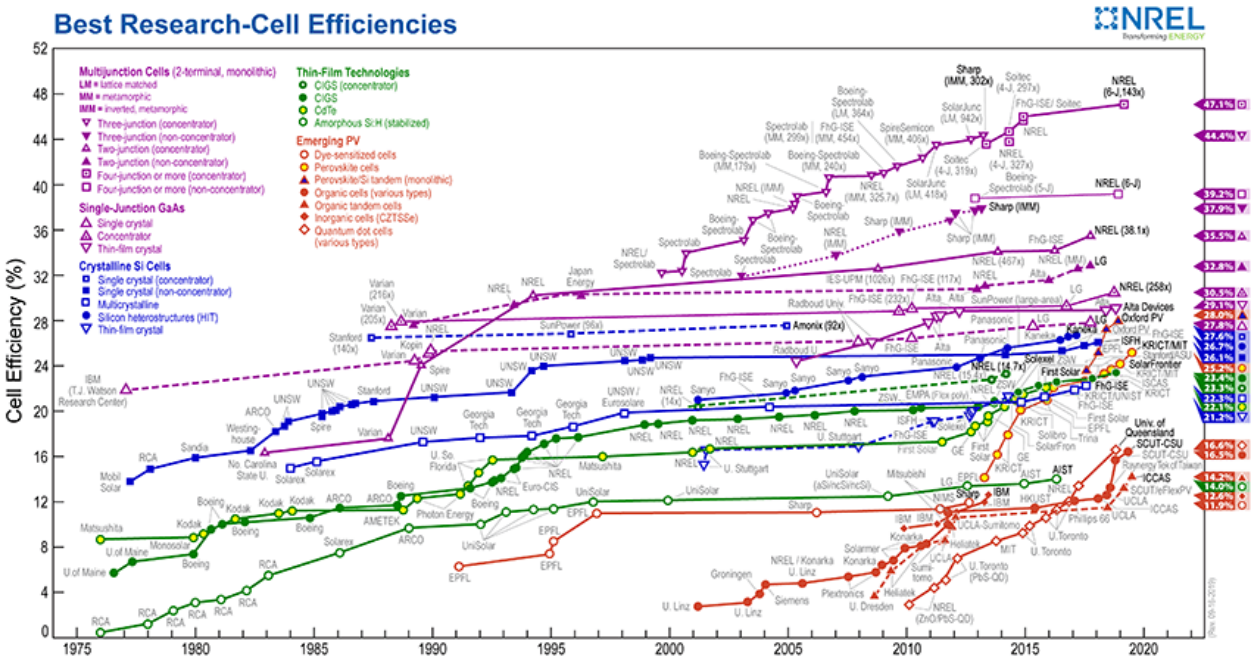

Figure 3. The highest certified PCEs for laboratory-scale solar cells for a range of photovoltaic technologies from 1976 to the present. Reproduced from Reference [5].

Under thermodynamic consideration of detailed balance, in the absence of nonradiative recombination, the theoretical maximum PCE for a single-junction solar cell is 33.7% for AM1.5G solar spectrum at 25 °C.[6] This value is known as the Shockley–Queisser limit. Despite their remarkable history, though, silicon-based solar cells still suffer from high costs of production.[7]

Second generation solar cells are made up of different semiconducting thin film technologies such as gallium arsenide (GaAs), cadmium telluride (CdTe), copper indium gallium selenide (CIGS), and amorphous silicon (a-Si). The maximum laboratory-scale single-junction PCEs that have been achieved for these four technologies are 27.8-30.5% (GaAs), 22.1% (CdTe), 22.9-23.3% (CIGS), and 14% (a-Si), making them competitive with crystalline silicon PVs.[5] Second generation solar cells have also found a niche in multi-junction tandem architectures, achieving efficiencies above the Shockley–Queisser limit due to the presence of multiple absorbing layers capable of harvesting light from different regions of the solar spectrum. Nevertheless, these thin film solar technologies also suffer from high production costs as well as another issue, toxicity, which have delayed their inclusion into the current commercial solar market.[7]

In an effort to lower the production costs of solar cells, scientists began investigating light-absorbing materials that could be processed at low temperatures and from solution, which would make them compatible with large-scale roll-to-roll, inkjet printing, and slot-die coating manufacturing. These emerging PV technologies, referred to as third generation solar cells, include dye-sensitized solar cells (DSSC), organic photovoltaics (OPV), quantum-dot solar cells (QDSC), and perovskite solar cells (PSC). While initial PCEs for these technologies were much lower than those of silicon PVs, their low-cost and potential for production on flexible substrates made them appealing research options. Today, DSSCs, OPVs, QDSCs, and PSCs have achieved maximum certified laboratory-scale PCEs of 11.9%, 15.6%, 16.6%, and 25.2%, respectively.[5] Of these, PSCs show a great deal of promise as they can achieve efficiencies competitive with those of first and second generation solar cells, but with a much lower production cost. They have also found a role

in flexible solar cells and tandem geometries with silicon and CIGS.[7,8] The wide range of possible applications for PSCs have made them one of the most researched PV technologies of today; however, until toxicity and stability issues with single-junction PSCs are resolved, it may be some time before they are market-ready.

CHAPTER 2

PEROVSKITE PHOTOVOLTAICS: AN OVERVIEW

2.1 Introduction to Perovskites

Perovskites are a class of material that adopt the three-dimensional (3D) cubic ABX_3 crystal structure (e.g. calcium titanate, $CaTiO_3$), where the A cation is surrounded by corner-sharing BX_6 octahedra.[9] When A is an organic cation, B a divalent transition metal, and X a halide, the material is referred to as a hybrid organic-inorganic metal halide perovskite, or simply hybrid perovskite (Figure 4).[10]

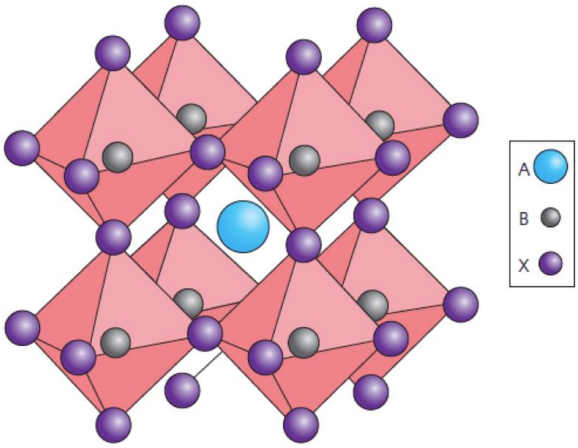

Figure 4. Cubic ABX_3 crystal structure for a hybrid perovskite. Reproduced from Reference [10].

For the 3D perovskite structure to be realized, the crystal must maintain a tolerance factor in the range of 0.8-1.0. The tolerance factor, *t*, is defined as:

$$t = \frac{R_A + R_X}{\sqrt{2}(R_B + R_X)} \qquad \text{Equation 1}$$

where R_A, R_B, and R_X are the ionic radii of the organic cation, divalent transition metal, and halide, respectively.[11,12] In the case where the organic cation is too large, then $t > 1.0$, and the perovskite material adopts the two-dimensional (2D) layered A_2BX_4 crystal structure (Figure 5).[13]

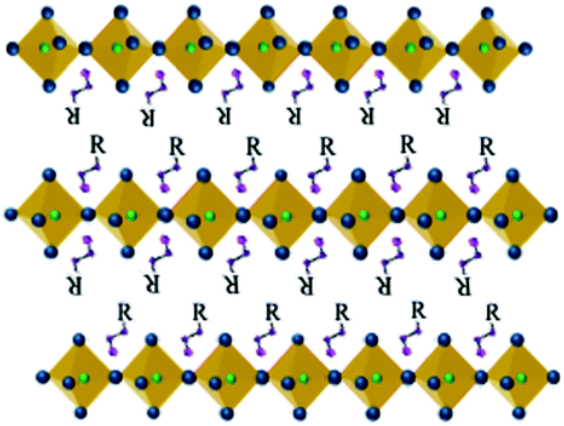

Figure 5. Layered A_2BX_4 (2D) hybrid perovskite crystal structure. Reproduced from Reference [13].

The layered hybrid perovskite structure was of particular interest to Mitzi and co-workers in the early 1990s, who investigated the optoelectric and semiconducting properties of these materials in light-emitting diodes (LEDs) and field-effect transistors (FETs).[14–17] However, no solar cell research was performed, possibly because investigative focus at this time was on layered excitonic materials.[18]

2.2 Perovskite Photovoltaics History

Mitzi and co-workers were some of the first to use hybrid perovskites in organic LEDs and FETs in the 1990s due to their strong room-temperature photoluminescence, high carrier mobility, and excellent solution processability.[14–17,19] Almost two decades later, in 2009, Miyasaka and co-workers used the 3D perovskite analogues, methylammonium lead bromide ($MAPbBr_3$) and methylammonium lead iodide ($MAPbI_3$), as sensitizers on the titanium dioxide (TiO_2) layer in a DSSC, achieving a maximum PCE of 3.81%.[20] Soon after, Park *et al.* used a similar device architecture, but with a thinner TiO_2 layer, and reported a PCE of 6.5%.[21] These were two of the first instances where hybrid perovskites

were used in solar cells; however, the perovskite-based DSSC exhibited poor operational stability as the perovskite absorber was found to quickly degrade in the redox electrolyte. It was not until 2012 that the first successful attempts at avoiding the dissolution of the perovskite in the liquid electrolyte came. By replacing the liquid electrolyte with a solid hole transport material (HTM), the first solid-state PSCs using cesium tin iodide/dye N719[22] and $MAPbI_3$/spiro-OMeTAD were developed. Not only did the addition of the solid HTM improve stability, but it also enhanced the PCE of these devices up to 11%.[23] Since then, optimization of the charge transport layers, perovskite absorber layer, and perovskite film deposition techniques of PSCs has led to a recent outstanding NREL-certified PCE of 25.2%.[5]

2.3 Properties of Hybrid Organic-Inorganic Halide Perovskites

2.3.1 Low Exciton Binding Energy

An exciton is a bound electron-hole pair that is formed when a semiconductor (e.g. the perovskite) absorbs a photon of higher energy than its bandgap, thus exciting an electron to the conduction band from the valence band (where a hole is left behind). The exciton binding energy is hence the minimum energy required to dissociate the exciton into free charge carriers.[24] For photovoltaic materials, low exciton binding energies that allow for room temperature dissociation are often ideal. The system in which the dissociation occurs can be excitonic or non-excitonic in nature. For excitonic dissociation an n- and p-type heterojunction interface (such as that in organic or polymer solar cells) is required. Conversely, for non-excitonic dissociation, the photoexcited electron-hole pair will spontaneously separate into free carriers in the bulk material (such as in inorganic solar

cells). Hybrid organic-inorganic halide perovskite films have been shown to be predominantly non-excitonic in nature, possessing exciton binding energies less than 50 meV, which allows for room temperature dissociation.[25]

2.3.2 High Absorption Coefficient

The absorption coefficient of a semiconductor determines how far a particular wavelength of light penetrates the material before it is absorbed. The absorption coefficient is not constant; it depends strongly on the wavelength and varies between materials. If the absorption coefficient is low, the light will have a higher penetration depth, and the material will not absorb the light very effectively. In fact, if the light penetration depth provided by the absorption coefficient is greater than the thickness of the material, the material may even appear transparent to that particular wavelength of light. On the other hand, materials with high absorption coefficients absorb light more readily. Provided that the photon energy is higher than the bandgap of the semiconductor, and that the wavelength of light is in the absorption spectrum range of the semiconductor, then as the energy of the photon increases, the higher the probability of its absorption. The reason for this is that in this case more electrons (not just those with energy close to the bandgap) are able to interact with the photon to induce absorption.[26] Hybrid organic-inorganic halide perovskites have high absorption coefficients (on the order of 10^4-10^5 cm^{-1} for wavelengths within the visible spectrum of 400 – 750 nm for $MAPbI_3$). As a result, maximum penetration depths are around 500 nm; therefore, most incoming light can be absorbed by the perovskite material within a thin layer of about 500 nm.[27]

2.3.3 Tunable Bandgap

Hybrid organic-inorganic metal halide perovskites have the unique property of bandgap tunability depending on the combination of small organic cation(s), divalent metal(s), and halide(s) used.[28] $MAPbI_3$ has a band gap of around 1.54 eV (typically reported between 1.5 and 1.6 eV), which corresponds to an absorption wavelength around 800 nm.[29,30] By replacing the methylammonium (MA, $CH_3NH_3^+$) cation with a larger organic cation (continuing to keep the tolerance factor between 0.8 and 1.0) such as formamidinium (FA, $CH(NH_2)_2^+$), the metal(M)-halide(X)-metal(M) bond angles and lengths are modified. This modification leads to a distortion in the 3D perovskite lattice, causing a shift in structure from tetragonal to trigonal. As a result, the band gap is decreased to around 1.48 eV (typically reported between 1.4 and 1.5 eV for FA-substituted perovskites), and the absorption wavelength increases to around 840 nm. Another strategy that can be used to tune the bandgap is through replacing the Pb^{+2} metal cation with another divalent metal cation, such as Sn^{+2}. This change results in a direct modification of the M-X bond, causing a shift in the metal p and halide s bonding and antibonding orbitals of the valence band maxima (VBM) and conduction band minima (CBM); that is, the positions of the VBM and CBM are shifted. As a result, replacing Pb^{+2} with Sn^{+2} causes the bandgap to decrease to about 1.2 eV. A final strategy to modify the perovskite bandgap involves replacing or mixing halides.[30] For example, Eperon *et al.* reported that a mixed halide $FAPbI_xBr_{3-x}$ could have a bandgap between 1.48 eV (x = 3) and 2.23 eV (x = 0) depending on the ratio of I^- to Br^-.[31] The increase in Br^- content leads to an increase in the perovskite bandgap (decrease in absorption wavelength) due to a shift in the lattice structure from tetragonal/trigonal to cubic since the size of the Br^- anion is smaller than that of I^-.[31]

Bandgap tunability is a very important property of hybrid organic-inorganic halide perovskites not only to push closer to the optimal bandgap (~1.34 eV) based on the Shockley–Queisser limit for a single-junction solar cell,[6] but also to enable these materials to be utilized in various tandem architectures (e.g. perovskite-perovskite or perovskite-silicon tandems).

2.3.4 Ambipolar Charge Carrier Transport

The ability not only to absorb photons, but also to transport charge carriers (either holes, electrons, or both) is a highly desired property of solar cell active layers, but it is very rare that a material is naturally capable of doing both. Often times, doping of the absorbing layer (as in inorganic solar cells) or using a heterojunction absorbing layer sandwiched between hole- and electron-transporting layers (as in organic or polymer solar cells) is required to achieve such a result. Nevertheless, hybrid organic-inorganic halide perovskites do possess this unique dual-functionality. Lee *et al.* replaced the electron-transporting TiO_2 scaffold with an insulating Al_2O_3 scaffold in a mesosuperstructured perovskite solar cell architecture and found that the perovskite absorber alone was able to transport electrons to the bottom transparent conductive oxide electrode.[23] This showed that a thick TiO_2 scaffold with perovskite sensitizers (the DSSC-based architecture) was no longer necessary.[32] Later, Etgar *et al.* removed the solid hole-transporting material in a mesosuperstructured architecture and embedded the perovskite absorber within the TiO_2 scaffold. Remarkably, it was observed that the perovskite absorber alone was also able to transport holes to the top metal electron.[33] As a material capable of transporting both electrons and holes, it

became apparent that perovskite absorbers could be used in simple, cost-effective planar (n-i-p or p-i-n) solar cell configurations.

2.3.5 Long and Balanced Electron and Hole Diffusion Lengths

For efficient charge extraction, charge carrier diffusion lengths must be greater than the thickness of the charge transporting layer. This ensures that more free carriers may be transported before any electron-hole pairs recombine. Therefore, for the perovskite absorbing layer to function efficiently as an electron and hole transporter in a solar cell (especially in a planar configuration), its electron and hole diffusion lengths should be greater than its thickness. Additionally, to function equally in both an n-i-p as well as a p-i-n architecture, the perovskite should have balanced electron and hole diffusion lengths.[34] Stranks *et al.* used transient absorption and photoluminescence (PL) spectroscopy to determine the average electron and hole diffusion lengths in a $MAPbI_3$ perovskite to be on the order of 1 μm for each.[35] These results confirmed that the perovskite absorber could not only transport charges for efficient extraction, but also that mesosuperstructured perovskite solar cell architectures were not entirely necessary as the perovskite could function effectively in a planar system.

2.4 Perovskite Solar Cell Architectures

The first hybrid perovskite-based solar cells employed the perovskite material as sensitizers affixed to the TiO_2 scaffold of a Grätzel cell, or DSSC, architecture (Figure 6a,b).[20,21]

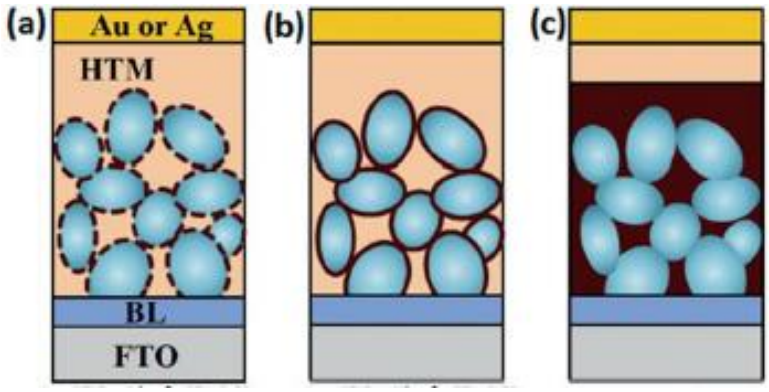

Figure 6. PSC architectures with (a) perovskite quantum dots on TiO_2, (b) extremely thin film perovskite sensitizers on TiO_2, and (c) meso-superstructured perovskite (bulk perovskite surrounding a mesoporous TiO_2 scaffold). Reproduced from Reference [36].[36]

Once the perovskite material was found to degrade in liquid redox electrolytes, however, the sensitized PSC adopted a solid hole transport material (HTM), 2,2',7,7'-Tetrakis[N,N-di(4-methoxyphenyl)amino]-9,9'-spirobifluorene (spiro-OMeTAD). When the ambipolar charge transporting ability of the hybrid perovskite absorber was revealed by replacing the conducting TiO_2 scaffold with an insulting mesoporous alumina (Al_2O_3) layer,[23,32] the PSC evolved to a meso-superstructured architecture (Figure 6c). Since then, PSCs have been fabricated in a wide variety of architectures determined by charge (p- or n-type) and morphology (mesostructured or planar), making it planar or mesostructured n-i-p (regular) (Figure 7a,b), p-i-n (inverted) (Figure 7 b,c), or n-p or p-n (Figure 8).

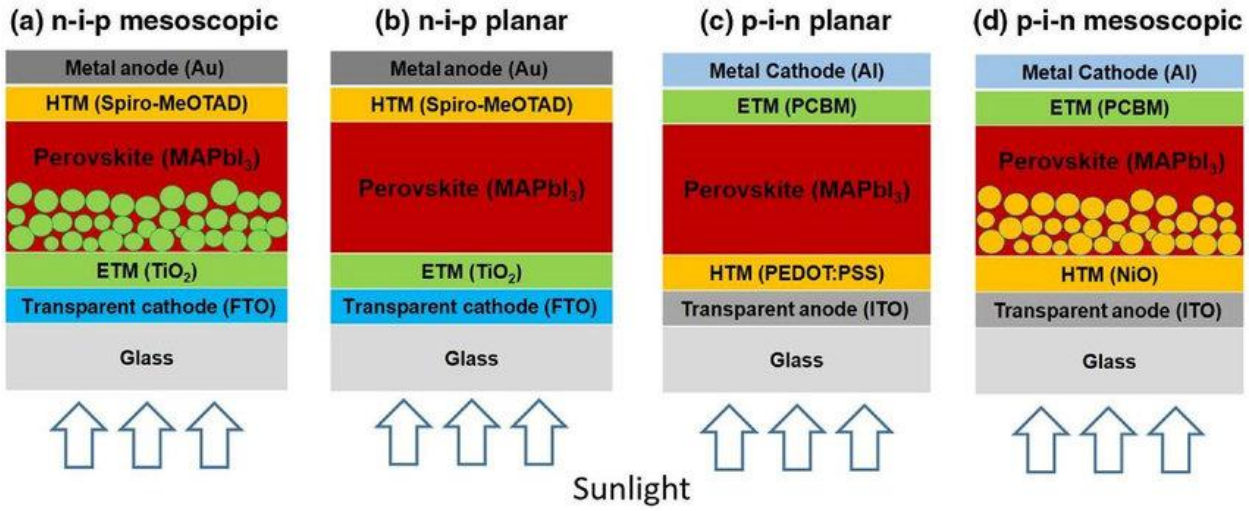

Figure 7. Typical planar and mesoscopic, n-i-p and p-i-n PSC architectures. Reproduced from Reference [37].[37]

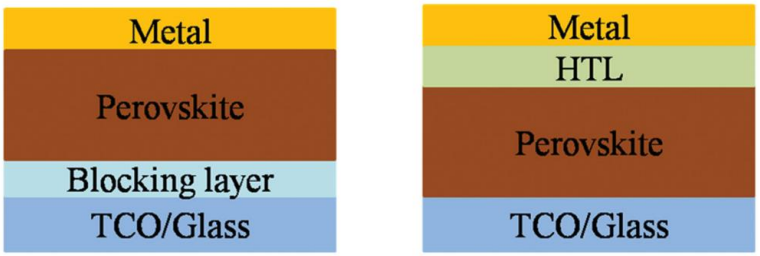

Figure 8. Hole-transport layer-free (left) and electron-transport layer-free (right) PSC architectures. Reproduced from Reference [38].[38]

2.4.1 Regular, n-i-p Architectures

Regular PSCs are those that employ the perovskite absorber between an electron transporting layer (ETL) such as TiO_2 on a transparent conducting substrate (e.g. FTO) and a hole transporting layer (ETL) such as spiro-OMeTAD with a metal back contact (e.g. gold, Au). These devices can be planar, with a thin film perovskite layer sandwiched between the ETL and HTL, or meso-superstructured, with an additional mesoporous conducting (TiO_2) or insulating (Al_2O_3) metal oxide that has been infiltrated with and capped by the perovskite absorber. The regular meso-superstructured architecture with

mesoporous TiO_2 currently holds the record certified PCE of 25.2% for a laboratory-scale PSC.[5] Nevertheless, despite the high performance of regular PSCs, the high temperature (>500 °C) annealing required to effectively calcine the TiO_2 layers is costly, increases processing time, and is not conducive to flexible substrates or roll-to-roll processing.[39] Additionally, the regular planar n-i-p architecture has been shown to suffer from current-voltage hysteresis.[40,41] These drawbacks limit this architecture's commercial viability.

2.4.2 Inverted, p-i-n Architectures

First reported by Jeng *et al.* in 2013, the inverted PSC adopts the structure of bulk-heterojunction (BHJ) organic or polymer solar cells, where a mixed electron-donor polymer and electron-acceptor fullerene (typically [6,6]-phenyl-C_{61}-butyric acid methyl ester, PCBM) layer acts as the absorber and is sandwiched between a polymer HTL (typically Poly(3,4-ethylenedioxythiophene)-poly(styrenesulfonate), PEDOT:PSS) on a transparent conducting substrate (i.e. ITO) and a metal back contact (aluminum, Al, or silver, Ag).[42] For the inverted PSC, however, the BHJ is replaced by a planar-heterojunction (PHJ) of perovskite/fullerene. Unlike the regular planar n-i-p architecture, the inverted planar p-i-n architecture exhibits negligible hysteresis behavior, likely due to the passivation of grain boundary trap states by the fullerene ETL.[43] The inverted architecture is often planar in make-up, but there have been reports of meso-superstructured architectures employing a mesoporous nickel oxide (NiO) layer.[44] While the highest reported PCEs of inverted PSCs are less than 21%, all processing temperatures are sub-150 °C, which decreases cost and processing time as well as makes them compatible with flexible substrates and roll-to-roll manufacturing.[45,46] Unfortunately, though this

architecture shows commercial viability and versatility, the performance must be improved to be competitive with that of the regular PSC architecture.

2.4.3 Hole- or Electron-Transporting Layer Free Architectures

Due to the excellent ambipolar charge transporting ability of hybrid perovskites, there have been reports of devices employing ETL(HTL)/perovskite or perovskite/HTL(ETL) architectures, where one of the charge-transporting layers has been removed.[33,47,48] While this design improves the simplicity of fabrication and may decrease processing time/cost, the maximum reported PCEs (though respectable) are not competitive with those devices that use both charge-transporting layers.

2.5 Perovskite Solar Cell Working Principle

Upon the absorption of photons by the perovskite active layer, free charge carriers are quickly generated due to the low exciton binding energy of the perovskite absorber. The photon-induced charge carrier generation rate, *G*, can be expressed as

$$G = IPCE \times I_0 \qquad \text{Equation 2}$$

where *IPCE* is the Incident Photon-to-Current Efficiency and I_0 is the incident light density. It is generally reasonable to assume that *G* is uniform in the perovskite layer.

Once generated, the free carriers (electrons and holes) are then transported to their respective interface contacts (electrons are transported from the perovskite absorber to the ETL, as well as then from the HTL to the perovskite absorber). If hole density is *p* and electron density is *n*, then the current induced by electrons and holes, $J_{i\,=\,p,\,n} = J_{diffusion} + J_{drift}$, can be expressed as

$$J_p = -eD_p \frac{\partial p}{\partial x} + ep\mu_p E \qquad \text{Equation 3}$$

$$J_n = eD_n \frac{\partial n}{\partial x} + en\mu_n E \qquad \text{Equation 4}$$

where e is the elementary charge, D_i (i = p, n) is the diffusion coefficient for holes or electrons, μ_i (i = p, n) is the charge carrier mobility for holes or electrons, and E is the magnitude of the electric field. The charge carrier mobilities are related to the diffusion coefficients via the Einstein Relation

$$D_i = \frac{\mu_i k_B T}{e} \qquad \text{Equation 5}$$

where k_B is Boltzmann's constant and T is temperature, whereas E is determined using Poisson's equation for an electric field

$$\frac{\partial E}{\partial x} = \frac{e(p-n)}{\varepsilon_r \varepsilon_0} \qquad \text{Equation 6}$$

where ε_r is the relative permittivity of the material and ε_0 is the vacuum permittivity. The law of conservation or charge carriers leads to the continuity equation

$$e\frac{\partial i=p,n}{\partial t} = \frac{\partial J_n}{\partial x} + eG - eR \qquad \text{Equation 7}$$

where R is the recombination rate (to be discussed in more detail below). Therefore, assuming steady state, the governing equations for charge carrier transport within the perovskite layer are

$$\frac{\partial J_p}{\partial x} = eG - eR \qquad \text{Equation 8}$$

$$\frac{\partial J_n}{\partial x} = -eG + eR \qquad \text{Equation 9}$$

As well as Poisson's equation for electrostatic potential, U,

$$\frac{\partial^2 U}{\partial x^2} = \frac{-e(p-n+N_t)}{\varepsilon_r \varepsilon_0} \qquad \text{Equation 10}$$

where N_t is the ionized p-type defect density in the perovskite layer.

Finally, after transferring through their selective contact interfaces, the free charge carriers are extracted by the top and bottom electrodes. Modified versions of Equation 8 and Equation 9 (i.e. with the charge carrier generation and recombination terms removed)

$$\frac{\partial J_p}{\partial x} = 0 \qquad \text{Equation 11}$$

$$\frac{\partial J_n}{\partial x} = 0 \qquad \text{Equation 12}$$

can be used to describe the steady state charge transport through the HTL and ETL, respectively, along with the following Poisson's equation for electrostatic potential within the HTL and ETL

$$\frac{\partial^2 U}{\partial x^2} = \frac{-e(p - \rho_p)}{\varepsilon_r \varepsilon_0} \qquad \text{Equation 13}$$

$$\frac{\partial^2 U}{\partial x^2} = \frac{e(n - \rho_n)}{\varepsilon_r \varepsilon_0} \qquad \text{Equation 14}$$

where ρ_i (i = p, n) is the hole or electron doping density within the ETL or HTL, respectively.[10,49,50]

While this aforementioned process is the desired route for charge transfer within a perovskite solar cell, it is also possible for other undesirable process to occur. Instead of transferring to their respective interface contacts, the free charge carriers may recombine if the charge carrier lifetime (the time window for charge selective contacts to efficiently extract charges) is too short. Recombination can occur due to the presence of charge trap states in a material (trap-mediated recombination) (Figure 9a), as a result of the direct recombination of electrons with holes from band to band within the material (bimolecular recombination) (Figure 9b), or when one charge carrier transfers its energy to another carrier to allow for non-radiative recombination (Auger recombination) (Figure 9c).[51] The

charge carrier recombination rate, R (used in Equations 8 and 9), can be described using the Langevin theory

$$R = \gamma(np - n_i^2) \qquad \text{Equation 15}$$

where γ is the bimolecular recombination constant $\left(\gamma = \frac{e(\mu_p + \mu_n)}{\varepsilon_r \varepsilon_0}\right)$ and n_i is the intrinsic charge density of the perovskite, which is a function of the density of states (DOS) of the conduction band, N_c, and band gap energy, E_g, of the perovskite $\left(n_i = N_c \times \exp\left(\frac{-E_g}{2k_B T}\right)\right)$.[49,50]

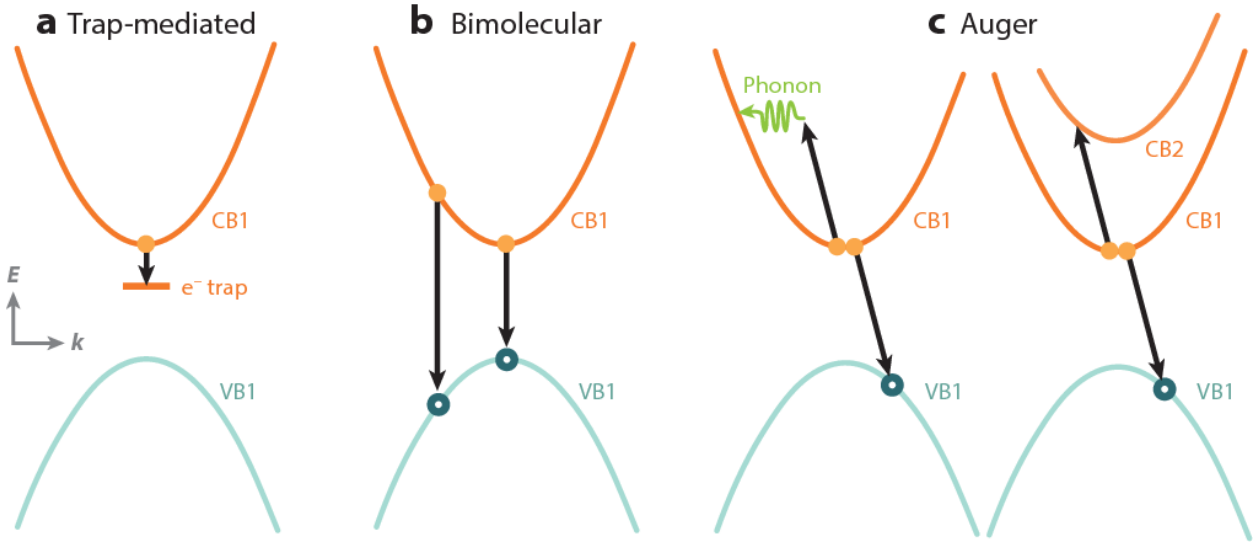

Figure 9. Visual representation of trap-mediated, bimolecular, and Auger recombination pathways. Reproduced from Reference [51].

Aside from recombination, the free charge carriers may also back transfer to the perovskite at the interfaces of the ETL or HTL with the perovskite. Furthermore, if the ETL and HTL are in any way contacted, then the charges may transfer between these layers rather than being extracted at the electrodes.[52] To help to avoid the undesirable charge transfer processes and promote efficient charge extraction (and ultimately performance) in a perovskite solar cell, it is important to select ETLs and HTLs that have favorable

conduction and valence band alignments with the perovskite absorber and electrodes, as well as those that foster balanced charge transfer at the interfaces.[53]

2.6 Current Problems Surrounding Perovskite Photovoltaics

Despite their remarkable achievements in PCE, there remain a few major issues with PSCs (stability, toxicity, and reproducibility) that must be addressed before this technology is fully market-ready.

2.6.1 Stability

One of the most appealing properties of hybrid organic-inorganic perovskite solid thin films is their ability to be processed at low temperatures (< 150 °C) by self-assembling from solution. However, due to their low energetic barrier of crystal formation, perovskites have poor structural and chemical stability in the presence of high temperatures,[54–56] prolonged light exposure,[57–60] and moisture,[28,61–63] and can experience rapid degradation to a photoinactive state under these conditions.

Hybrid organic-inorganic perovskite films are highly hydrophilic by nature, and readily absorb water from the surrounding environment causing the formation of various hydrates within the film. For $MAPbI_3$, in the presence of moisture, H_2O will deprotonate the methylammonium iodide, ultimately forcing a degradation to methylamine, hydrogen iodide, and solid lead iodide.[61] Further decomposition to hydrogen gas and solid iodine is possible if oxygen is also present (i.e. in humid ambient environment).[64] The solid lead iodide film that remains post-degradation is considerably photoinactive, causing the performance of the solar cell to drastically decrease.

It has been reported that intense prolonged light exposure can also lead to perovskite instability due to induced ion migration and lattice expansions/phase transitions. In the presence of oxygen under prolonged light exposure, it is possible for photogenerated electrons in the perovskite to react with oxygen to form a superoxide. The superoxide can then react with the methylammonium cation and cause a degradation to methylamine gas, solid lead iodide, and solid iodine.[65] Under an inert atmosphere, light-induced instability is still possible due to the migration of mobile methylammonium, iodide, and lead ions, with iodide having been noted as the most "mobile" of the three.[66] In one case, mobile ions, like iodide, can migrate towards the metal (e.g. silver) cathode and induce the formation of an insulating compound (e.g. silver iodide), which affects charge transport and thus diminishes the solar cell performance.[67] Additionally, mobile ions can migrate towards various interfaces or grain boundaries and cause light-induced hysteresis behavior and trap states within the solar cell, making it difficult to measure the actual efficiency output of the device.[68]

Upon exposure to heat (i.e. temperatures at or above 85 °C, the IEC 61 656 climatic chamber test temperature standard for thermal stability) it is possible for the perovskite film to degrade even under inert atmosphere. Due to its low formation energy, $MAPbI_3$ will ultimately sublime to methylamine gas, hydrogen iodide gas, and solid lead iodide upon prolonged exposure to increased temperatures.[65] In fact, the decomposition temperature for $MAPbI_3$ is often reported between 100 °C and 140 °C.[54,55] Furthermore, higher temperatures may also induce the migration of metal ions from the metal cathodes into the perovskite layer, inducing an irreversible degradation.[69,70]

Many efforts at improving perovskite film and solar cell stability have been proposed. Compositional engineering of the perovskite layer by substituting or mixing the MA cation with cesium (Cs) and/or formamidinium (FA), or the I^- anion with Br^- and/or Cl^- has been shown to induce stabilization in the perovskite crystal structure, which consequently improves the overall stability.[71–73] Improved stability, albeit with large reductions in PCE of the resulting solar cells, has also been observed for mixed 2D/3D organic-inorganic halide and double perovskite structures, again due to the enhanced structural stability.[74,75] Aside from changes to the perovskite layer itself, improvements to stability has also been achieved by using different encapsulation technologies that prevent water penetration into the perovskite film.[76,77] Nevertheless, these encapsulation technologies can increase the processing costs of the solar cell, lower the overall PCE of the solar cell, or increase the difficulty of upscaling the technology. Lastly, many researchers have reported that the instability of perovskites is linked to termination regions at the grain boundaries or on the surface.[78,79] Efforts to cap the surface with suitable protective materials or to passivate the grain boundaries have proven effective at improving perovskite solar cell stability. All in all, though, a perfect solution to the long-term stability issue of perovskites (one that maintains the high performance of the solar cell) has not yet been brought forth.

2.6.2 Toxicity

Lead-halide perovskite-based solar cells have exhibited the most superior photovoltaic performance compared to any of the currently proposed lead-free alternatives. This is primarily due to the fact that divalent lead has the best optoelectronic properties in 3D ABX_3 perovskites.[80] Nevertheless, the toxicity of lead is now well known to not just

scientists, but to virtually everyone, making acceptance of this technology by the general public a very difficult task. Furthermore, according to the EU Restriction of Hazardous Substances (RoHS), lead is a restricted substance with a maximum allotted level of < 1000 ppm.[81] A recent study has estimated that the lead concentration for a perovskite module is about 5500 ppm.[82] Therefore, current proposed perovskite commercial technologies could have lead levels even higher than what may be safe for consumers. In order for perovskite solar cells to become a more attractive technology to industry, investors, and consumers it is necessary to continue research efforts to develop high performance lead-free perovskite alternatives that can be processed from environmentally friendly solvents and materials.

2.6.3 Reproducibility

Although there is a large number of research groups currently involved to some degree in the field of hybrid organic-inorganic halide perovskites, there are only a few groups who can repeatedly produce perovskite solar cells with efficiencies exceeding 20%. Nevertheless, a deeper understanding of the fundamental principles and degradation mechanisms is still required to continue to improve device performance and stability; however, groups that work on such topics may not have the capabilities to fabricate highly efficient solar cells. Because such a gap exists between groups who can produce high performing perovskite solar cells and those who investigate fundamental properties of perovskite materials and devices, it becomes difficult to compare the results reported in manuscripts between various perovskite devices. Unfortunately, this discrepancy slows down research progress in the perovskite field and may even lead to contradictory results. Groups (especially those who consistently achieve >20% PCE devices) should, therefore,

aim to report extremely detailed and clear fabrication protocols such that any group can easily reproduce their results in their laboratories. This would allow for fundamental-based research to be conducted on the highest performing and reproducible PSCs and provide for more congruent comparisons throughout the field.[83,84]

CHAPTER 3

DISSERTATION OBJECTIVES

In this dissertation, I will present various strategies to improve the performance and stability of the planar, p-i-n $MAPbI_3$ PSC using cost-effective or roll-to-roll-compatible materials or strategies. Through this, we look to demonstrate that this perovskite cell architecture has certain inherent advantages over the planar or mesoporous, n-i-p architectures despite their inferior maximum PCE. All improvements made are achieved by optimization or engineering of different regions of the planar, p-i-n cell architecture.

1. To develop a roll-to-roll-compatible fabrication process that will yield a high-quality perovskite active layer atop a non-ideal surface. By forming an intermediate complex film via evaporation-induced self-assembly, which can then be easily converted to high-quality perovskite films, we show that improvement to the quality of the perovskite active layer alone leads to enhanced device performance.

2. To replace the commonly used calcium/aluminum top electrode, which quickly degrades upon exposure to air. Higher work function metals such as silver and gold are more stable than lower work function metals like aluminum, but ultimately yield lower device performance if used by themselves. However, by incorporating a thickness-tolerant, solution-processable n-doped zwitterionic fulleropyrrolidine derivative between the electron transport material and high work function top metal electrode, it is possible to effectively decrease the work function of the air-stable metal and enhance charge transport across the device in order to improve device performance and stability.

3. To find an alternative hole-transporting material to PEDOT:PSS that is still solution-processable and economical. The hydrophilic and acidic natures of PEDOT:PSS accelerate the degradations of the perovskite active layer and indium-doped tin oxide transparent bottom electrode, respectively. Inorganic copper-based hole-transport materials are cost-effective, more conductive, and do not possess the aforementioned drawbacks of PEDOT:PSS; however, they have been shown to exhibit poorer film morphology when processed from solution. We aim to investigate if (and if so, why) CuI, CuSCN, or blends of the two can function better than PEDOT:PSS as HTMs in PSCs in terms of performance. We speculate that the other inherent material or film properties of the Cu-based HTMs will overshadow their poor film morphology and lead to their improving the performance of the devices into which they are incorporated.

4. To improve the thermal and moisture stability of the planar, p-i-n perovskite solar cell using a protective overlayer. Insulating polymers can hinder moisture penetration into the perovskite active layer, but these layers must be made thin enough for charges to tunnel through or else performance will be sacrificed for stability. Roll-to-roll-compatible monolayer graphene, however, is naturally thin and can also hinder moisture penetration and heat-induced metal ion diffusion into the perovskite active layer due to its hydrophobic and highly impermeable properties. We speculate that graphene can serve as a viable protective barrier to water and diffusing metal ions if it can be effectively incorporated into the perovskite cell architecture. Electrons can easily tunnel through a single-atom layer thick sheet of graphene, so charge transport should not be compromised.

CHAPTER 4

IMPLEMENTING A VERSATILE PEROVSKITE ACTIVE LAYER FABRICATION PROCESS

4.1 Perovskite Film Fabrication Methods

The formation of high-quality perovskite thin films with good crystallinity, ideal purity, large grains, full surface coverage, and minimal surface roughness has yielded the best performing photovoltaic devices, indicating the importance of a well-defined and optimized active layer.[85–87] Several techniques have been employed to prepare the laboratory-scale perovskite active layer, including single-step solution deposition,[88] sequential or two-step solution deposition,[89,90] vapor-assisted solution deposition,[91] and vacuum deposition [92] (Figure 10).

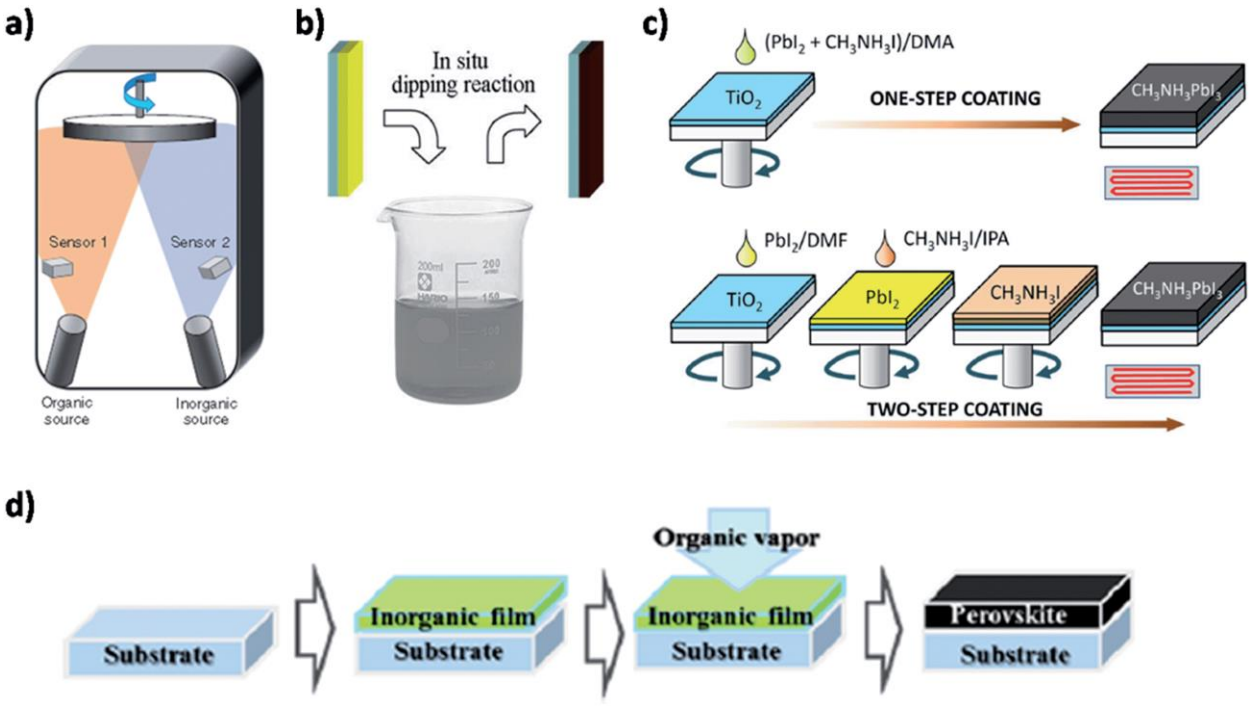

Figure 10. Perovskite film deposition techniques: (a) vacuum deposition, (b) sequential deposition with dipping in a solution of the organic cation, (c) single-step (top) and two-step (bottom) solution deposition, and (d) vapor-assisted solution deposition. Reproduced from Reference [86].

4.1.1 Single-step Solution Deposition

In single-step solution deposition, the perovskite precursors – the small organic molecule (e.g. MAI or FAI) and the metal halide (e.g. PbI_2 or $PbBr_2$) – are dissolved together in a polar aprotic solvent (e.g. GBL, DMF, or DMSO). The perovskite precursor solution is then spin-coated onto a desired substrate and the resulting film is annealed at a specific temperature to promote perovskite crystallization. The single-step solution deposition technique is perhaps the simplest method of perovskite film fabrication, but because of the poor crystallization dynamics of the organic-inorganic metal halide perovskite, films fabricated using the single-step solution deposition process are often low quality.[93] As such, researchers have used solvent engineering (Figure 11),[94] compositional engineering,[95] and additive engineering[96] to help improve the crystallization dynamics and thus the overall quality of the resulting perovskite film when using single-step solution deposition.

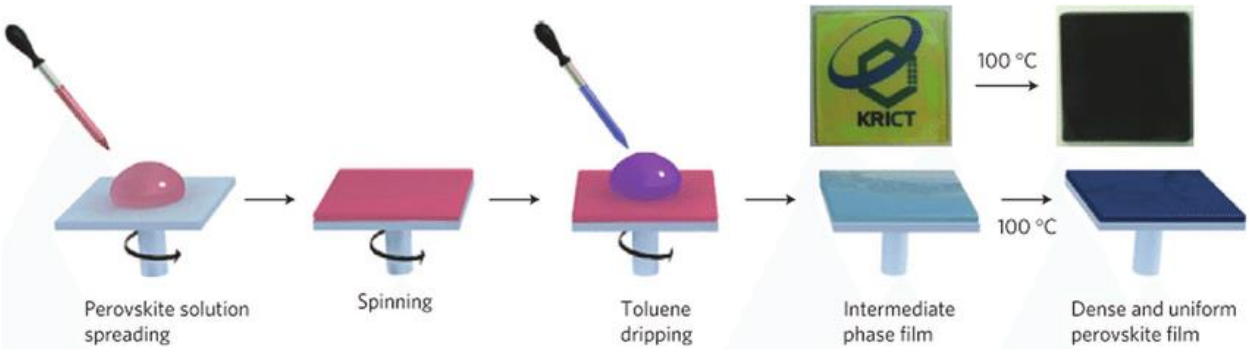

Figure 11. A schematic representation of the single-step solution deposition technique with solvent engineering in which an anti-solvent (e.g. toluene) is dripped on the spinning perovskite precursor solution. Reproduced from Reference [94].

4.1.2 Two-step Solution Deposition

The two-step deposition process involves first creating one solution of the metal halide in a polar aprotic solvent, and a second solution of the small organic molecule in an alcohol

(commonly, 2-propanol). The metal halide solution is then spin-coated onto a desired substrate to form a thin film, followed by either spin-coating or dip-coating that film with the solution of the organic molecule in alcohol. Thermal annealing of the film then yields the 3D crystalline perovskite.

4.1.3 Vapor-assisted Solution Deposition

The vapor-assisted solution deposition process (VASP) is similar to the two-step solution process in that a film of the metal halide is first produced by spin-coating from a solution of the metal halide in a polar aprotic solvent. However, instead of spin-coating or dip-coating with a solution of the organic molecule in alcohol, the powder form of the organic molecule is spread out around the metal halide film on a hot plate. Upon covering the materials and heating to a desired temperature, the perovskite film forms as the organic powder sublimes and integrates into the metal halide film.[91]

4.1.4 Vacuum Deposition

With vacuum deposition, two crucibles are filled with powders of the small organic molecule and the metal halide, separately. The crucibles are placed in an evaporation chamber, which is then pumped down to a low pressure. After heating each crucible to the desired deposition temperature, the powders vaporize and then begin to deposit onto a desired substrate, forming the perovskite film in the process. Single-source rather than dual-source vacuum deposition is also possible provided that the target substrate is first spin-coated with a film of the metal halide prior to evaporation of the small organic molecule.[92]

4.2 Evaporation-Induced Self-Assembly with Intramolecular Exchange for Perovskite Film Fabrication[97]

4.2.1 Introduction

The two-step solution deposition method has proven to generate high quality perovskite films with admirably reproducible solar cell performance.[98,99] This method has shown to be effective in producing thick and uniform perovskite active layers when a mesoporous titanium dioxide (TiO_2) or alumina (Al_2O_3) scaffold is present;[23,89,100] however, difficulty has arisen when trying to use this process to make thick films in planar architectures.[101] Poor surface morphology and a large amount of unconverted PbI_2 with thicker films forces the fabrication of thinner perovskite active layers for planar devices, resulting in a decrease in the amount of light absorbed, and thus a drop in the cell's short-circuit current (J_{sc}) and overall PCE.

In an effort to make an unprecedented >500 nm thick formamidium lead iodide ($FAPbI_3$) perovskite active layer in a mesoporous-TiO_2 cell architecture, Seok and co-workers used an intramolecular exchange sequential deposition process in which sequentially deposited formamidium iodide (FAI) molecules "exchange" with dimethyl sulfoxide (DMSO) molecules of a previously deposited PbI_2(DMSO) complex film.[102] Because the FAI molecules have strong ionic bonding and the DMSO molecules have weak coordination with the PbI_2 molecules, the exchange occurs rapidly. While this method led to a record efficiency in 2015, the 24-hr vacuum annealing step required to obtain the PbI_2(DMSO) complex powder needed to fabricate the PbI_2(DMSO) complex intermediate film renders the process lengthy and not conducive to large-scale solution processing. Recently, though, Kim and co-workers showed that PbI_2(DMSO) complex films could be obtained in only

one step by spin-coating from a 1:1 molar ratio of PbI_2 and DMSO in DMF.[103] Using this process they fabricated solar cells comprising $FAPbI_3$/$MAPbBr_3$ mixed layers, and their champion FTO/bl-TiO_2/$(FAPbI_3)_{3-x}(MAPbBr_3)_x$/PTAA/Au device achieved a PCE of 17.1%, indicating that perovskite active layers could be successfully grown with the intramolecular exchange sequential deposition process in planar n-i-p architectures.

Here, we used a similar one step spin-coating process to fabricate semi-crystalline PbI_2(DMSO) complex films from a solution in which the stoichiometry of PbI_2 and DMSO was carefully controlled to be 1:1. We show that the PbI_2(DMSO) complex films are actually formed through an evaporation-induced self-assembly process during spinning when the optimal spin-coating conditions are used. These intermediate films were then used to create thick, highly crystalline, and uniform perovskite films using the most common perovskite material, $MAPbI_3$. Despite the limitations inherent to growing perovskite films on amorphous surfaces, we were able to obtain pinhole-free, good coverage films on a PEDOT:PSS surface. Moreover, we found that it was possible to produce optimum quality perovskite layers using different concentrations of MAI provided deposition occurred at a specific corresponding spin speed. This shows that, like $FAPbI_3$, $MAPbI_3$ can also be fabricated using the intramolecular exchange sequential deposition process. Finally, instead of the more commonly used planar n-i-p architecture, $MAPbI_3$ perovskite solar cells were fabricated in a planar p-i-n architecture. The planar p-i-n architecture with a PEDOT:PSS hole-transport layer and a $PC_{61}BM$ electron-transport layer was chosen due to its potential scalability, compatibility with flexible substrates, ease of processing, and absence of corrosive hole-transport material dopants. Additionally, the

more hydrophobic and electron conductive $PC_{61}BM$ layer inherently yields higher device stability and lower J-V hysteresis compared to planar n-i-p TiO_2-based devices.[104–107]

By careful optimization of the perovskite active layer only, a maximum PCE of 16.72% was obtained without compositional[95,108] or interfacial engineering.[40,109–111] Similar photovoltaic device metrics are reported for 100 complete solar cells, demonstrating the notable reproducibility of the process. The intramolecular exchange sequential deposition process was used to simply, inexpensively, and reproducibly fabricate efficient $MAPbI_3$ perovskite active layers in the most basic planar p-i-n perovskite solar cell architecture: ITO/PEDOT:PSS/ $MAPbI_3$/$PC_{61}BM$/Ca/Al.

4.2.2 Experimental

4.2.2.1 Solar Cell Device Fabrication

Patterned indium-doped tin oxide (ITO) substrates (20 Ω/sq, 14.7 cm^2, Thin Film Devices) were cleaned with 2% Hellmanex® (Sigma-Aldrich) soap solution, deionized water, acetone, and IPA (in that order) with 10 min of ultra-sonication in each step, followed by drying in an oven at 140 °C overnight. Before being used, the cleaned ITO substrates were exposed to UV/Ozone treatment for 20 min. Following the cleaning and surface polarization, the ITO substrates were coated with an aqueous dispersion of PEDOT:PSS (HeraeusClevios™ P VP AI 4083) through a 0.45 μm PVDF filter, spun at 3500 rpm for 90 s, and annealed on a hot plate at 150 °C for 30 min in air. This resulted in a film thickness of 40±5 nm as measured by profilometry. The PEDOT:PSS-coated substrates were then transferred to a N_2-glovebox for the remainder of the procedure. A stoichiometrically controlled 1:1 molar ratio of PbI_2 (Alfa Aesar, 99.9985% (metals basis)) and DMSO

(anhydrous, Sigma-Aldrich) was dissolved fully at room temperature in DMF (anhydrous, Sigma-Aldrich). Specifically, 461 mg PbI_2/944 mg DMF and 78 mg DMSO/944 mg DMF were used for the 1.0 M PbI_2(DMSO) complex solution. The PbI_2(DMSO) complex solution was filtered through a 0.45 μm PTFE filter and 30 μL was spun onto the PEDOT:PSS-coated substrates at 1500 rpm for 15 s. Immediately, 100 μL of MAI (Dyesol) in IPA (anhydrous, Sigma-Aldrich) was drop-casted onto the PbI_2(DMSO) complex film. After a 20 s loading time, the film was spun for 30 s, at which point the film turned from a transparent yellow to a dark brown. The perovskite film was then annealed at 100 °C for 1 hr in the dark. After the perovskite was formed, 35 μL of a 10 mg/mL $PC_{61}BM$ (nano-C) solution in chlorobenzene (anhydrous, Sigma-Aldrich) was immediately spun onto the perovskite film at 1000 rpm for 30 s. Following a previous report,[107] the films were then covered with a petri dish and left to solvent anneal in the dark for 24 hours before being transferred to the thermal evaporator. Finally, a 15 nm thick Ca electrode at a rate of 0.5 Å/s followed by a 100 nm thick Al electrode at a rate of 1−2 Å/s were thermally deposited, both at a chamber pressure of at least 3×10^{-6} mbar. The device area was fixed at 0.06 cm^2.

4.2.2.2 Characterization

Current−voltage (J−V) curves were tested inside a N_2-glovebox using a Keithly 2400 source-meter under simulated AM 1.5G solar irradiation at 100 mV/cm^2 light intensity. The light source was a 300 W Xe lamp (Newport 91160) that was adjusted with an NREL-calibrated Si reference solar cell and KG-5 filter. No photomask was used for the J-V measurements. X-ray diffraction (XRD) measurements were made with a PANalytic X'Pert^3 X-ray diffractometer having a Ni filter, 1/2 in. diverging slit, vertical goniometer,

and X'Celerator detector. Measurements were made from 2θ = 5° or 10°−40° under Cu Kα (λ = 1.542 Å). Scanning electron microscopy (SEM) images were obtained using a FEI Magellan 400 microscope at 15 kV. Prior to imagining, samples were mounted on a metal stub using a piece of carbon tape and then coated with a thin layer of platinum to avoid charging. Thickness measurements were made using a KLA Tencor Alpha-Step profiler.

4.2.3 Results and Discussion

In this study, a two-step sequential deposition technique was used to prepare thick and highly uniform perovskite thin films with minimal defects by employing the concept of intramolecular exchange. First, by fixing the PbI_2:DMSO stoichiometry to a 1:1 molar ratio and the PbI_2 concentration to 1.0 M in DMF, we were able to systematically study the effect of spin speed and spin time on PbI_2(DMSO) complex film formation and quality. With an optimized PbI_2(DMSO) complex film, we then determined the MAI concentration/spin speed combinations that resulted in the best quality perovskite films. We defined high quality perovskite films to be those that possess high crystallinity and purity according to their XRD patterns, as well as minimal surface roughness and pinholes according to their SEM morphologies.

As a Lewis acid, PbI_2 has been known to form 1:1 and 1:2 adducts with Lewis base bidentate or monodentate ligands. Polar aprotic solvents, such as DMF and DMSO, are O-donors and act as Lewis bases, making them good candidates for adduct formation by coordinating with PbI_2. Specifically, PbI_2 likes to strongly coordinate with DMSO solvent molecules in solution via the formation of Pb–O bonding. The 1:2 complex between PbI_2 and DMSO, $PbI_2(DMSO)_2$, readily forms when PbI_2 is dissolved directly in DMSO[112] (or

when PbI_2 is present with excess DMSO in a DMF primary solvent since DMSO has a stronger coordination ability than DMF[113]), and then crystallizes into a film or powder. Powders or films of the $PbI_2(DMSO)_2$ complex have been shown to be more crystalline as the DMSO molecules favourably intercalate into the interlayer space of the Pb–I network during crystallization.[95,100,102,112] When the PbI_2:DMSO stoichiometry is carefully controlled to be 1:1 in solution, however, PbI_2 will form the 1:1 adduct as only one coordination site ends up being occupied by the DMSO molecules, and so the $PbI_2(DMSO)$ complex forms during crystallization. Powders or films of the $PbI_2(DMSO)$ complex yield diffraction patterns indicating an amorphous or semi-crystalline structure as fewer DMSO molecules have intercalated into the PbI_2 framework.[100,102]

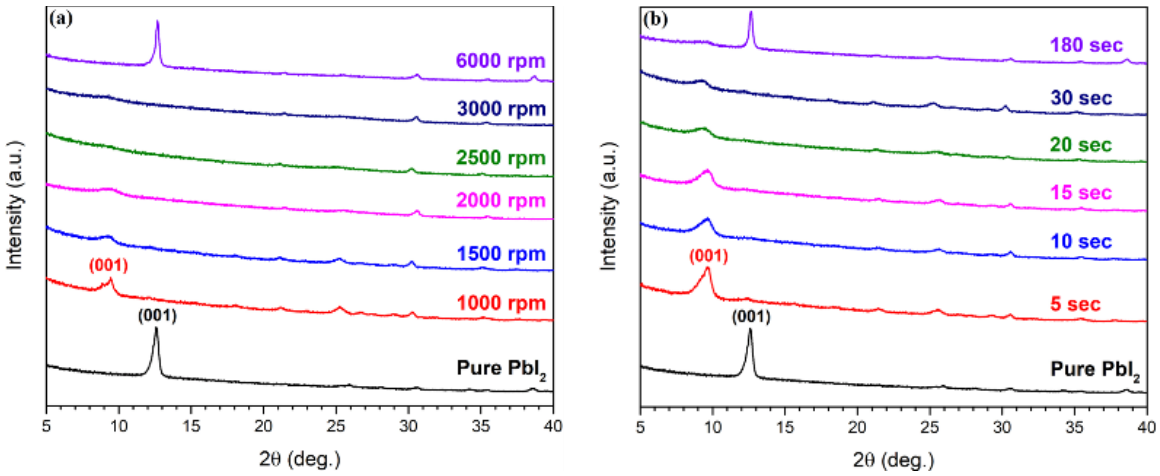

Figure 12. XRD patterns of 1.0 M PbI_2 (black patterns) and 1.0 M $PbI_2(DMSO)$ complex films (all other patterns) from a solution spun at (a) various speeds for 30 s and (b) 1500 rpm for various times onto ITO/PEDOT:PSS substrates. The pure PbI_2 films were spun at 1500 rpm for 30s. Note that the characteristic (001) peak shifts from 12.6° for pure PbI_2 to 9.8° for $PbI_2(DMSO)$ due to the intercalation of the DMSO molecules into the PbI_2 framework.

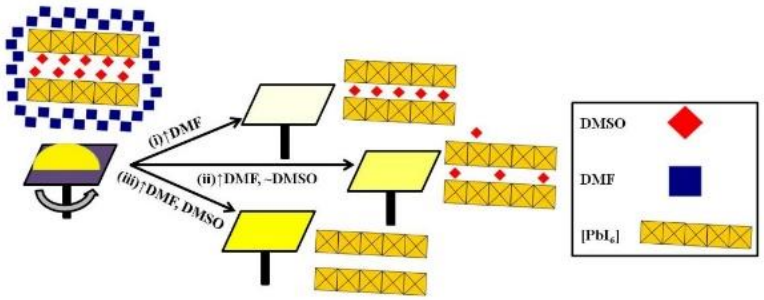

Figure 13. Schematic view of the evaporation-induced self-assembly process. Lower spin speeds and short spin times effectively yield the semi-crystalline PbI_2(DMSO) complex intermediate film. Higher spin speeds and longer spin times eventually yield the pure, crystalline PbI_2 intermediate film.

The self-assembly of PbI_2:DMSO complex films from a stoichiometrically controlled 1:1 PbI_2:DMSO complex solution in DMF is strongly dependent on the speed and time at which the solution is spin-coated onto a substrate (PEDOT:PSS-coated ITO in this case). It should be noted that because of the carefully controlled stoichiometry, the PbI_2:DMSO complex films formed here are semi-crystalline or amorphous PbI_2(DMSO) and not crystalline $PbI_2(DMSO)_2$.[102] To optimize these parameters, first, the spin speeds of the complex solution were varied from 1000 rpm to 6000 rpm, while the spin time was fixed to 30 s (Figure 12a). For pure PbI_2 films (Figures 12a and 12b, black pattern), the characteristic (001) diffraction peak can be seen at 12.6°, while for the semi-crystalline PbI_2(DMSO) complex films formed using spin speeds between 1000 and 2000 rpm, the (001) peak has shifted to 9.8°. This shift towards lower diffraction angles is due to the successful intercalation of DMSO molecules, which increases the distance between the I-Pb-I layers of the PbI_2 network. From 2000 rpm to 3000 rpm, however, the (001) diffraction peak begins to disappear, and the films adopt an amorphous structure. Similarly, the PbI_2(DMSO) complex films adopt a semi-crystalline form at lower spin times (5-15 s), and a more amorphous form at higher spin times (20-30 s) (Figure 12b). Interestingly, the

characteristic (001) PbI_2 peak at 12.6° began to appear at higher spin speeds (6000 rpm) and longer spin times (180 s) (Figures 12a and 12b, respectively), indicating that increasing the spin speeds and spin times further would eventually lead to pure PbI_2 films. We speculate the reason for this to be that at lower spin speeds and shorter spin times the coordination between the PbI_2 and the intercalated DMSO molecules is strong enough to withstand dissociation from the complex, so only the low viscosity, high vapor pressure DMF solvent molecules evaporate, yielding the semi-crystalline PbI_2(DMSO) complex film (Figure 13, path (i)). At higher spin speeds and longer spin times, however, the DMSO molecules begin to dissociate from the PbI_2 (some may even evaporate), which leads to more amorphous PbI_2(DMSO) complex films (Figure 13, path (ii)). Increasing the spin speed beyond 3000 rpm and spin time well beyond 30 s leads to pure, crystalline PbI_2 films as both the DMSO and DMF molecules evaporate (Figure 13, path (iii)). It should be noted that PbI_2(DMSO) complex films would also convert to pure PbI_2 films if left to sit for an extended period of time.

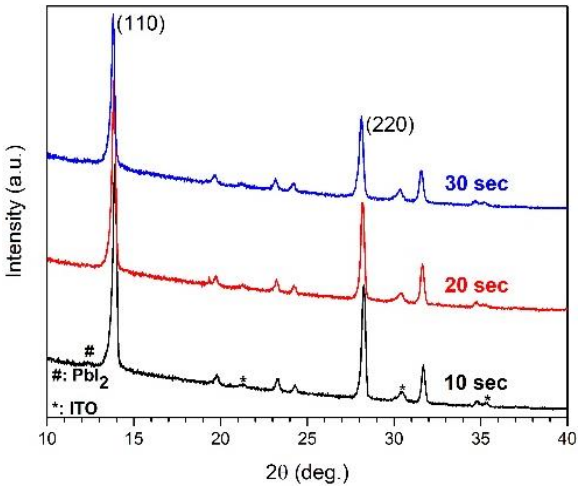

Figure 14. XRD patterns for $MAPbI_3$ perovskite films formed from 1.0 M PbI_2(DMSO) complex intermediate films. The 1.0 M PbI_2(DMSO) complex intermediate films were prepared by spin-coating a 1:1 PbI_2:DMSO solution in DMF onto ITO/PEDOT:PSS substrates at 1500 rpm for 10, 20 and 30 s (black, red, and blue lines, respectively). PbI_2(DMSO) crystallinity increases with decreasing spin time, and, noticeably, $MAPbI_3$ crystallinity also increases with increasing PbI_2(DMSO) crystallinity as evident by the increasing (110) and (220) perovskite peak intensities at 14.1° and 24.8°, respectively.

Due to the absence of structural order, amorphous PbI_2(DMSO) complex films would require additional rearrangement steps for perovskite film formation during the intramolecular exchange between the DMSO and organic halide molecules. Therefore, it was hypothesized that the most crystalline PbI_2(DMSO) complex films; that is, those films with the largest (001) peak intensity, would yield the most crystalline (and presumably the highest quality) perovskite films. To corroborate this, we fabricated $MAPbI_3$ perovskite films on PbI_2(DMSO) complex films formed by spin-coating the PbI_2(DMSO) complex solution at 1500 rpm for 10, 20 and 30 s (most crystalline to least crystalline) (Figure 14). The $MAPbI_3$ perovskite film was formed through the PbI_2(DMSO) complex intermediate film by the intramolecular exchange of DMSO with MAI (Figure 15). It was observed that the characteristic (110) and (220) $MAPbI_3$ perovskite peaks at 14.1° and 28.4°, respectively, increased in intensity with increasing PbI_2(DMSO) complex film crystallinity

(Figure 14). However, while more crystalline PbI_2(DMSO) complex films facilitated the formation of more crystalline perovskite films as postulated, they did not necessarily yield the highest quality perovskite films. In fact, PbI_2(DMSO) complex films fabricated at low spin speeds (below 1500 rpm) or short spin times (below 15 s) had visibly rough surfaces and ultimately yielded rough perovskite films. Because of this, 1500 rpm for 15 s was chosen as the ideal spin speed and spin time for a 1.0 M PbI_2(DMSO) complex solution as it would foster the formation of perovskite films with both good crystallinity and visibly smooth surface morphologies. These PbI_2(DMSO) complex films were found to be 350±10 nm as measured by profilometry.

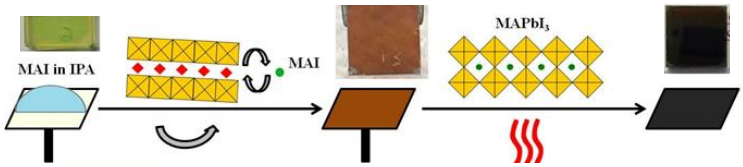

Figure 15. Schematic representation of the intramolecular exchange sequential deposition process between MAI and the DMSO of the PbI_2(DMSO) complex intermediate film during spin-coating. Subsequent thermal annealing then yields the $MAPbI_3$ perovskite.

MAI concentrations from 50-75 mg/mL in IPA (increments of 5 mg/mL) and spin speeds from 3000-6000 rpm (increments of 1000 rpm) were used to study the effects of MAI concentration and spin-coating speeds on perovskite film quality. To obtain good perovskite crystallinity with ideal purity, higher concentrations of MAI required higher spin speeds, whereas lower concentrations required lower spin speeds. Figure 16 shows the evolution of the XRD pattern for perovskite films formed from spin-coating various concentrations of MAI in IPA at 3000 rpm for 30 s (after a 20 s loading time) and then annealing at 100°C for 1 hr. Low purity films (those with a surplus of unconverted PbI_2) were formed with the lower MAI concentration of 50 mg/mL, as evidenced by the

prominent characteristic PbI_2 peak at 12.6°. Increasing the MAI concentration led to perovskite films of greater purity (less intense (001) PbI_2 peak) and crystallinity (more intense (110) and (220) perovskite peaks) since more PbI_2 was converted to $MAPbI_3$. Above 60 mg/mL, though, the perovskite films started to appear rough and subtleties in the perovskite XRD patterns began to emerge; namely, a ramping effect before the (110) perovskite peak, a small peak just before the (112) perovskite peak, and another small peak just before 30°. These features are a result of an increase in d-spacing within the $MAPbI_3$ crystal due to the presence of excess MAI within the lattice, as the MAI that was unable to participate in the intramolecular exchange likely remained on the surface or accumulated at the grain boundaries. These same trends were also observed for spin speeds of 4000 rpm, 5000 rpm and 6000 rpm (not shown), with the optimal spin speed and MAI concentration combinations (those that yielded the highest quality perovskite film) all occurring just before the unconverted MAI started to appear.

Upon incorporating these optimized active layers into a completed device, we found, as expected, that those perovskite active layers with smooth surface morphologies and higher crystallinity resulted in the best performing devices. Table 1 provides the optimized spin speed and concentration combinations for the MAI spin-coating step along with their corresponding device performance values. Amazingly, the average efficiencies (η) were very similar for each spin speed and concentration combination, indicating that formation of high quality and high performing sequentially deposited perovskite films is MAI concentration independent so long as an appropriate corresponding spin speed is used for a specific concentration range.

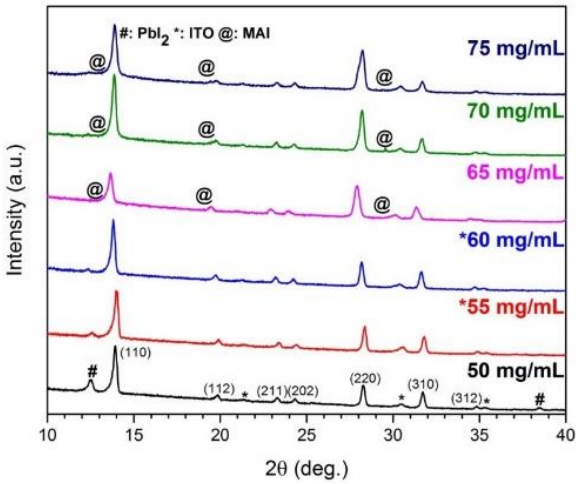

Figure 16. XRD patterns of $MAPbI_3$ perovskite films formed from 1.0 M PbI_2(DMSO) complex intermediate films. MAI of various concentrations in IPA were spun at 3000 rpm for 30 s.

Table 1. Average $MAPbI_3$ performance and film thickness values using the optimized MAI conc. and spin speed combinations.

MAI Conc. (mg/mL)	Spin-Coating Settings	J_{sc} (mA/cm^2)	V_{oc} (V)	FF (%)	η (%) [Best η (%)]	$MAPbI_3$ Film Thickness (nm)
55-60	3000 rpm for 30 s	21.35	0.88	71	13.36 [15.24]	403
60-65	4000 rpm for 30 s	21.05	0.89	71	13.29 [16.72]	399
65-70	5000 rpm for 30 s	21.14	0.87	72	13.28 [15.04]	398
70-75	6000 rpm for 30 s	20.59	0.89	73	13.35 [16.57]	401
All Combinations Combined		**21.03**	**0.88**	**72**	**13.30 [16.72]**	**400**

The J-V curves for the best performing devices and a plan-view SEM images of the perovskite active layers formed using our process and the conventional sequential deposition process are shown in Figures 17a and 17b. In addition to the high degree of crystallinity and ideal purity reported earlier, the exceptional performance of these devices is clearly a result of the better surface coverage, thicker absorbing layer, and the larger perovskite grain sizes compared to the conventional sequential deposition process. Whereas the conventional sequential deposition process yielded grain sizes in the tens of

nanometers, our process produced grains up to one micron in size (Figures 17a and 17b, insets). Smooth film morphology and greater grain size suppresses charge trapping and minimizes hysteresis,[85] which improves solar cell performance.

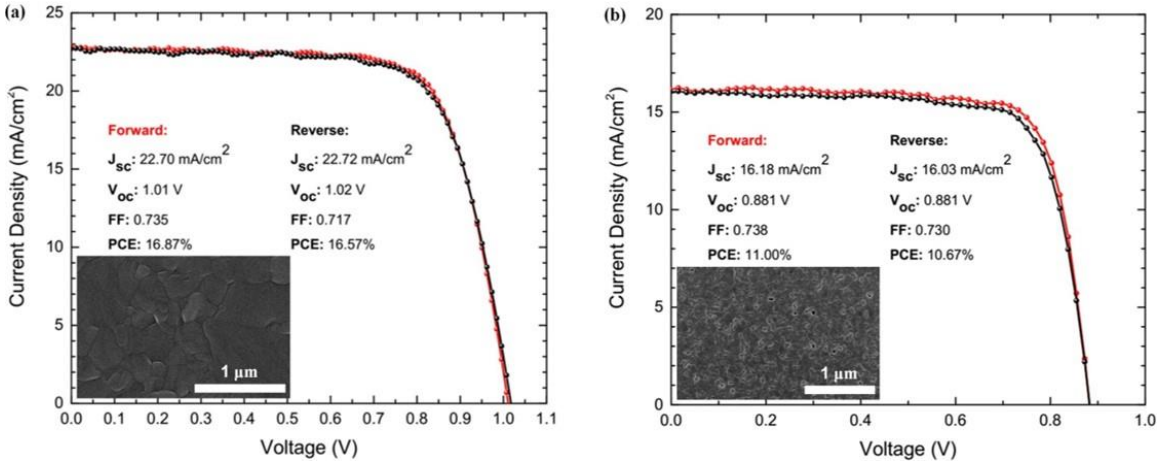

Figure 17. (a) J-V characteristics and plan-view SEM image (inset) for the best-performing $MAPbI_3$ perovskite solar cell formed using the evaporation-induced self-assembly with intramolecular exchange process, and (b) J-V characteristics and plan-view SEM image (inset) for the best-performing $MAPbI_3$ perovskite solar cell formed using the conventional sequential deposition process. Note the negligible hysteresis behavior between the forward and reverse scans.

Table 2. Comparison of intermediate and perovskite layer thicknesses for films formed using the conventional sequential deposition process and evaporation-induced self-assembly with intramolecular exchange process.

Processing Method	PbI_2-Based Film Thickness	$MAPbI_3$ Film Thickness
Conventional Sequential Deposition	210±10 nm	420±10 nm
Evaporative-Induced Self Assembly with Intramolecular Exchange	350±10 nm	400±10 nm

Surface profilometer measurements were done to compare layer thickness before and after the formation of the $MAPbI_3$ perovskite phase (Table 2). Noticeably, the volume expansion for the intramolecular exchange sequential deposition process was much less than that for

the conventional sequential deposition process in accordance with a previous report.[102] When spin-coated under the same conditions, PbI_2(DMSO) complex films will be thicker than pure PbI_2 films since the PbI_2(DMSO) films have intercalated DMSO between the I-Pb-I layers. When the pure PbI_2 intermediate film converts to the $MAPbI_3$ perovskite film using the conventional sequential deposition process, there is considerable volume expansion with the pure PbI_2 film due to (1) the incomplete conversion of the PbI_2 to the $MAPbI_3$ perovskite (some PbI_2 remains at the bottom) and (2) a structural distortion as a result of the interdiffusion between MAI and PbI_2 during thermal annealing. On the other hand, with the intramolecular exchange sequential deposition process, the MAI molecules directly replace the DMSO molecules of the PbI_2(DMSO) complex film. As a result, there is little volume expansion during the conversion of the PbI_2(DMSO) intermediate film to the $MAPbI_3$ perovskite. The minor volume expansion with the intramolecular exchange sequential deposition process allowed for the fabrication of thicker, smoother films of greater perovskite crystallinity and fewer defects than those fabricated from the conventional sequential deposition process. Interestingly, we found that the final perovskite film thickness was ultimately determined by the thickness of the PbI_2(DMSO) complex intermediate film. Regardless of the spin speed or MAI concentration used in the MAI deposition step, the perovskite film was found to be around 400±10 nm. It should be noted that although the conventional sequential deposition process yielded a thicker perovskite film, poorer device performance was observed most likely due to pinholes formed as a result of poor surface coverage and film roughness. Therefore, thinner perovskite films had to be fabricated with the conventional sequential deposition process in order to obtain homogenous films and, thus, better overall performance. Ultimately, the

ability to fabricate thick perovskite active layers with good surface morphology and large grain sizes with our process allowed for average J_{sc} and FF values above 20 mA/cm^2 and 70%, respectively, which in turn resulted in exceptional average device performance.

4.2.4 Conclusions

Careful stoichiometric control and evaporation-induced self-assembly via spin-coating were used to simply fabricate semi-crystalline PbI_2(DMSO) complex intermediate films in a single step. Thick, crystalline and uniform $MAPbI_3$ perovskite active layers of ideal purity and with grain sizes up to one micron were then made through an intramolecular exchange sequential deposition process. It was found that different concentrations of MAI in IPA could be used to produce equally high-quality perovskite films of similar average performance values so long as an appropriate spin speed was used in line with the specific corresponding MAI concentration range. An optimized device exhibiting a PCE of 16.72% was produced as a result of the dense and smooth morphology of the perovskite active layer without the need for interfacial or compositional engineering. This study provides a facile and reproducible optimization method for fabricating thick and efficient perovskite solar cells with planar p-i-n device architectures that would be ideal for scalability. Use of compositional engineering of the perovskite active layer with FAI, CsI, and MABr; interfacial engineering of the $PC_{61}BM$-metal electrode interface; and optimization of the electron and hole-transport layers may help further improve the overall performance of the solar cell. It is also well known that solar cells comprising ABX_3 perovskite active layers exhibit very poor moisture stability. However, due to its inherent barrier properties and conductivity, graphene can effectively prevent water from penetrating into the devices

while simultaneously allowing for electron transfer to the top electrode. The incorporation of the graphene barrier avoids the need for expensive, post-processing encapsulation, and represents a key step towards the realization of low temperature roll-to-roll manufacturing of stable, efficient, and flexible perovskite solar cells.

CHAPTER 5

REPLACING THE UNSTABLE CALCIUM/ALUMINUM ELECTRODE VIA INTERFACIAL ENGINEERING

5.1 Introduction

Aluminum coupled with a thin underlying layer of calcium (Ca/Al) has been frequently used in organic solar cells as the device cathode.[114] The inorganic calcium has an intrinsically low work function and aids in maximizing the device V_{oc} and minimizing the contact resistance.[115] As such, the Ca/Al electrode has also been adopted by planar perovskite solar cells that use polymer and fullerene hole and electron transport layers, respectively, and reputable PCE's have been reported.[116] Nevertheless, neither calcium nor aluminum can be processed from solution, and both materials are sensitive to oxygen and moisture, which hinders their use as commercially viable electrodes. Higher work function metals such as gold (Au) and silver (Ag) can be solution deposited and are more stable in the environment; however, they require some sort of interfacial modifier to lower their effective work functions, otherwise device performance will be sacrificed due to weak built-in electrostatic potential.[117–119]

Aside from Ca, other conductive inorganic (e.g. LiF) and polar organic interlayers (e.g. PEI and BCP) have been used as interfacial work function modifiers for the metal electrode.[120–122] Unfortunately, many of these interlayers cannot be effectively processed from solution and must be made thin (less than 5 nm) to prevent charge accumulation. To circumvent these issues, Page *et al.* developed two solution-processable fulleropyrrolidine interlayers: C_{60}-N (a tertiary anime functionalized fullerene) and C_{60}-SB (a zwitterionic sulfobetaine functionalized fullerene) for effective cathode (Au, Ag, Cu, and Al) work

function modification in organic solar cells.[123] What is more, these interlayers showed impressive air stability and thickness tolerance up to about 30 nm, lending way to their roll-to-roll compatibility and commercial viability. Liu *et al.* later used the C_{60}-N interlayer, which outperformed the C_{60}-SB interlayer in the organic solar cells, in planar p-i-n PSCs to reduce the work function of the Ag cathode due to the large negative interfacial dipole. The presence of the fulleropyrrolidine interlayer reduced recombination losses and improved charge carrier lifetime, charge extraction, and device stability, and an improvement in PCE from 7.5% (bare Ag) to 15.5% (C_{60}-N/Ag) was reported.[111]

Here, we show that the zwitterionic C_{60}-SB interlayer can also be effectively used as a work function modifier to an Ag cathode in planar p-i-n PSCs. When previously used in organic solar cells, the C_{60}-N interlayer exhibited a larger work function reduction and higher electron mobility than the C_{60}-SB interlayer due to the presence of a lone pair on the nitrogen of the C_{60}-N, providing ohmic contact due to self-doping.[124] By n-type doping the C_{60}-SB interlayer with tetra-n-butyl ammonium iodide (TBAI), we promote anion-induced electron transfer (a similar effect to the tertiary anime self-doping), which ultimately allows for increased Ag work function reduction (from 4.0 eV for C_{60}-SB/Ag to 3.65 eV for C_{60}-SB:TBAI/Ag) and improved electron mobility of the C_{60}-SB. Owing to the conductivity of C_{60}-SB:TBAI, the doped interlayer has the ability to function for a wide range of thicknesses. The combination of improved conductivity and work function reduction of the C_{60}-SB:TBAI interlayer helped to improve maximum device performance from 11.5% (bare Ag) to 16.8% (C_{60}-SB:TBAI/Ag).

5.2 Experimental

5.2.1 Materials

Methylammonium iodide (MAI), lead iodide (PbI_2), and $PC_{61}BM$ were purchased from Dyesol, Alfa Aesar, and American Dye Source, respectively. The synthesis of C_{60}-SB is described elsewhere.[123] Tetra-n-butyl ammonium iodide (TBAI, > 99%) was purchased from SigmaAldrich.

5.2.2 Interlayer Preparation

The C_{60}-SB, TBAI, and mixed C_{60}-SB:TBAI interlayers of different thicknesses were spin-coated from 2,2,2 trifluoroethanol (TFE) solutions with concentrations ranging from 0.25 to 12 mg/mL at 4000 rpm for 60 s. Film thicknesses greater than ~30 nm were measured by surface profilometry (KLA Tencor, model Alpha-Step IQ) directly. The ultraviolet-visible-near infrared (UV-vis-NIR) absorbance of C_{60}-SB films at 450 nm was used to determine the thickness of thinner films. The thickness of thin TBAI films was determined by extrapolating the film thickness versus solution concentration, using the surface profiler measurements of larger film thicknesses. Weight ratios (wt %) of 99:1, 95:5, 90:10, 80:20, 70:30, and 50:50 were used for mixed C_{60}-SB:TBAI interlayer materials. The concentrations of all mixed solutions were kept at 2 mg/mL to produce consistent interlayer film thicknesses.

5.2.3 Solar Cell Device Fabrication

An inverted planar p-i-n architecture was used for perovskite devices, ITO/PEDOT:PSS/$MAPbI_3$/$PC_{61}BM$/interlayer/Ag. Initially, a 35 nm thick PEDOT:PSS

(Clevios P VP AI 4083, Heraeus) layer was spin-coated onto the ultraviolet (UV)- ozone-treated ITO-coated glass substrates (resistivity of 20 Ω/ sq, Thin Film Devices, Inc.) and annealed at 150 °C for 30 min. After transferring to a nitrogen glovebox, PbI_2 [Alfa Aesar, 99.9985% (metals basis)] and DMSO (anhydrous, Sigma-Aldrich) were dissolved in a 1:1 molar ratio at room temperature in DMF (anhydrous, Sigma-Aldrich) to form a 1.0 M PbI_2(DMSO) complex. The solution was spun onto the PEDOT:PSS-coated substrates at 1500 rpm for 15 s, immediately followed by spin coating of 60 mg/mL MAI (Dyesol) in IPA (anhydrous, Sigma-Aldrich) at 2500 rpm for 30 s. The resulting perovskite film was annealed at 100 °C for 1 h in the dark. After the methylammonium lead iodide ($MAPbI_3$) perovskite was formed, 35 μL of a hot (90 °C) 20 mg/mL $PC_{61}BM$ solution in chlorobenzene was spin-coated onto the hot (~100 °C) perovskite film at 2000 rpm for 30 s. Following procedures from a previous report,[107] the films were covered with a Petri dish and allowed to solvent anneal in the dark for 24 h. The devices were completed by spin-coating of either C_{60}-SB, TBAI, or C_{60}-SB:TBAI cathode interlayers, followed by thermal evaporation of either a 100 nm thick Ag electrode at a base pressure of 3×10^{-6} Torr through a shadow mask.

5.2.4 Characterization

UPS measurements were performed using an electron spectroscopy for chemical analysis instrument (Scienta Omicron Nanotechnology, model ESCA+S) operating at 4×10^{-10} mbar. Room-temperature X-band electron paramagnetic resonance (EPR) spectra were collected on powders using the perpendicular mode of a dual-mode resonator cavity (Bruker Elexsys E-500 with ER-4116 cavity). The current density-voltage (J-V)

characteristics of photovoltaic devices were measured using a Keithley 2400 source-meter. Illumination was performed with a solar simulator (Newport 91160, 100 mW/ cm^2) equipped with an AM1.5G filter and calibrated using a reference Si solar cell with a KG5 window (Newport certification). An overlap of the Ag electrode and patterned ITO substrate defined a device area of 0.06 cm^2. The photomask of 0.054 cm^2 area (calibrated at NREL) was overlapped with the Ag electrode to define the illuminated device area. The average device metrics are given for 8 perovskite devices fabricated on 4 different substrates. Impedance spectroscopy was performed using an Agilent 4294A impedance analyzer on devices directly with an oscillation amplitude of 10 mV, applied bias, and illumination as described later. The fitting of Cole-Cole plots was done using ZView software package (Scribner Associates Inc.). All device characterization was performed inside the glovebox.

5.3 Results and Discussion

The chemical structures of C_{60}-SB and TBAI are shown in Figure 18a, a schematic of the device architecture used for the PSC is shown in Figure 18b, and electron spin resonance (EPR) spectra evidence of charge transfer (doping) between the iodide anion of TBAI and C_{60}-SB is shown in Figure 18c. The peak in the energy absorption in the C_{60}-SB:TBAI spectrum indicates charge transfer.

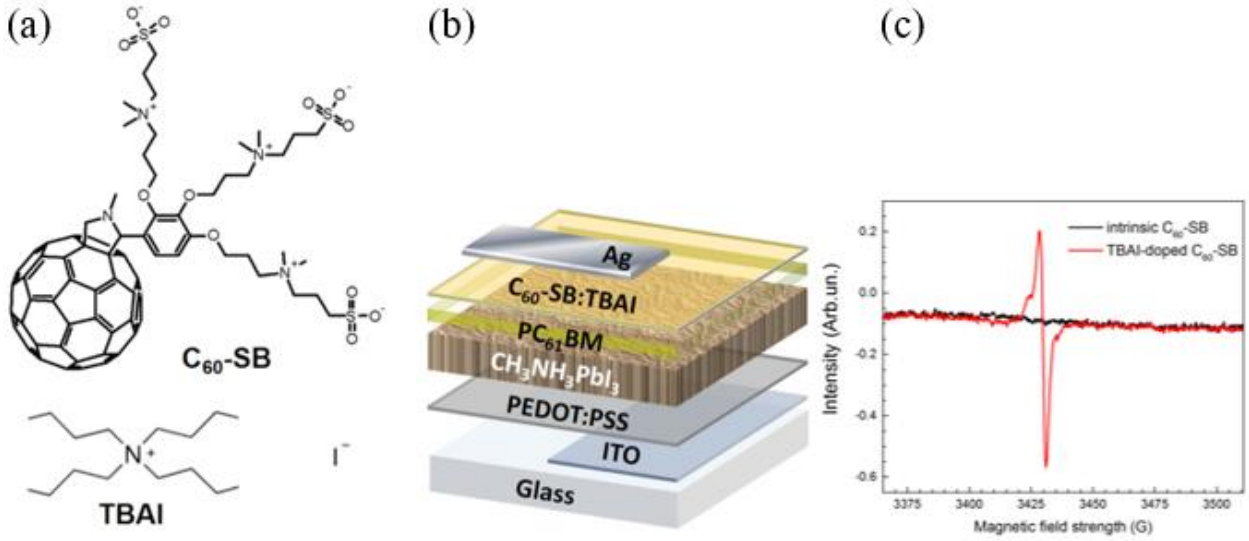

Figure 18. (a) Chemical structures of C_{60}-SB and TBAI; (b) device architecture used for inverted planar p-i-n PSC with an $MAPbI_3$ active layer; and (c) EPR spectra of C_{60}-SB and C_{60}-SB:TBAI (50:50 wt%). Reproduced from Reference [125].[125]

The J-V characteristics for the best performing $MAPbI_3$ PSCs with various interlayers are shown in Figure 19. Inserting a C_{60}-SB interlayer into the device improved the maximum device perfromance from 11.5% (bare Ag) to 14.0% (C_{60}-SB /Ag). However, the Ca/Al cathode still outperformed the C_{60}-SB interlayer, achieving a maximum PCE of 15.2%. Nevertheless, an 80:20 wt% mixture of the C_{60}-SB:TBAI interlayer functioned more effectively than both the pure C_{60}-SB and the Ca/Al, producing a maximum PCE of 16.8%. The 90:10 and 70:30 wt% mixtures of the C_{60}-SB:TBAI interlayer (not shown) gave maximum PCEs of 15.7% and 16.4%, respectively, also outperforming the Ca/Al cathode. Figure 20 summarizes the average device metrics for inverted PSCs of different C_{60}-SB:TBAI doping levels. The improvement of PSC device performance originates mainly from enhanced V_{oc} and slightly from enhanced J_{sc}.

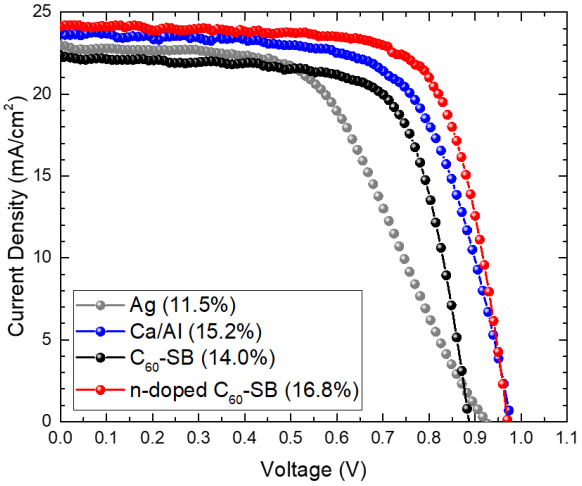

Figure 19. J-V characteristics of the best performing inverted $MAPbI_3$ PSCs with different interlayer/cathode arrangements. An Ag cathode was used for both the intrinsic and doped C_{60}-SB interlayers. The n-doped C_{60}-SB interlayer shown in the plot is an 80:20 wt% mixture of C_{60}-SB:TBAI. Measurements were obtained with no photomask.

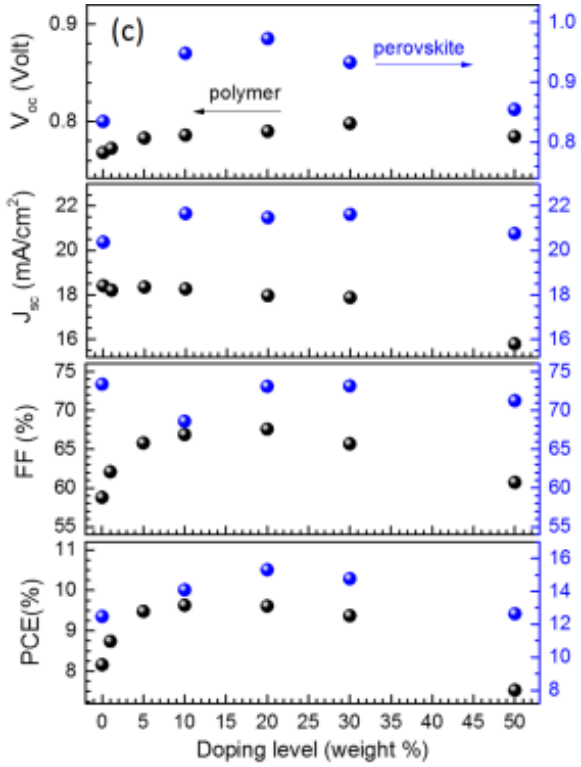

Figure 20. Average device metrics for inverted $MAPbI_3$ PSCs with C_{60}-SB:TBAI/Ag electrodes of different C_{60}-SB:TBAI doping levels (reproduced from Reference [125]).[125] A photomask with an area of 0.54 cm^2 was used for these measurements. Note that values for polymer solar cells are shown here as they were also being studied alongside the PSCs in Reference [125], but are beyond the scope of Aim 2.

By examining the electronic structure of the C_{60}-SB/Ag and C_{60}-SB:TBAI/Ag interfaces using UPS, we were able to determine the cause of the improved device performance that occurs from n-doping the C_{60}-SB interlayer with TBAI. As shown in Figure 21a, addition of the C_{60}-SB interlayer increases the binding energy onset from 16.8 eV (bare Ag) to around 17.25 eV, corresponding to a work function (Φ) decrease of 0.45 eV from 4.45 eV (bare Ag) to a saturation point of 4.0 eV (C_{60}-SB/Ag) (Figure 21b). The work function change ($\Delta\Phi$) with the addition of the zwitterionic C_{60}-SB has been attributed to the self-alignment of the zwitterionic dipoles of the sulfobetaine side chains as a result of their interaction with the image charges on the surface of the Ag metal cathode. As shown in the left panel of Figure 21c, the largest achievable work function reduction attainable at the C_{60}-SB:TBAI interface is determined by the Fermi level pinning at the energy of negative integer charge transfer (ICT^-) states (E_{ICT^-}), which explains why a saturation point is possible for thickness-dependent work function modification. The alignment of the zwitterionic dipoles is counterbalanced by electron transfer from occupied states below the Fermi level of the metal to unoccupied ICT^- states of the C_{60}-SB.

Increasing TBAI content in C_{60}-SB:TBAI further increases the binding energy onset to a saturation point around 17.6 eV (Figure 21a), corresponding to a Ag work function reduction to 3.65 eV (a $\Delta\Phi$ of 0.8 eV) (Figure 21b). As shown in the right panel of Figure 21c, the existence of the extrinsic electrons from the TBAI allow for the population of the negative polaron states (E_{np}), which raises the Fermi level. This is evidenced by the 0.2 eV shift in the HOMO (and thus LUMO) level of C_{60}-SB:TBAI with respect to the Fermi level of the C_{60}-SB/Ag (Figure 21a). As a result, the Ag metal cannot transfer electrons to the ICT^- states, and thus the Fermi level is pinned at higher energies, which explains the larger

$\Delta\Phi$ for C_{60}-SB:TBAI/Ag compared to C_{60}-SB/Ag. Since Fermi level pinning is also occurring in this case, a saturation point or the work function is again expected and can be seen in Figure 21d. Interestingly, the same work function of 3.65 eV obtained here for C_{60}-SB:TBAI/Ag was also seen for C_{60}-N/Ag in a previous report[124], which correlates well since the two interlayers exhibit the same HOMO/LUMO levels.

For pure TBAI, which lacks π-conjugation, the work function of Ag is reduced to 3.0 eV for an ~30 nm thick TBAI film (Figure 21d) since electron transfer from the Ag metal is unable to occur as the ammonium/iodide of the TBAI interacts with the metal. This allows for a larger $\Delta\Phi$; however, the insulating nature of TBAI and its unfavorable reaction with Ag to create undesirable AgI species hinders its application as an effective interlayer alone.

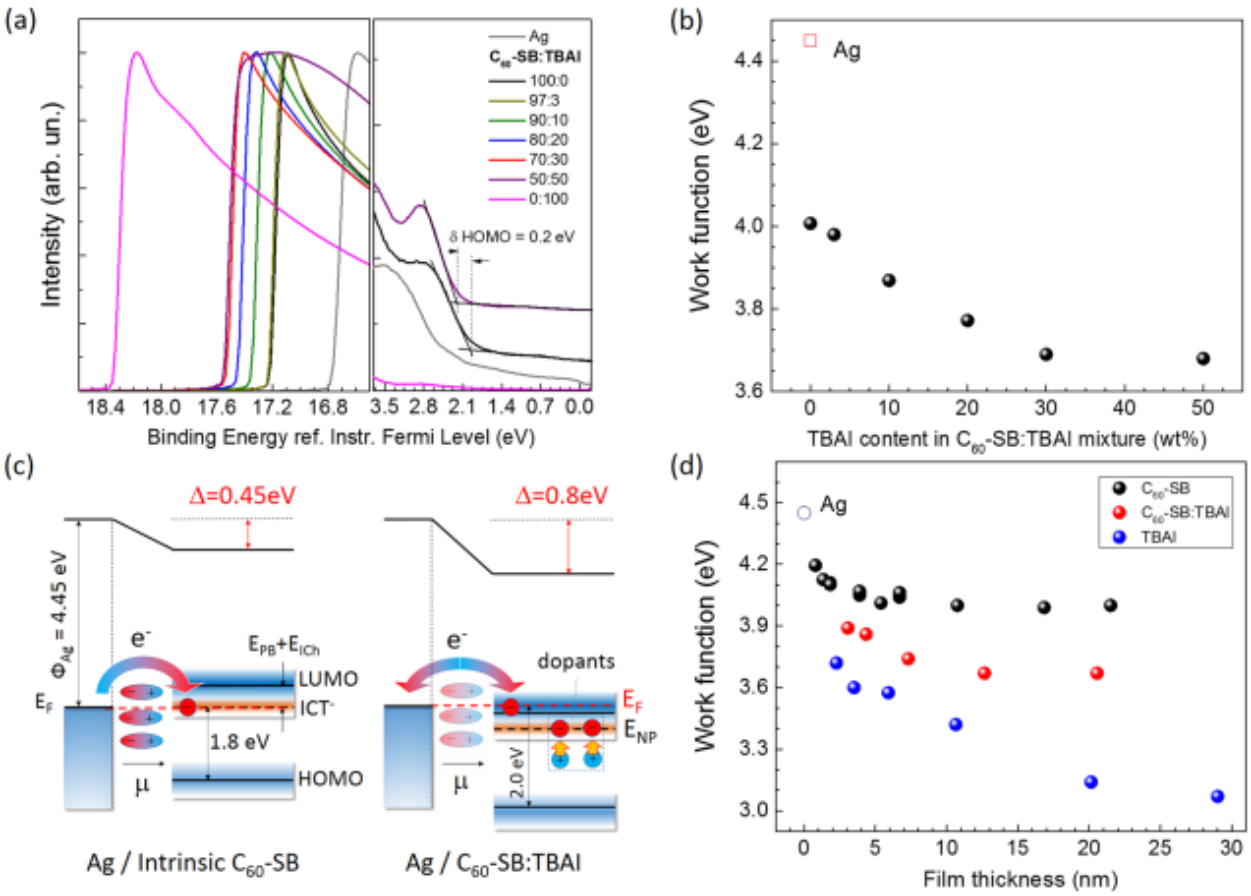

Figure 21. (a) UPS spectra of bare Ag and C_{60}-SB:TBAI-covered Ag for various weight ratios of C_{60}-SB:TBAI; (b) the observed work functions of a C_{60}-SB:TBAI/Ag electrode for different weight ratios of C_{60}-SB:TBAI; (c) a schematic electronic structure of C_{60}-SB/Ag (left) and C_{60}-SB:TBAI/Ag (right) interfaces; and (d) the observed work functions of C_{60}-SB-covered, C_{60}-SB:TBAI (50:50)-covered, and TBAI-covered Ag electrodes for interlayer films of different thicknesses. Reproduced from Reference [125].[125]

The reduction in the Ag cathode work function not only helps to improve charge extraction through the PCBM ETM. Additionally, the doping of the C_{60}-SB interlayer also helps to improve the band alignment between itself and the PCBM, further facilitating electron extraction at the cathode.

5.4 Conclusions

In summary, a thickness-independent, TBAI-doped zwitterionic fulleropyrolidine interlayer, C_{60}-SB:TBAI (solution-processed from an orthogonal solvent to that of the PCBM ETM), was successfully incorporated into inverted $MAPbI_3$ PSCs. The C_{60}-SB:TBAI interlayer allowed for a Fermi level pinning at higher energies than those allowed by intrinsic C_{60}-SB, which resulted in a higher reduction of the interlayer/Ag electrode work function (3.65 eV for C_{60}-SB:TBAI compared to 4.0 eV for C_{60}-SB). The higher work function reduction and the improved conductivity of the C_{60}-SB:TBAI interlayer improved charge extraction throughout the device; and as a result, inverted PSCs with a maximum PCE of 16.8% for an 80:20 wt% of C_{60}-SB:TBAI were achieved, outperforming those PSCs with a Ca/Al electrode. The higher environmental stability, solution-processability, and thickness tolerance of the C_{60}-SB:TBAI interlayer are advantageous for the future development of inverted PSCs aiming towards commercialization.

CHAPTER 6

COPPER-BASED HOLE TRANSPORT MATERIALS AS A REPLACEMENT FOR PEDOT:PSS

6.1 Introduction

In 2013, Jeng *et al.* reported the first perovskite/fullerene planar-heterojunction hybrid solar cell in which poly(3,4-ethylenedioxythiophene) polystyrene sulfonate (PEDOT:PSS) was used as a hole-transporting layer, mimicking a common architecture of organic solar cells.[42] Since then, PEDOT:PSS has been widely used as the conventional hole-transport material (HTM) for planar p-i-n (inverted) perovskite solar cells (PSCs). While PEDOT:PSS is an attractive polymer for use as a HTM due to its low-temperature solution processability, high transparency, and good film quality, the material itself is relatively expensive and exhibits poor stability.[126–128] In fact, it has been shown that the acidic and hydrophilic natures of PEDOT:PSS hinder the long-term stability of inverted PSCs by degrading the ITO transparent conductive electrode and promoting water ingress into the active layer.[129] Other polymer HTMs such as P3HT, PTAA, and Poly-TPD have been used to replace PEDOT:PSS in inverted PSCs, and while optimized processing and doping of these materials has helped achieve PCEs and stabilities beyond those obtained by PEDOT:PSS-based inverted PSCs, they still remain costly.[130–137] Additionally, poorer hole mobility or transparency of these replacement polymer HTMs often requires that layers be made relatively thin (< 5nm), which is not compatible with large-scale roll-to-roll manufacturing.[135] For these reasons, researchers have looked towards the use of inorganic HTMs to replace PEDOT:PSS. Inorganic HTMs such as NiO, CuI, Cu_2O, and CuSCN are relatively cheaper and exhibit higher stability and mobilities than organic HTMs.[138–143] The

higher mobilities of the inorganic HTMs allows for the fabrication of thicker films provided optical transparency is not compromised. However, achieving uniform thin films via solution-processing with inorganic HTMs is a difficult task, which has forced many researchers to use more complicated and costly processes, such as vapor deposition, for film deposition.[135]

Of the inorganic HTMs reported, Cu-based HTMs are most intriguing materials for PEDOT:PSS replacements in inverted $MAPbI_3$ PSCs since they offer the low-cost and solution-processability without the hydrophilicity and acidity drawbacks.[135] Both CuI and CuSCN have been previously used in inverted PSCs as HTMs, with each having its advantages and disadvantages.[144–148] On the one hand, CuI exhibits higher hole mobility relative to CuSCN, whereas CuSCN crystallizes at a slower rate than CuI and thus exhibits better film morphology. Both CuI and CuSCN offer good optical transparency. By merging CuI and CuSCN into a composite, Luo *et al.* sought to balance the hole-mobility and film morphology properties to create an optimized charge-transport layer in polymer LEDs. They found that a 25 wt% proportion of CuI in CuSCN produced a composite film that outperformed films produced from both the pure CuI and pure CuSCN.[149]

Through a detailed study, we investigate the benefits and drawbacks of CuI, CuSCN, and CuI:CuSCN blends as HTMs in inverted PSCs using various device and thin film characterization tools. We suggest processing conditions for the Cu-based HTMs for optimized solar cell performance. Ultimately, the inverted PSCs fabricated with Cu-based HTMs either rivaled or outperformed those fabricated with a PEDOT:PSS HTM in terms of performance stability and efficiency, indicating their viability for usage in the future of inverted PSCs.

6.2 Experimental

6.2.1 Preparation of Solutions

Copper iodide (CuI, Alfa Aesar) and copper thiocyanate (CuSCN, Alfa Aesar) solutions were prepared by dissolving a desired mass in either acetonitrile (MeCN, anhydrous, Acros) for CuI or diethyl sulfide (DES, Sigma Aldrich) for either CuI or CuSCN for 2 h at room temperature. The solutions were then filtered with a 0.45 µm PTFE filter. CuI:CuSCN blends were prepared by mixing the filtered 15 mg/mL stock solutions of CuI and CuSCN in DES in a 1:3, 1:1, or 3:1 volume ratio, and then stirring for 1 h. To prepare the PbI_2(DMSO) complex solution, a 1:1 molar ratio of lead iodide (PbI_2) (Alfa Aesar) and dimethyl sulfoxide (DMSO) (anhydrous, Acros) was dissolved fully at room temperature in N,N-dimethylmethanamide (DMF) (anhydrous, Acros), and then filtered with a 0.45 µm PTFE filter. Specifically, 461 mg PbI_2/944 mg DMF and 78 mg DMSO/944 mg DMF were used for a 1.0 M PbI_2(DMSO) complex solution. A methylammonium iodide (MAI) solution was prepared by fully dissolving 60 mg MAI (Greatcell Solar) in 1 mL 2-propanol (anhydrous, Acros), and then filtering with a 0.45 µm PTFE filter. A phenyl-C61-butyric acid methyl ester (PCBM) solution was prepared by dissolving 10 mg of PCBM (nano-C) in 1 mL chlorobenzene (anhydrous, Sigma-Aldrich) at 55 °C overnight, cooling to room temperature while stirring, and then filtering with a 0.45 µm PTFE filter. A C_{60}-N cathode interlayer solution was prepared by dissolving 3 mg C_{60}-N (1-Material) in 1 mL 2,2,2-trifluoroethanol (TFE, Acros) overnight, and then filtering with a 0.45 µm PTFE filter.

6.2.2 Solar Cell Device Fabrication

Patterned indium-doped tin oxide (ITO) substrates (20 Ω/sq, 14.7 cm^2, Thin Film Devices) were cleaned with a 2% Mucasol™ (Sigma-Aldrich) soap solution, deionized water, acetone (Fisher), and 2-propanol (Fisher) (in that order) with 10 min of ultra-sonication at each step, followed by drying in an oven at 140 °C overnight. Prior to use, the cleaned ITO substrates were exposed to UV/Ozone treatment for 20 min. For the devices with a PEDOT:PSS HTM, PEDOT:PSS (Clevios P VP AI 4083, Heraeus) was spin-coated onto the ITO-coated glass substrates at 3500 rpm for 90 s, and then annealed at 150 °C for 30 min before being transferred to an N_2-glovebox. For the devices with Cu-based HTMs, the ITO substrates were transferred to an N_2-glovebox and spin-coated with 50 μL of the Cu-based HTM solution at 3000 rpm for 60 s. If annealing was desired, the Cu-based HTM films were annealed at 100 °C for 10 minutes. Once cooled to room temperature, 50 μL of the PbI_2(DMSO) complex solution was spun onto the Cu-based HTM substrates at 1500 rpm for 15 s, immediately followed by a spin-coating of 100 μL of the MAI solution at 2500 rpm for 30 s. The resulting perovskite film was annealed at 100 °C for 1 hr in the dark. After the $MAPbI_3$ perovskite was formed and the substrate cooled to room temperature, 50 μL of the PCBM solution was spun onto the perovskite film at 1000 rpm for 30 s. Following a previous report,[107] the films were covered with a petri dish and allowed to solvent anneal in the dark for 24 hours. The perovskite devices were completed by spin-coating 80 μL of the C_{60}-N solution at 4000 rpm for 60 s, followed by thermal evaporation of a 100 nm thick Ag electrode at a base pressure of 3×10^{-6} mbar through a shadow mask. An overlap of the Ag electrode and patterned ITO substrate defined a device area of 0.06 cm^2.

6.2.3 Characterization

Current−voltage (J−V) curves were tested inside a N_2-glovebox using a Keithly 2400 source-meter under simulated AM 1.5G solar irradiation at 100 mV/cm^2 light intensity. The light source was a 300 W Xe lamp (Newport 91160) that was adjusted with an NREL-calibrated Si reference solar cell and KG-5 filter. No photomask was used for the J-V measurements. X-ray diffraction (XRD) measurements were made with a PANalytic X'Pert^3 X-ray diffractometer having a Ni filter, 1/2 in. diverging slit, vertical goniometer, and X'Celerator detector under Cu Kα (λ = 1.542 Å). Scanning electron microscopy (SEM) images were obtained using a FEI Magellan 400 microscope at 15 kV. Prior to imagining, samples were mounted on a metal stub using a piece of carbon tape and then coated with a thin layer of platinum to avoid charging. Thickness measurements were made using a KLA Tencor Alpha-Step profiler. Ultraviolet–visible spectroscopy measurements were made using a PerkinElmer Lambda 950 UV-vis-NIR Spectrometer in the wavelength range of 250-900 nm. The UPS measurements were performed with a Scienta Omicron Nanotechnology, model ESCA+S at a base pressure of 4×10^{-10} mbar. The instrument configuration consisted of a He discharge lamp (He I line, 21.2 eV) as the UV excitation source and a hemispherical SPHERA energy analyzer. The measurements were performed at a -3V sample bias to collect the low kinetic energy electrons. The binding energy scale in the UPS spectra is given with reference to a vacuum level, which was taken 21.2 eV away from the onset of the secondary electron cut off energy. The HOMO level was determined from the intersection of a tangent line to the low-binding-energy onset with the abscissa axis. The resolution of the instrument was ~0.1 eV as determined from the width of a Fermi level of Ar+-sputtered silver. Films for the UPS measurements were spin-coated

onto UV-O_3-treated ITO-coated glass either outside the glovebox (for PEDOT:PSS) or inside the glovebox (for the Cu-based HTMs from MeCN or DES). Films fabricated inside the glovebox were transferred to the UPS instrument with minimal exposure to ambient air (<30 seconds).

6.3 Results and Discussion

A planar p-i-n inverted PSC device architecture of the form ITO/HTM/$MAPbI_3$/PCBM/C_{60}-N/Ag was used for the purposes of this study. The HTMs used were PEDOT:PSS, CuI, CuSCN, or CuI:CuSCN blends. The solvents MeCN and DES were chosen as the two solvents for the Cu-based HTMs. Whereas CuSCN may only be dissolved in DES, CuI is soluble in both MeCN and DES; however, the maximum solubility of CuI in MeCN was found to be about 30 mg/mL. The first part of this study focused on analyzing the morphology of PEDOT:PSS and the various Cu-based HTM films. However, preliminary efficiency results for complete PSCs did not match what was expected based on morphological observations, suggesting that film morphology is not the only factor that contributes to overall device performance. After film thickness optimization, complete PSCs using PEDOT:PSS, CuI from MeCN, or CuI:CuSCN from DES (1:0, 3:1, 1:1, 1:3, and 0:1 v:v) HTMs were fabricated and tested to obtain average device efficiency values. HTM film optics, crystallinity, conductivity, and electronic energy levels as well as $MAPbI_3$ perovskite film crystallinity and morphology on various HTM surfaces were then investigated in an effort to better understand the performance trends observed with devices employing the different HTMs.

6.3.1 HTM Film Morphology with Preliminary Device Performance Results

For film morphology analysis by SEM, all Cu-based HTMs were fabricated on ITO-coated glass substrates from a 15 mg/mL solution and annealed at 100 °C for 10 minutes (unless otherwise indicated). Films of CuI from DES and MeCN were analyzed first; their SEM images are shown in Figure 22.

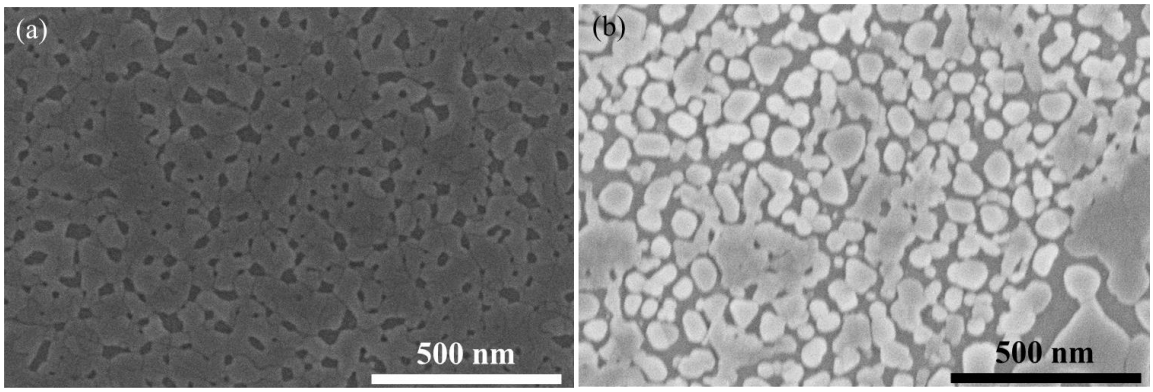

Figure 22. SEM images of CuI films on ITO-coated glass substrates from MeCN (a) and DES (b) solvents.

Visibly, neither solvent leads to a CuI film with full-surface coverage. The CuI film from MeCN shows numerous pinholes, whereas the CuI film from DES shows island growths. The poor film quality for both films can be attributed to the fast crystallization dynamics of CuI. Additionally, the higher volatility of DES relative to MeCN is likely the reason that CuI films from DES showed an inferior film quality between the two under the same spin-coating conditions. To avoid charge trap/recombination sites and increased charge transport resistance, good HTM film quality is important. For this reason, MeCN is the preferred solvent of the two for CuI film fabrication. Increasing the concentration of CuI in MeCN to 30 mg/mL had no noticeable effect on film quality; however, annealing the CuI film at room temperature rather than 100 °C appeared to lessen the number of observable pinholes (Figure 23). The SEM images for PEDOT:PSS and CuSCN films on

ITO are shown in Figure 24. Both CuSCN and PEDOT:PSS showed superior film quality and surface coverage compared to CuI, which can be attributed to CuSCN's slower crystallization dynamics relative to CuI and PEDOT:PSS's polymeric nature.

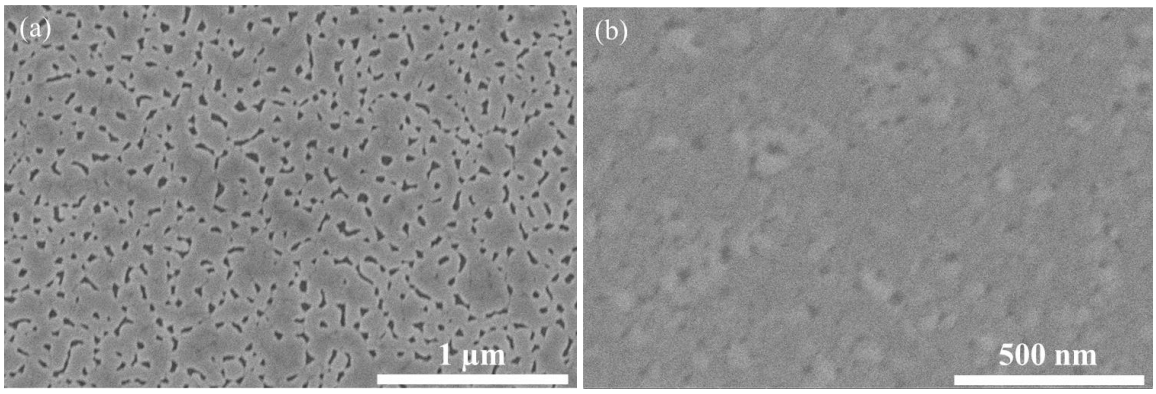

Figure 23. SEM images of CuI films on ITO-coated glass substrates from 30 mg/mL MeCN annealed at 100 °C for 10 minutes (a) and 15 mg/mL MeCN annealed at room temperature for 10 minutes (b).

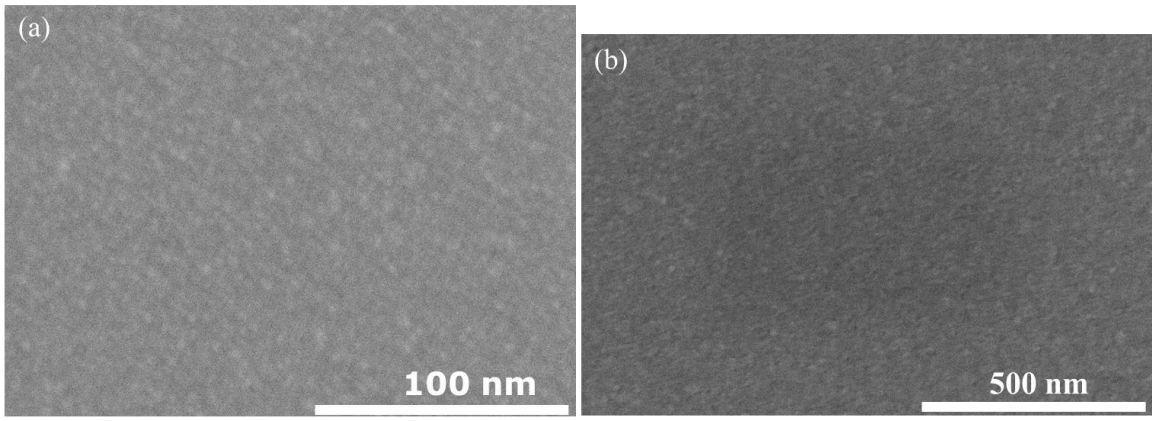

Figure 24. SEM images of (a) CuSCN films from 15 mg/mL DES annealed at 100 °C for 10 minutes and (b) PEDOT:PSS films on ITO-coated glass substrates.

For further analysis of Cu-based HTM film morphology, blends of CuI:CuSCN (1:3, 1:1, and 3:1 v:v) were made using 15 mg/mL stock solutions of CuI and CuSCN in DES. DES was chosen as the solvent due to CuSCN's insolubility in MeCN. The SEM images of the three CuI:CuSCN composite films prepared on ITO are shown in Figure 25. For the 3:1

composite film, it appears as though there is a phase separation between the CuI and CuSCN (Figure 25c). Film morphology of the composite blends improved as the volume % of CuSCN increased (Figure 25a and Figure 25b); in fact, the 1:1 and 1:3 CuI:CuSCN composite films show a much improved film quality compared to the pure CuI film from DES (Figure 22b), suggesting that the added CuSCN has aided in suppressing the fast crystallization of the CuI.

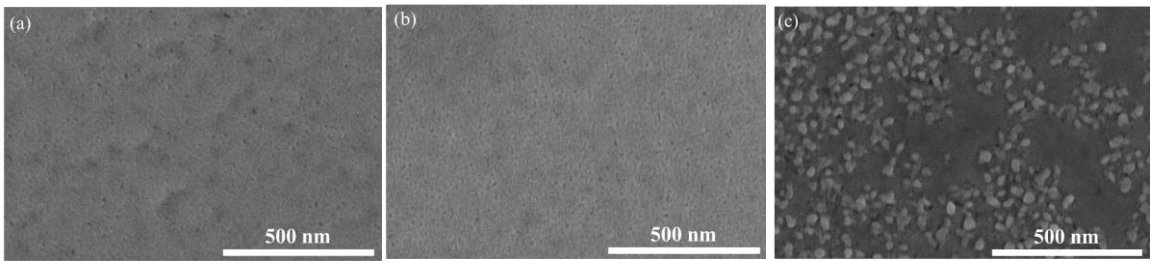

Figure 25. SEM images of 15 mg/mL (a) 1:3, (b) 1:1, and (c) 3:1 v:v CuI:CuSCN composite films spin-coated from DES onto ITO-coated glass substrates.

Complete inverted PSC devices were fabricated with the following HTMs: PEDOT:PSS, 15 mg/mL CuI from MeCN annealed at room temperature for 10 minutes, and 15 mg/mL CuI from MeCN annealed at 100 °C for 10 minutes to obtain preliminary performance metrics. The J-V curves for the best performing devices are shown in Figure 26. Despite its poorer film morphology, the device with an HTM of 15 mg/mL CuI from MeCN annealed at 100 °C for 10 minutes outperformed the other two. This suggests (1) that it is likely that the pinholes of the CuI film do not extend throughout the thickness of the film (otherwise the devices would likely short), (2) that 100 °C annealed CuI HTM films have inherent benefits over room temperature annealed films, and (3) that HTM film morphology is not the only factor influencing device performance.

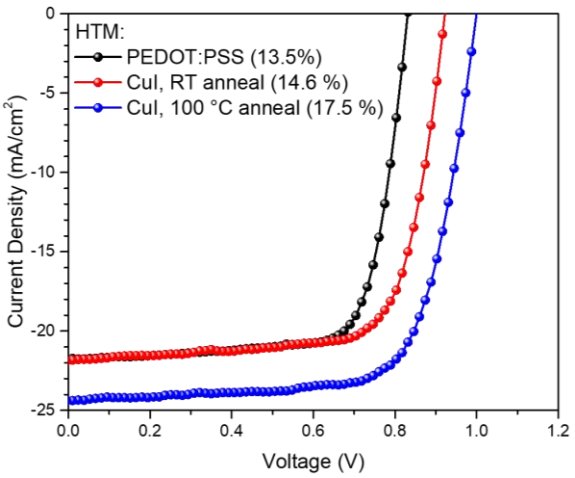

Figure 26. J-V curves for the highest performing inverted $MAPbI_3$ PSCs with three different HTMs.

6.3.2 HTM Film Thickness Optimization for Maximum Device Performance

Complete inverted PSCs employing 100 °C annealed CuI and CuSCN HTMs from MeCN and DES solvents, respectively, were fabricated using concentrations of 1 (0.3 nm), 5 (2.6 nm), 10 (7.1 nm), 15 (15.4 nm), and 30 (27.6 nm) mg/mL to determine the optimum concentration (film thickness) for maximum device performance. The 100 °C annealed Cu-based HTM films were chosen for optimization over the room-temperature annealed Cu-based HTM films due to their superior performance based on preliminary results (Figure 26), and thus will be used throughout the remainder of this study. As shown in Figure 27, the best performing inverted PSCs with a CuI from MeCN HTM occurred at a CuI film thickness of 15.4 nm and the best performing inverted PSCs with a CuSCN from DES HTM occurred at a CuSCN film thickness of 7.1 nm, corresponding to concentrations of 15 and 10 mg/mL, respectively. It should be noted that regardless of film thickness, the CuI-based PSCs outperformed the CuSCN-based PSCs, further indicating that film morphology is not the only factor influencing device performance.

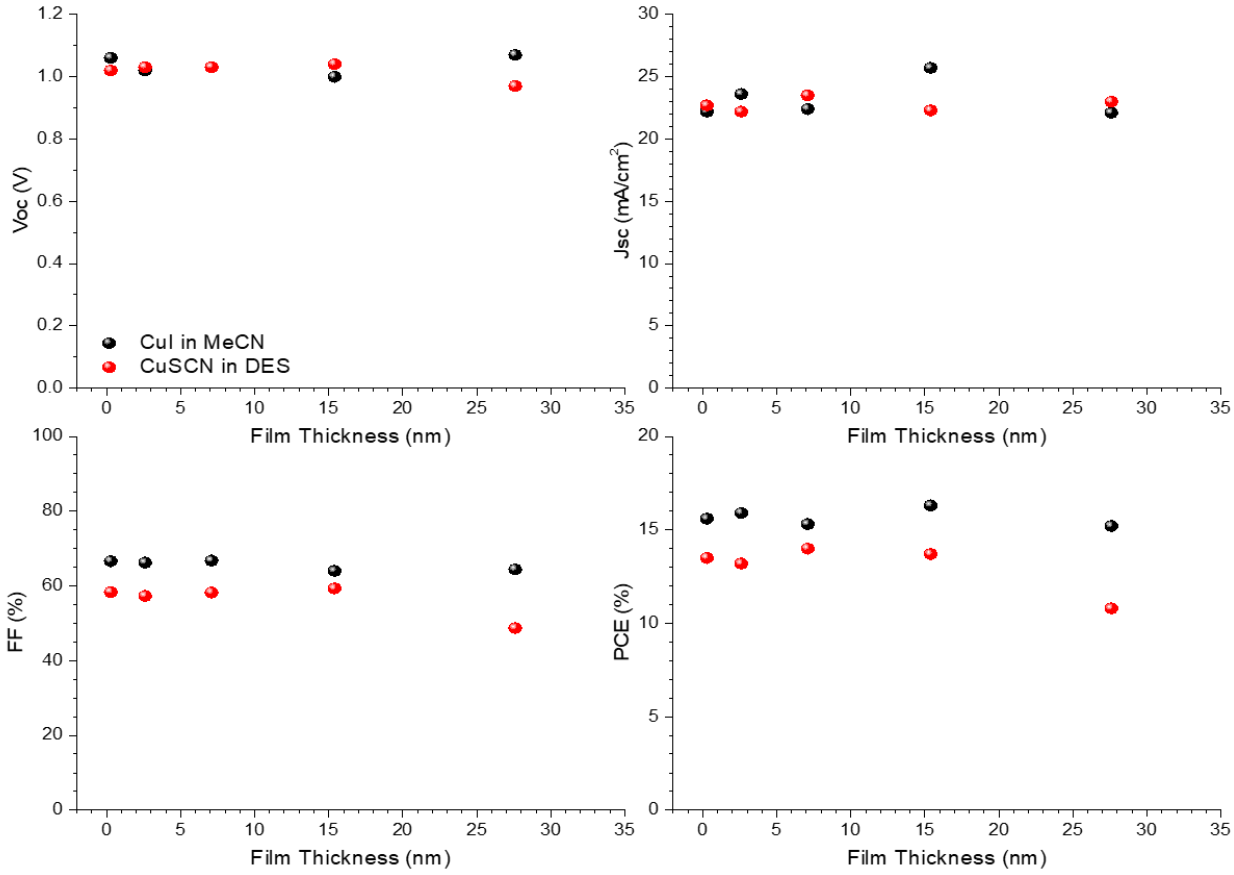

Figure 27. PSC performance metrics for devices made with either a CuI from MeCN HTM or CuSCN from DES HTM of varying thicknesses.

6.3.3 Device Performance Metrics for Complete PSCs with Various HTMs

Complete inverted PSCs employing various HTMs were fabricated, and their average J-V performance metrics are presented in Figure 28. All Cu-based HTMs were 15 mg/mL in DES (or MeCN for one set of CuI) based on the previous film thickness optimization results. Values for those PSCs fabricated with a PEDOT:PSS HTM are also shown in Figure 28 for comparison. Despite its poor film morphology, PSCs fabricated with a CuI from MeCN HTM outperformed all others once again. The lower performance of PSCs with a CuI from DES HTM compared to PSCs with a CuI from MeCN HTM suggests that film morphology is still important; however, it is certainly not the only factor at play since

PSCs with a CuI from MeCN HTM also outperformed PSCs with a PEDOT:PSS and CuI:CuSCN from DES (all volume ratios except 1:0) HTM, all of which had superior film morphology. All of the PSCs fabricated with CuI:CuSCN (3:1, 1:1, and 1:3 v:v) from DES HTMs showed higher efficiencies than PSCs fabricated with a pure CuI from DES or a pure CuSCN from DES HTM, not only suggesting again that morphology may still play a role but also that it is a property (or properties) of CuI that is likely contributing to improved device performance. However, as evidenced by the 1:3 CuI:CuSCN from DES HTM's better performance relative to the 1:1 and 3:1 blends, it appears as though high concentrations of CuI are not necessary.

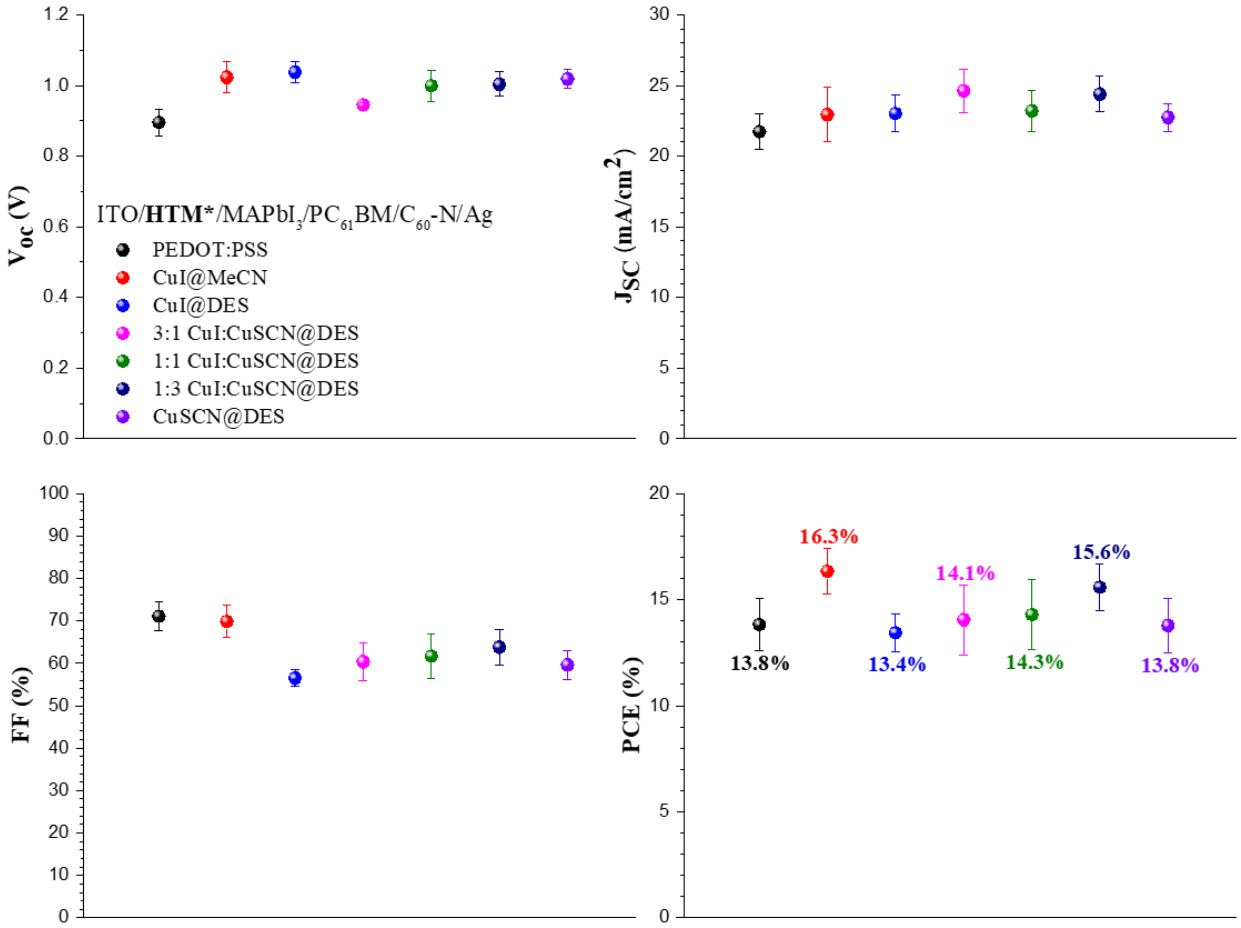

Figure 28. J-V device performance metrics for inverted $MAPbI_3$ PSCs fabricated using different HTMs. All Cu-based HTMs were fabricated from a 15 mg/mL solution.

6.3.4 HTM Film Crystallinity

Powder XRD measurements were performed on various HTMs spin-coated onto ITO-coated glass substrates to examine the relative crystallinity of the films since more crystalline films are often associated with superior charge transport. All Cu-based HTM films were fabricated to be around the same thickness. As shown in Figure 29, PEDOT:PSS and CuSCN films did not show any crystalline peaks, suggesting amorphous films. On the other hand, both CuI films (from DES and MeCN) exhibited a peak around 25°, which corresponds to the (111) crystal plane of γ-CuI. Noticeably, the (111) peak intensity for the CuI from MeCN film is much greater than that of the CuI from DES film, indicating a higher degree of crystallinity in the former.

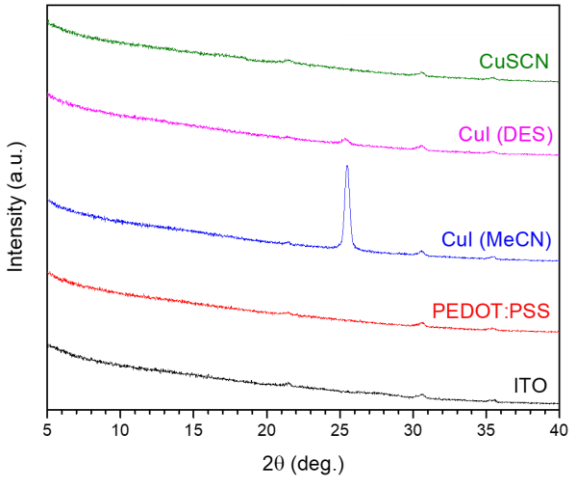

Figure 29. XRD patterns of various HTMs prepared on ITO-coated glass substrates. All Cu-based HTMs were prepared to be around the same thickness for comparative purposes. The XRD pattern of bare ITO is shown for reference.

The XRD patterns for the 15 mg/mL in DES CuI:CuSCN (all volume ratios) films prepared on ITO are shown in Figure 30. The (111) γ-CuI peak around 25° remains present for the 3:1 composite film but disappears as the volume % of CuSCN increases to 50%, at which point the composite films appear amorphous.

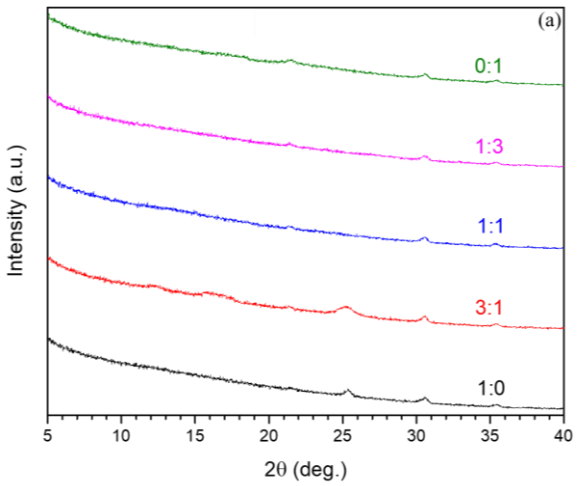

Figure 30. XRD images of 15 mg/mL blends of CuI:CuSCN spin-coated from DES onto ITO-coated glass substrates. All Cu-based HTMs were prepared to be around the same thickness for comparative purposes.

The stronger crystalline nature of CuI from MeCN films relative to PEDOT:PSS films and CuI:CuSCN (all volume ratios) from DES films may result in superior charge transport in the CuI from MeCN films (and could be a reason for CuI's higher observed effective hole mobility in Table 3), which could be one factor contributing to the higher observed efficiencies of PSCs fabricated with CuI from MeCN HTMs. Of course, if crystallinity were the only contributing factor, one would expect to see higher average efficiencies with PCSs fabricated with the 3:1 and 1:1 v:v CuI:CuSCN from DES HTMs over those with the 1:3 CuI:CuSCN from DES HTM, which is opposite from what is observed (Figure 28). As such, it is clear that both HTM film morphology and crystallinity play a role in overall PSC device performance. Nevertheless, HTM film crystallinity and morphology alone still do not explain all of the device performance trends observed in Figure 28.

6.3.5 Perovskite Film Morphology and Crystallinity on Different HTM Surfaces

To further understand why PSCs with a PEDOT:PSS HTM were outperformed by those with a CuI from MeCN HTM, SEM (Figure 31) and XRD (Figure 32) were used to examine the surface morphology and crystallinity, respectively, of $MAPbI_3$ perovskite films grown on either PEDOT:PSS or CuI from MeCN surfaces. While both $MAPbI_3$ perovskite film surfaces showed no evidence of pinhole formation regardless of the underlying substrate, the grains of the $MAPbI_3$ formed on CuI are visibly larger on average than those formed on PEDOT:PSS (Figure 31). The XRD patterns further corroborate this finding as the (110) and (220) perovskite peaks of the $MAPbI_3$ perovskite grown on CuI show a greater intensity than those $MAPbI_3$ perovskite films of the same thickness grown on PEDOT:PSS, indicating a higher degree of crystallinity (Figure 32a). PSCs with active layer perovskite films of larger grain sizes often show enhanced performance over those with smaller grains due to improved charge transport as a result of a lack of grain boundary induced recombination and charge trap sites.

Figure 32b shows the XRD patterns of $MAPbI_3$ perovskite films (all the same thickness) grown on various Cu-based HTM film surfaces. Unlike what was observed between PEDOT:PSS and CuI, there was no noticeable differences in the relative intensities of these $MAPbI_3$ perovskite films. Ultimately, it appears as though $MAPbI_3$ perovskite crystallizes to the same degree on surfaces of CuI, CuSCN, or blends of the two.

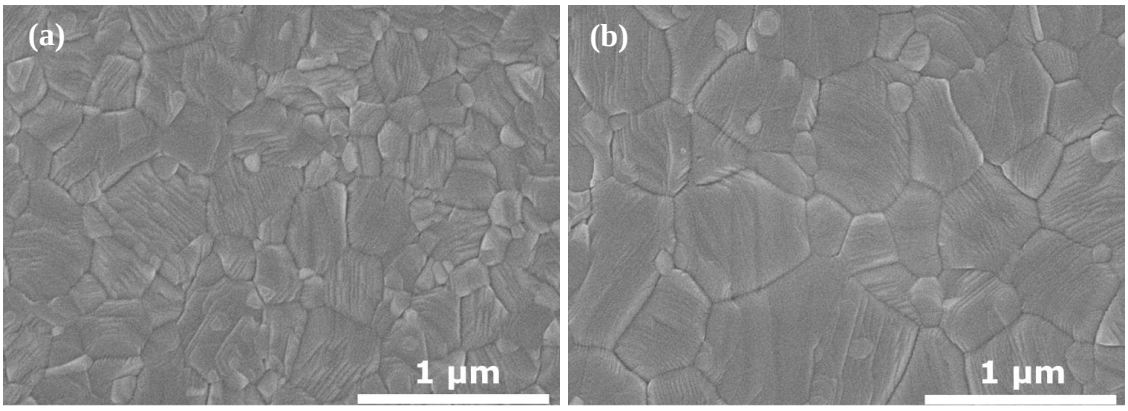

Figure 31. SEM images of $MAPbI_3$ perovskite films grown on (a) PEDOT:PSS and (b) CuI surfaces.

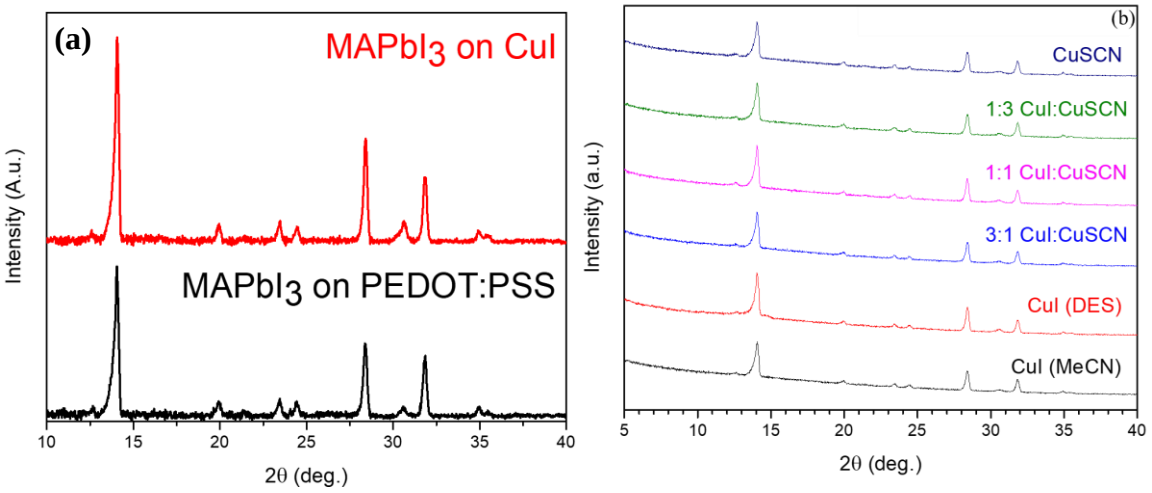

Figure 32. XRD patterns for (a) $MAPbI_3$ perovskite films grown on PEDOT:PSS and CuI surfaces, and (b) $MAPbI_3$ perovskite films grown on different Cu-based HTMs. All $MAPbI_3$ perovskite films were prepared to be around the same thickness for comparative purposes.

6.3.6 HTM Film Optics

The amount of light that is able to be absorbed by the $MAPbI_3$ perovskite active layer is directly dependent on the amount of light that is allowed to transmit through the ITO-coated glass and HTM film. The optical absorbance and transmission spectra for PEDOT:PSS, pure CuI from MeCN, pure CuI from DES, pure CuSCN from DES, and

CuI:CuSCN (3:1, 1:1, and 1:3 v:v) blends from DES spin-coated on ITO-coated glass are shown in Figures 33a and 33b, respectively. The absorbance and transmission spectra for ITO-coated glass are also shown for reference. Note that the average transmission for the ITO shown in Figure 33b is lower than that of each ITO/HTM due to the reflectance of the bare ITO-coated glass substrate. Due to their being wide-bandgap semi-conductors, the Cu-based HTM films have a small absorbance in the low-wavelength region of the visible and ultraviolet spectra. The films of PEDOT:PSS, pure CuI from MeCN, and pure CuSCN from DES had an ~86% average transmission in the visible region from 400-800 nm. The average transmission in the 400-800 nm visible region was 85-86% for the CuI:CuSCN composite films on ITO, with the average transmission increasing by about 0.5% with increasing CuSCN content. CuI from DES had an ~4% lower average transmission of ~82% likely due to its inferior film quality. At 550 nm, CuI from MeCN had a transmission of ~90%, which is ~2% higher than that of PEDOT:PSS (~88%), ~3% higher than that of CuSCN from DES (~87%), ~4% higher than those of the three CuI:CuSCN composite blends (~86% for each), and ~5% higher than that of CuI from DES (~85%). The improved transmission for CuI from MeCN films on ITO-coated glass is yet another factor that could be contributing to the higher observed efficiencies of PSCs fabricated with CuI from MeCN HTMs. Additionally, the improved average transmission with increasing CuSCN content could be one factor contributing to why PSCs fabricated with 1:3 CuI:CuSCN from DES HTMs outperform PSCs fabricated with either 1:1 or 3:1 CuI:CuSCN HTMs.

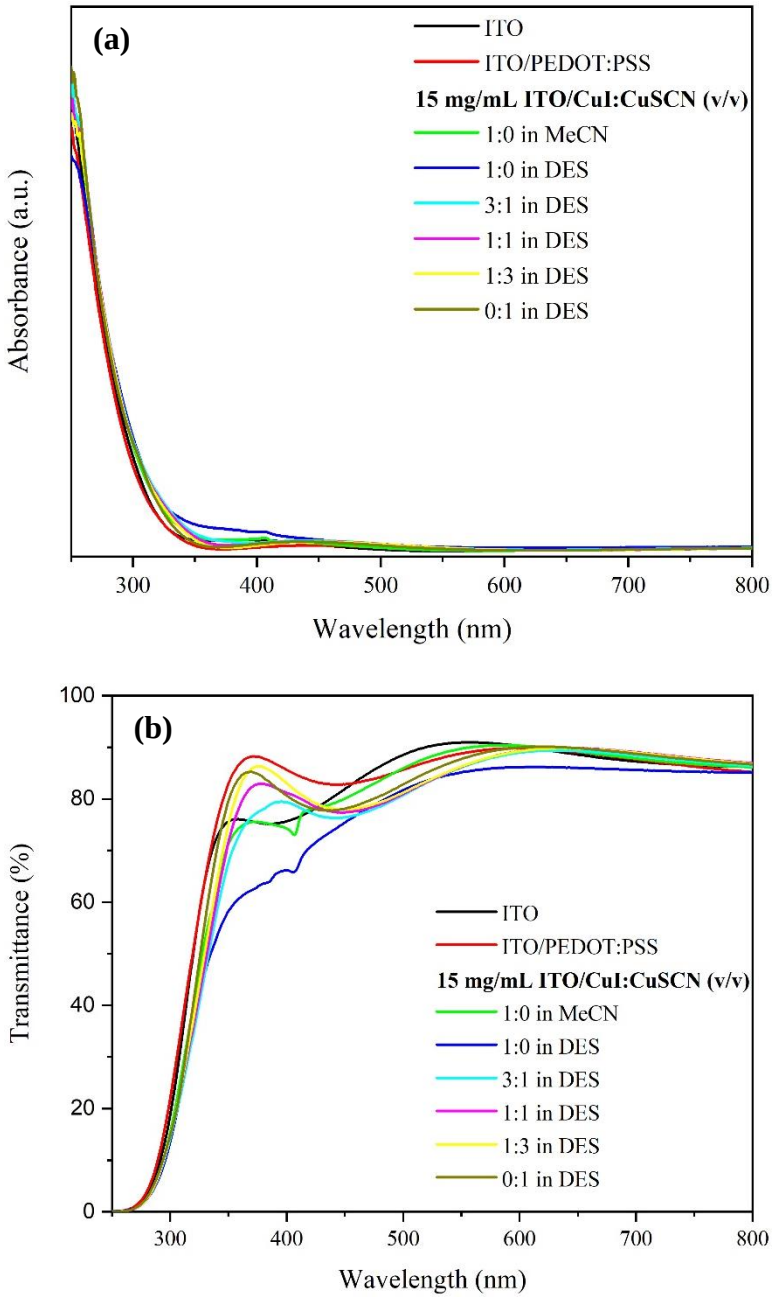

Figure 33. Optical absorbance (a) and transmission (b) spectra for PEDOT:PSS, CuI from MeCN, and CuI:CuSCN (1:0, 3:1, 1:1, 1:3, and 0:1 v:v) from DES films on ITO-coated glass substrates. The spectra for the ITO-coated glass are also shown for reference. All Cu-based HTM films were deposited from 15 mg/mL solutions.

6.3.7 HTM Film Electronic Band Levels

Proper band level alignment between the valence bands of the HTMs and the $MAPbI_3$ perovskite is important for efficient hole extraction and transport to the conducting electrode. Charge carrier recombination is also less likely to occur the better the band levels match up. Figure 34 (top panel) gives the UPS secondary electron cutoffs for bare ITO-coated glass, PEDOT:PSS deposited on ITO, 15 mg/mL CuI from MeCN deposited on ITO, and each 15 mg/mL CuI:CuSCN volume ratio from DES deposited on ITO, which allow for the calculation of each film's effective work function. Figure 34 (bottom panel) gives the low-binding-energy onsets, which, along with the calculated work function, provides the information needed to estimate the HOMO or valence band (VB) levels for each semiconducting film. The calculated work functions and corresponding HOMO/VB levels (if applicable) for bare ITO-coated glass, PEDOT:PSS deposited on ITO, 15 mg/mL CuI from MeCN deposited on ITO, and each 15 mg/mL CuI:CuSCN volume ratio from DES deposited on ITO are shown in Table 3. The VB levels for the Cu-based HTMs tend to increase with increasing CuSCN content. Compared to the VB level of ~5.45 eV for $MAPbI_3$, all Cu-based HTMs have excellent band alignment, aside from CuSCN. The higher VB level of CuSCN (5.6 eV) relative to that of $MAPbI_3$ could lead to increased series resistance during carrier transport, which would decrease the resulting FF and thus the overall efficiency of the solar cell. Additionally, the poorer work function-VB match of the PEDOT:PSS HTM (5.0 eV) with $MAPbI_3$ relative to the CuI-containing HTMs (5.35-5.45 eV) would indicate increased chances for recombination in PEDOT:PSS HTM-based PSC, which would result in a lower V_{oc} and thus a decrease in the overall efficiency of the solar cell.

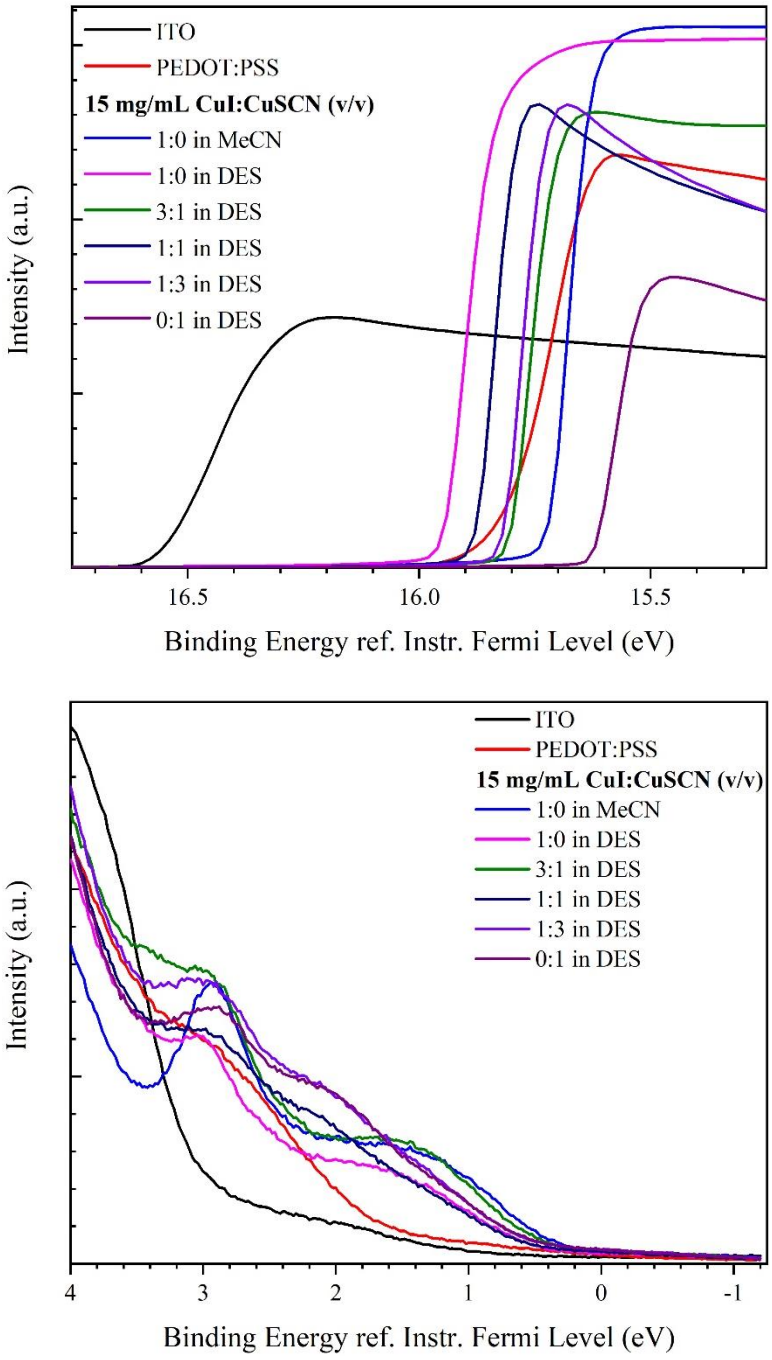

Figure 34. UPS spectra of ITO, PEDOT:PSS-covered ITO, and CuI:CuSCN-covered ITO for various volume ratios of CuI and CuSCN in MeCN or DES.

Table 3. Calculated work functions and HOMO/VB levels for various HTMs deposited on UV-O_3 ITO-coated glass. Bare UV-O_3 ITO and $MAPbI_3$ are both shown for reference. All Cu-based HTM films were deposited from a 15 mg/mL solution. The error is ± 0.5 eV.

HTM	Work Function (eV)	δ HOMO (eV)	HOMO/VB Level (eV)
ITO	4.50	-	-
$MAPbI_3$	-	-	5.45
PEDOT:PSS	5.00	-	-
CuI from MeCN	5.30	0.1	5.40
1:0 CuI:CuSCN from DES	5.10	0.25	5.35
3:1 CuI:CuSCN from DES	5.30	0.1	5.40
1:1 CuI:CuSCN from DES	5.20	0.2	5.40
1:3 CuI:CuSCN from DES	5.25	0.2	5.45
0:1 CuI:CuSCN from DES	5.45	0.15	5.60

6.4 Conclusions

Despite their other advantages (e.g. higher conductivity and economical), inorganic thin films as charge transporting layers often have poorer film morphologies than their organic counterparts. Preliminary device performance data for PSCs fabricated with either an organic PEDOT:PSS or an inorganic Cu-based HTM revealed that, though still relevant, film morphology is not the sole deciding factor for final device performance as devices employing pinhole-containing CuI from MeCN HTMs outperformed those with uniform HTM films from PEDOT:PSS or CuI:CuSCN (3:1, 1:1, 1:3, or 0:1 v:v) from DES blends. In an effort to better understand the performance trends observed with devices employing the different HTMs, HTM film optics, crystallinity/charge transport potential, and electronic energy levels as well as $MAPbI_3$ perovskite film crystallinity and morphology on various HTM surfaces were investigated. Table 4 summarizes the results from this study by assigning corroborative numerical rankings to each HTM based on their performances during each of these experiments. The rankings were not arbitrary, but rather given based on quantitative data or qualitative results. The scores for each HTM were then averaged

and compared to how each HTM ranked performance-wise when used in a complete PSC. Amazingly, the ranking trends were identical, which confirms that the efficacy of these HTMs in complete PSCs is dependent on the additive benefits from all relevant film/material properties (i.e. morphology, optics, crystallinity/charge transport potential, and electronic band level alignment).

Table 4. Summary, using corroborated numerical rankings, of how each HTM performed relative to one another during each experiment throughout the study. The right side of the table compares the overall ranking of each HTM (determined by averaging their rankings from the left side of the table) to how they ranked based on the performance of the PSCs in which they were used.

HTM	Morphology	Optics	Crystallinity/ Charge Transport Potential	VB Alignment	Overall Ranking (Avg. Score)	Device Performance Ranking
PEDOT:PSS	1	2	7	7	5 (4.25)	5
CuI from MeCN	6	1	1	2	1 (2.50)	1
1:0 CuI:CuSCN from DES	7	7	2	5	7 (5.25)	7
3:1 CuI:CuSCN from DES	5	6	3	2	4 (4.00)	4
1:1 CuI:CuSCN from DES	4	5	4	2	3 (3.75)	3
1:3 CuI:CuSCN from DES	3	4	5	1	2 (3.25)	2
0:1 CuI:CuSCN from DES	2	3	6	6	5 (4.25)	5

Despite its poorer film morphology, PSCs fabricated using CuI from MeCN HTMs still outperformed all others due to the HTM's exceptional optical, crystallinity/charge transport potential, and VB alignment properties. Meanwhile, PSCs fabricated using HTMs like PEDOT:PSS and CuSCN from DES (which had great film morphology and optics but inferior crystallinity/charge transport potential and VB alignment to $MAPbI_3$ compared to all other HTMs) or CuI from DES (which had better crystallinity/charge transport potential and VB alignment to $MAPbI_3$ but inferior film morphology and optics compared to all other

HTMs) gave subpar device efficiencies due to the negative drawbacks brought forth by certain film/material properties of their HTMs. For the 3:1, 1:1 and 1:3 v:v CuI:CuSCN blends from DES HTMs, it was the small, though still slightly better, differences in morphology, optics, and especially VB alignment to $MAPbI_3$ that made PSCs fabricated with the 1:3, 1:1 and 3:1 CuI:CuSCN blends from DES HTMs achieve the second, third, and fourth highest average efficiencies, respectively. All in all, it is recommended that researchers consider all film and material properties (perhaps those that were not even mentioned in this study) of a charge transport layer before choosing the one they wish to optimize and use within their solar cell. Of course, it should be noted that long term stability, toxicity, and cost were factors not considered here that may influence a researcher to choose a lesser performing HTM over a higher performing HTM in their devices.

CHAPTER 7

GRAPHENE AS A PROTECTIVE OVERLAYER IN PEROVSKITE SOLAR CELLS FOR STABILITY ENHANCEMENT

7.1 Introduction

Since their first appearance in 2009, the maximum power conversion efficiency (PCE) achieved by hybrid organic-inorganic perovskite solar cells (PSCs) has drastically improved from an initial 3.81%[20] to over 25%.[5] While the performances of PSCs now rival those of crystalline silicon-based solar cells, their poor stability in the presence of moisture[150–153], high temperatures[154–156], and prolonged light exposure[108,157–159] remains one of the major issues deterring their immediate commercialization.

Graphene is a single-atom-layer thick material comprised of sp^2-bonded carbon atoms arranged in a hexagonal lattice of aromatic rings. Due to its structure, graphene has remarkable in-plane thermal and electrical conductivity,[160] impressive flexibility,[161] and high molecular impermeability;[162,163] in fact, it has been shown that even molecules as small as O_2 cannot permeate through pristine graphene under thermal equilibrium. High-quality, large-area graphene can be easily produced through chemical vapor deposition (CVD) processing, and later it was revealed that roll-to-roll production of this material was also possible.[164,165] Because of these properties, graphene is an attractive material for use in PSCs to improve their stability. With its high impermeability, graphene can effectively block water and the metal ions of the top electrode from diffusing into the perovskite active layer. Additionally, charge transport within the device will be uncompromised as electrons can easily tunnel through a single atomic layer of graphene. Lastly, its proven roll-to-roll compatibility would allow for graphene to continue to be used in larger area PSCs.

Herein, large area, continuous monolayer CVD graphene was effectively adhered to the surface of $MAPbI_3$ perovskite films using a versatile orthogonal solvent-assisted pseudo dry transfer process. Perovskite films with a protective graphene layer showed improved moisture and thermal stability compared to those films without graphene. Complete PSCs with and without a graphene barrier layer were also constructed. Under unfavorable moisture and thermal conditions for $MAPbI_3$ perovskites, complete PSCs with graphene outlasted their no-graphene counterparts in terms of performance.

7.2 Experimental

7.2.1 Preparation of Solutions

A polyvinyl formal (Formvar) graphene transfer medium was prepared by dissolving Formvar resin in chloroform (Fisher) at room temperature at a ratio of 100 mg Formvar per 1 mL chloroform. A copper iodide (CuI) solution was prepared by dissolving 15 mg CuI (Alfa Aesar) in 1 mL acetonitrile (anhydrous, Acros) for 2 h at room temperature, and then filtering with a 0.45 μm PTFE filter. To prepare the PbI_2(DMSO) complex solution, a 1:1 molar ratio of lead iodide (PbI_2) (Alfa Aesar) and dimethyl sulfoxide (DMSO) (anhydrous, Acros) was dissolved fully at room temperature in N,N-dimethylmethanamide (DMF) (anhydrous, Acros), and then filtered with a 0.45 μm PTFE filter. Specifically, 461 mg PbI_2/944 mg DMF and 78 mg DMSO/944 mg DMF were used for a 1.0 M PbI_2(DMSO) complex solution. A methylammonium iodide (MAI) solution was prepared by fully dissolving 60 mg MAI (Greatcell Solar) in 1 mL 2-propanol (anhydrous, Acros), and then filtering with a 0.45 μm PTFE filter. A phenyl-C61-butyric acid methyl ester (PCBM) solution was prepared by dissolving 10 mg of PCBM (nano-C) in 1 mL chlorobenzene

(anhydrous, Sigma-Aldrich) at 55 °C overnight, cooling to room temperature while stirring, and then filtering with a 0.45 μm PTFE filter. A C_{60}-N cathode interlayer solution was prepared by dissolving 3 mg C_{60}-N (1-Material) in 1 mL 2,2,2-trifluoroethanol (TFE) (Acros) overnight, and then filtering with a 0.45 μm PTFE filter.

7.2.2 Graphene Synthesis

Continuous, monolayer graphene was synthesized on 3 in^2 sheets of 35 μm copper (Cu) foil (Graphene Platform) by chemical vapor deposition in a quartz tube furnace (Planar Tech). Prior to growth, the Cu foil was pre-cleaned with DI water and ethanol (Fisher), and then dried with N_2. The Cu foil was annealed under low pressure (2 torr) and 1020 ℃ with a gas flow of 20 SCCM of H_2 for 2 h. To begin the graphene growth, 10 SCCM of CH_4 was introduced to the chamber (still at 1020 ℃ and 2 torr) for 20 min, followed by a rapid cooling to room temperature under a gas flow of 20 SCCM of H_2 and 20 SCCM of Ar. Following the growth, the graphene/Cu foil sheets were adhered to thermal release tape (TRT) (Graphene Supermarket) and cut into smaller 15 cm^2 squares for the transfer process.

7.2.3 Graphene Transfer

A 15 cm^2 graphene/Cu foil/TRT square was placed in a glass dish against the wall at a 60° incline with the graphene side facing upwards. A pipet was used to evenly coat the graphene surface with the Formvar solution. The Formvar/graphene/Cu foil/TRT was dried for 15 min, baked at 100 °C to remove the TRT, and then floated (graphene side up) atop a 1:1 volume ratio DI water and ferric chloride copper etchant solution (MG Chemicals).

After 3 min, the Formvar/graphene/Cu foil was removed, and the bottom (non-graphene side) of the substrate was washed with DI water to remove any backside graphene. The Formvar/graphene/Cu foil was then placed atop a 3:1 volume ratio DI water and ferric chloride copper etchant solution with the graphene side up. After 45 min, the Cu foil was dissolved, leaving only graphene adhered to the Formvar. The free-standing Formvar/graphene was washed thoroughly by floating in several baths of DI water to remove any remaining copper etchant solution, and then placed gently between two cleanroom wipe squares to dry. The free-standing Formvar/graphene was moved to an N_2-glovebox (N_2 and O_2 < 5.0 ppm) for the remainder of the transfer. In the glovebox, 100 µL of n-butanol (Fisher) was used to cover the surface of a $MAPbI_3$ perovskite film. The free-standing Formvar/graphene was gently placed (graphene side down) atop the $MAPbI_3$/n-butanol such that it covered the entire surface of the perovskite. A Teflon rod was rolled over the system to enhance the contact between the graphene and the perovskite before transferring the device to a hot plate set to 50 °C. The device was baked for 15 min to further promote the graphene adhesion and to remove any remaining butanol. Once cooled to room temperature, the device was placed in a chloroform (Fisher) bath for 2 min, removed, and washed with additional chloroform to fully remove the Formvar layer, leaving only the graphene adhered to the perovskite film.

7.2.4 Solar Cell Device Fabrication

Patterned indium-doped tin oxide (ITO) substrates (20 Ω/sq, 14.7 cm^2, Thin Film Devices) were cleaned with a 2% Mucasol™ (Sigma-Aldrich) soap solution, deionized water, acetone (Fisher), and 2-propanol (Fisher) (in that order) with 10 min of ultra-sonication at

each step, followed by drying in an oven at 140 °C overnight. Prior to use, the cleaned ITO substrates were exposed to UV/Ozone treatment for 20 min. Following the cleaning and surface polarization, the ITO substrates were transferred to an N_2-glovebox (N_2 and O_2 < 5.0 ppm) for the remainder of the procedure. 50 μL of the CuI solution were spun onto the bare ITO at 3000 rpm for 60 s, and then annealed at 100 °C for 10 minutes. Once cooled to room temperature, 50 μL of the PbI_2(DMSO) complex solution was spun onto the CuI-coated substrates at 1500 rpm for 15 s, immediately followed by a spin-coating of 100 μL of the MAI solution at 2500 rpm for 30 s. The resulting perovskite film was annealed at 100 °C for 1 hr in the dark. After the $MAPbI_3$ perovskite was formed and the substrate cooled to room temperature, 50 μL of the PCBM solution was spun onto the perovskite film at 1000 rpm for 30 s. Following a previous report,[107] the films were covered with a petri dish and allowed to solvent anneal in the dark for 24 hours. The perovskite devices were completed by spin-coating 80 μL of the C_{60}-N solution at 4000 rpm for 60 s, followed by thermal evaporation of a 100 nm thick Ag electrode at a base pressure of 3×10^{-6} mbar through a shadow mask. An overlap of the Ag electrode and patterned ITO substrate defined a device area of 0.06 cm^2. For the devices with the graphene layer, monolayer graphene was transferred onto the $MAPbI_3$ perovskite prior to the deposition of the PCBM.

7.2.5 Inductively Coupled Plasma Mass Spectroscopy

After the complete PSCs with or without the graphene barrier layer were subjected to the thermal annealing treatment for 12 hours at 85 °C, scotch tape was used to remove the Ag electrodes from the tops of the devices. This process was repeated two additional times to ensure the Ag electrodes had been thoroughly removed. The PCBM layers were removed

by submerging the samples in a chlorobenzene bath for 5 min. The samples, now with the perovskite layer as the top layer, were then rinsed with additional chlorobenzene, dried with a nitrogen gun, and then placed in separate vials each containing 5 mL of 4:1 HCl (37%)/HNO_3 (67%) aqua regia for 12 hours to dissolve. The aqua regia solutions were transferred to 15 mL Falcon tubes and diluted in a 5:7 v/v ratio with water. ICP-MS analysis was performed with a Perkin-Elmer NexION 350D ICP-MS on the aqua regia solutions. The detection limit for Ag was ~0.1 ng in 1 mL of the solution.

7.2.6 Characterization

Current−voltage (*J-V*) curves were tested inside a N_2-glovebox using a Keithly 2400 source-meter under simulated AM 1.5G solar irradiation at 100 mV/cm^2 light intensity. The light source was a 300 W Xe lamp (Newport 91160) that was adjusted with an NREL-calibrated Si reference solar cell and KG-5 filter. No photomask was used for the J-V measurements. X-ray diffraction (XRD) measurements were made with a PANalytical X'Pert^3 X-ray diffractometer having a Ni filter, 1/2 in. diverging slit, vertical goniometer, and X'Celerator detector. Measurements were made under Cu Kα (λ = 1.542 Å).

7.3 Results and Discussion

Large area, continuous monolayer graphene was grown on copper (Cu) foil using a low-pressure CVD method. Raman spectroscopy was performed to determine the crystalline quality of the graphene. According to Figure 35, the Raman spectrum shows three Raman peaks at 1341 cm^{-1} (D band), 1584 cm^{-1} (G band), and 2668 cm^{-1} (2D band). The intensity

(*I*) ratio I_{2D}/I_G for the 2D to G bands is about 2.95, which is consistent with that of monolayer graphene (~2-3).[166,167]

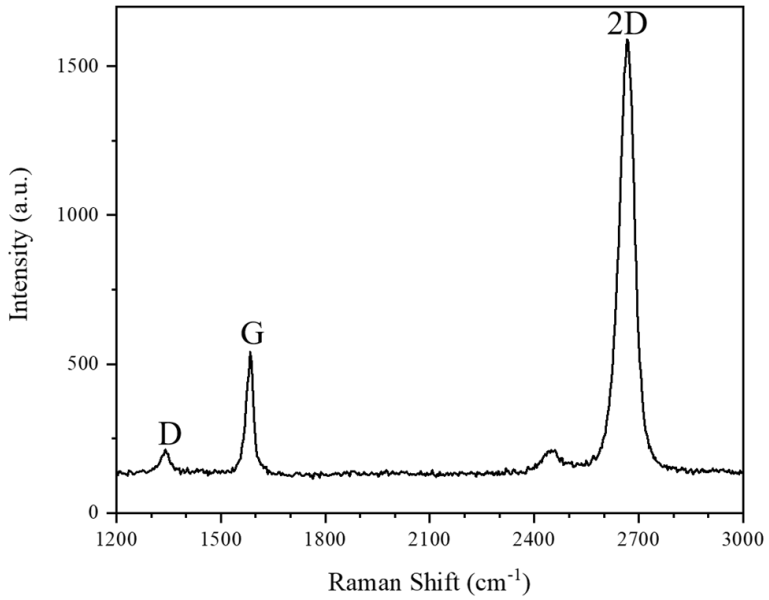

Figure 35. Raman spectrum of monolayer graphene transferred onto an SiO_2/Si substrate.

Generally, a wet transfer process is used to adhere graphene to a target substrate.[168] In this case, graphene attached to a polymer support (typically poly(methyl methacrylate), PMMA) is floated on the surface of water so that a target substrate can then be used to scoop up the graphene. The graphene adheres to the target substrate after heating and drying. If a PMMA support is used, the substrate with the PMMA/graphene is immersed in a hot acetone bath to remove the PMMA, leaving just the graphene adhered to the target substrate. Unfortunately, this transfer process does not work with a perovskite substrate since submersion in water will quickly degrade the perovskite film. Furthermore, a support layer other than PMMA is necessary since a hot acetone bath will also degrade the perovskite film. As such, for this study a pseudo dry transfer process with a thick polyvinyl formal (Formvar) support was used, based on a previous report.[169] The thicker support

layer allowed for a freestanding Formvar/graphene film that could be easily transferred to a target surface. Instead of water, an orthogonal solvent (i.e. n-butnaol) was used to adhere the Formvar/graphene to a $MAPbI_3$ perovskite film. The Formvar support was easily removed by submerging the Formvar/graphene/$MAPbI_3$ in a chloroform bath, leaving just the graphene adhered to an undamaged $MAPbI_3$ film. A more detailed description of this transfer process can be found in **Experimental**. It should be noted that this transfer process can be used to adhere graphene to any film surface provided it does not degrade in the chloroform needed to remove the Formvar.

7.3.1 Moisture Stability

To determine if graphene could effectively inhibit water ingress into the perovskite film, $MAPbI_3$ perovskite films with and without a graphene barrier layer (prepared on glass) were placed in an ambient environment controlled to 30-50% relative humidity (Figure 36). The films were left under these conditions for one week, only to be removed at different time periods for stability analyses.

Figure 36. Apparatus used to maintain a controlled humidity environment in air during moisture stability studies. The relative humidity inside the container was kept between 30-50%.

Since the presence of PbI_2 is a good indicator of perovskite film degradation, powder x-ray diffraction (XRD) was used to measure film stability in the presence of moisture. As shown in Figure 37a, for the films without a graphene barrier layer, the (001) diffraction peak for PbI_2 around 12.2° began to appear after just 1 day. After 4 days the relative intensity of the PbI_2 surpassed that of the $MAPbI_3$, and by day 7 the film had completely degraded to pure PbI_2. Conversely, for films with the graphene barrier layer, only a small amount of PbI_2 was detected in the film after one week (Figure 37b). It was observed that a small amount of PbI_2 began to form around the edges of the $MAPbI_3$ film with graphene (Figure 38f). Since graphene was only encapsulating the surface of the perovskite, it is very likely that this slight degradation was due to water penetration from the edges of the film. Nevertheless, it is evident from these results that the graphene was able to effectively

protect the $MAPbI_3$ perovskite film from water penetration in a humid ambient environment.

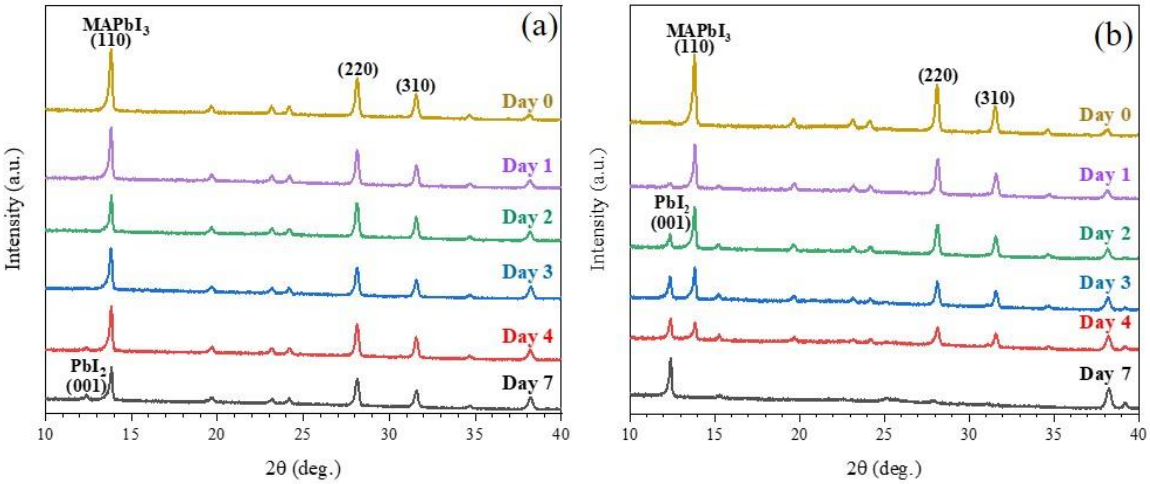

Figure 37. Evolution of $MAPbI_3$ XRD patterns with (a) and without (b) a graphene barrier layer during storage in air at 30-50% relative humidity for one week.

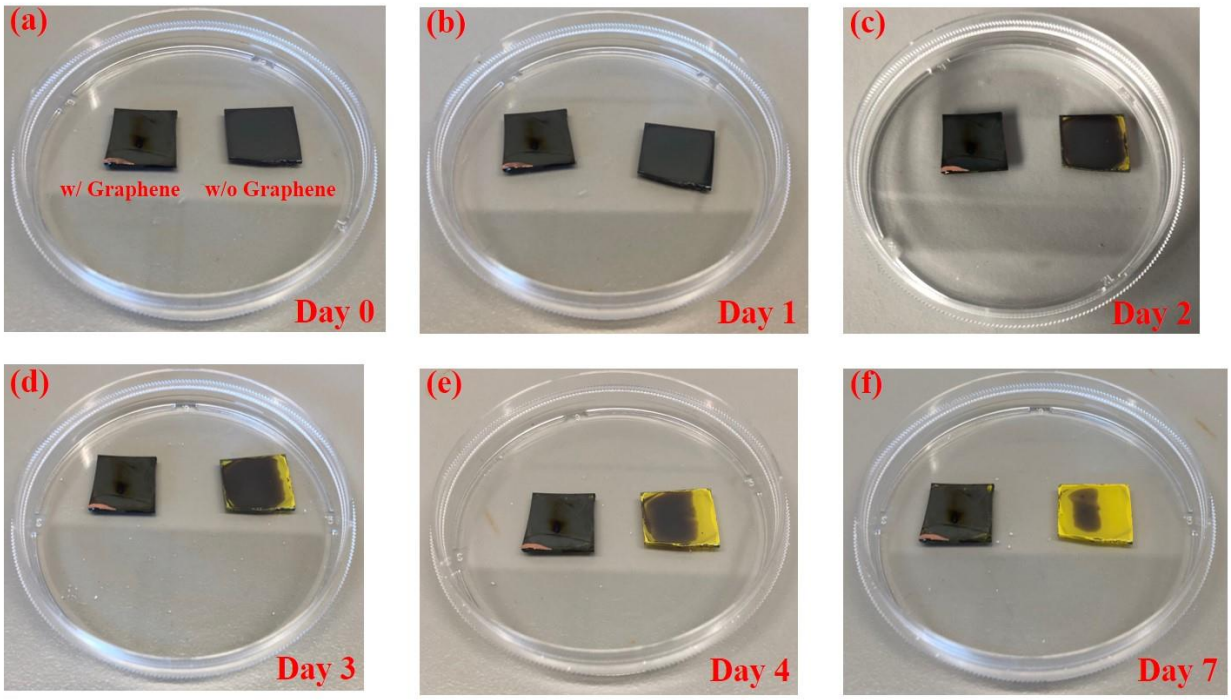

Figure 38. $MAPbI_3$ films on glass substrates with or without a graphene barrier layer during storage in air at 30-50% relative humidity for one week.

Complete PSCs were fabricated in the inverted, planar p-i-n architecture with or without a graphene barrier layer between the $MAPbI_3$ active layer and the phenyl-C61-butyric acid methyl ester (PCBM) electron transport material (ETM) (Figure 39). Copper iodide (CuI) was chosen as the hole transport material (HTM) in this study over the commonly used poly(3,4-ethylenedioxythiophene) polystyrene sulfonate (PEDOT:PSS) HTM due to its superior stability in $MAPbI_3$ PSCs (Figure 40) and lower acidity.[144]

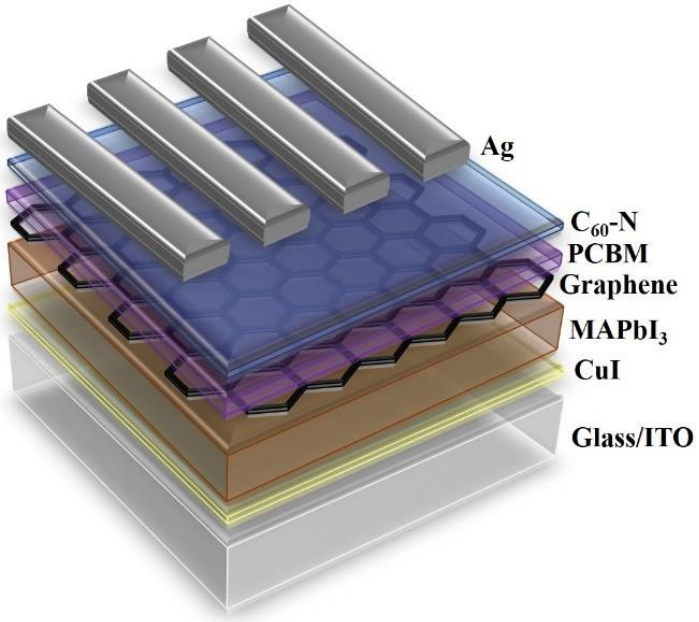

Figure 39. Schematic of the inverted structure, planar p-i-n PSC. Note that the graphene layer may or may not be included in the final device architecture.

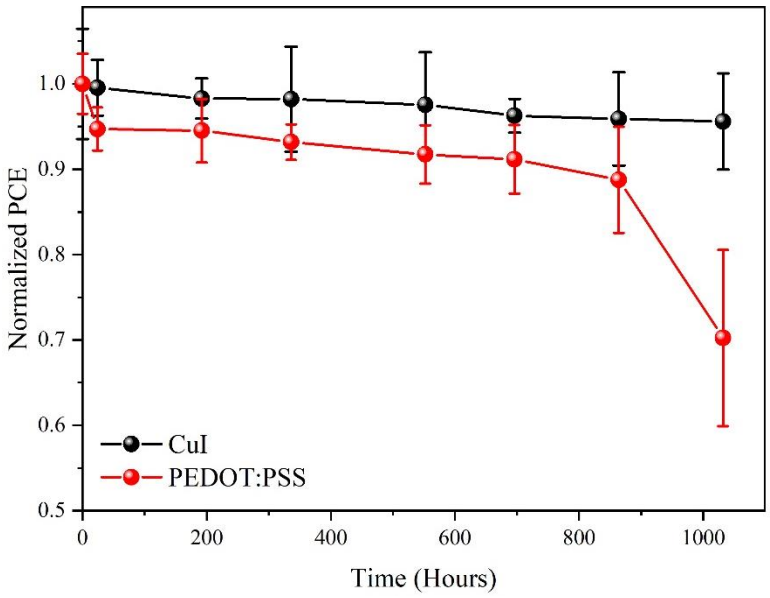

Figure 40. The change in normalized PCE over 1032 hours for $MAPbI_3$ PSCs fabricated with a PEDOT:PSS or CuI HTM. Except when tested, devices were left in the dark in an inert N_2 atmosphere. The testing was performed in an inert N_2 atmosphere.

The current-voltage (J-V) characteristics for the highest performing devices with and without the graphene barrier layer are presented in Figures 41a and 41b. On average, devices with the graphene barrier layer gave V_{oc} = 1.04 V, J_{sc} = 20.5 mA/cm^2, FF = 77.6%, and PCE = 16.6%; and devices without the graphene barrier layer gave V_{oc} = 1.05 V, J_{sc} = 19.8 mA/cm^2, FF = 73.4%, and PCE = 15.2%. As expected, the presence of graphene did not affect the overall performance of the device; however, it was observed that devices with graphene showed slightly greater hysteresis compared to those without graphene. It has been reported that inverted PSCs with a PCBM ETM showed minimal (if any) hysteresis since the PCBM is able to effectively passivate surface and grain boundary trap states within the perovskite layer.[170] Here, though, there is an impermeable graphene layer between the perovskite and the PCBM, which is likely prohibiting the PCBM from passivating the perovskite trap states. Efforts are currently underway to develop a

perovskite film fabrication procedure that includes trap state passivation so as to eliminate the need for PCBM to fulfill this role. It should also be mentioned that the FF for devices with a graphene barrier layer was higher on average than that for devices without a graphene barrier layer. We hypothesize that the cause for this is that the graphene barrier layer is hindering the migration of mobile MA^+ or I^- ions within the perovskite active layer, which improves the series resistance of the solar cell, and thus the resulting FF. Of course, additional investigation is required for corroboration of this theory.

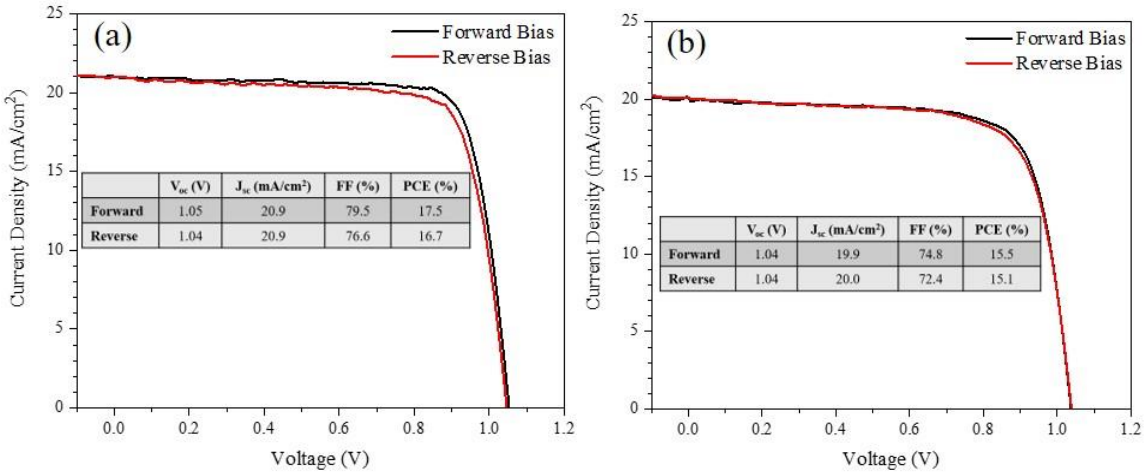

	V_{oc} (V)	J_{sc} (mA/cm²)	FF (%)	PCE (%)
Forward	1.05	20.9	79.5	17.5
Reverse	1.04	20.9	76.6	16.7

	V_{oc} (V)	J_{sc} (mA/cm²)	FF (%)	PCE (%)
Forward	1.04	19.9	74.8	15.5
Reverse	1.04	20.0	72.4	15.1

Figure 41. J-V curves with corresponding performance parameters (insets) for the highest performing PSCs with (a) and without (b) a graphene barrier layer.

To measure the PSC performance over time, complete devices with and without a graphene barrier layer were placed an ambient environment controlled to 30-50% relative humidity. At various time periods, the devices were removed from the controlled environment and transferred into a nitrogen glovebox for testing. After testing, the devices were immediately returned to the controlled environment. Images of the full devices during the week-long ageing process are shown in Figure 42.

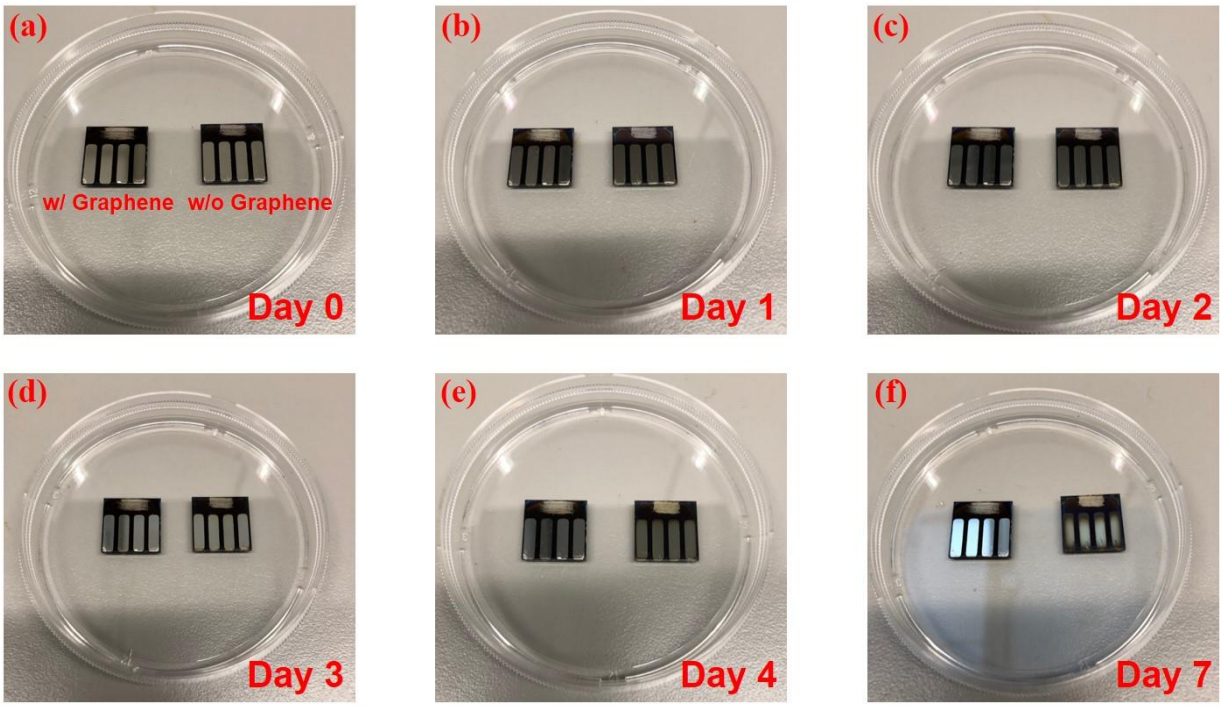

Figure 42. Glass/ITO/CuI/$MAPbI_3$/PCBM/C_{60}-N/Ag full devices with or without a graphene barrier layer during storage in air at 30-50% relative humidity for one week.

The normalized PCE versus time plot for the devices with and without graphene is shown in Figure 43. Noticeably, after one week the complete PSCs without a graphene barrier layer rapidly decreased to 46% of their initial PCE, while those PSCs with a graphene barrier layer maintained 93% of their initial PCE. J-V curves for devices with and without a graphene barrier layer after one week in air at 30-50% relative humidity are given in Figure 44 and 45, respectively. On average after one week in air at 30-50% relative humidity, devices with the graphene barrier layer gave V_{oc} = 1.04 V, J_{sc} = 19.7 mA/cm^2, FF = 75.3%, and PCE = 15.4%; and devices without the graphene barrier layer gave V_{oc} = 1.05 V, J_{sc} = 12.8 mA/cm^2, FF = 52.0%, and PCE = 7.0%. Evidently, the primary cause for the decrease in PCE for devices without graphene was the rapid drop in short circuit current

(J_{sc}) and fill factor (*FF*). This is due to the increasing presence of PbI_2 in the perovskite active layer over time.

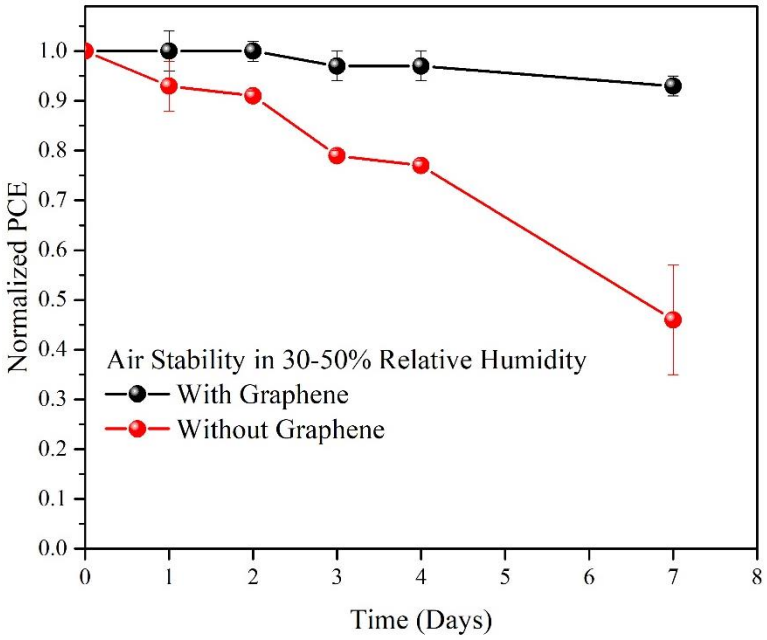

Figure 43. Normalized PCEs of full devices with or without a graphene barrier after storage in air at 30-50% relative humidity for one week.

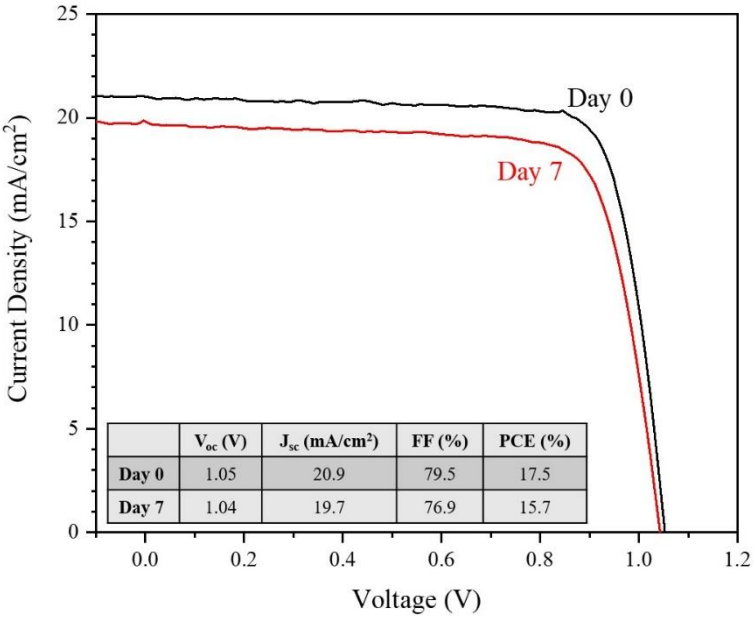

	V_{oc} (V)	J_{sc} (mA/cm^2)	FF (%)	PCE (%)
Day 0	1.05	20.9	79.5	17.5
Day 7	1.04	19.7	76.9	15.7

Figure 44. Forward bias scan J-V curves with corresponding performance parameters (inset) for the highest performing PSC with a graphene barrier layer after 0 days and 7 days in air at 30-50% relative humidity.

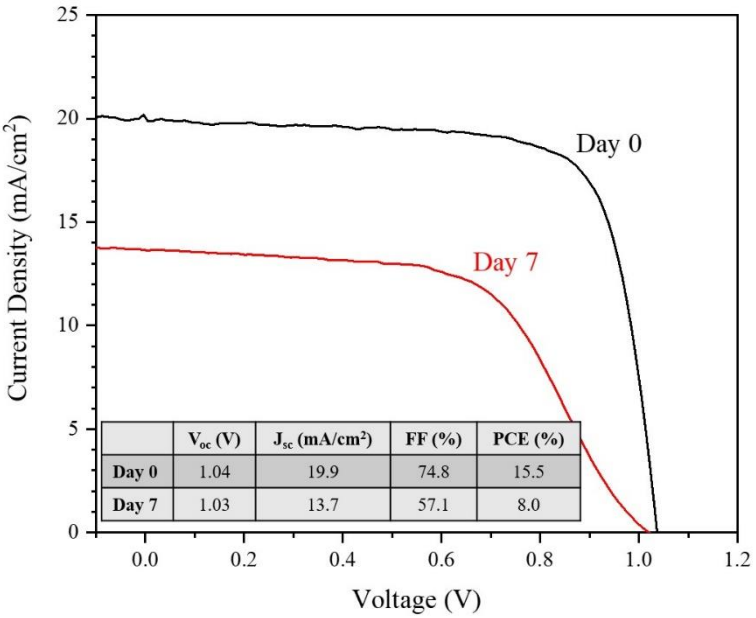

	V_{oc} (V)	J_{sc} (mA/cm^2)	FF (%)	PCE (%)
Day 0	1.04	19.9	74.8	15.5
Day 7	1.03	13.7	57.1	8.0

Figure 45. Forward bias scan J-V curves with corresponding performance parameters (inset) for the highest performing PSC without a graphene barrier layer after 0 days and 7 days in air at 30-50% relative humidity.

On the other hand, devices with graphene withstood degradation to PbI_2 and thus did not show such a decrease in J_{sc} and FF. Ultimately, these results demonstrate that graphene can effectively help to improve the stability of complete PSCs in a humid ambient environment by preventing water penetration into the perovskite active layer. It should be noted, though, that the presence of the hydrophobic PCBM layer in the complete PSCs most likely contributed to improved moisture stability as well.

7.3.2 Thermal Stability

In the presence of high temperatures, it is possible for the metal ions of the top electrode of a complete PSC to migrate into the perovskite active layer. Domanski *et al.* showed that when a complete PSC is heated to 70 °C, Ag or Au ions from the top electrode migrate down through the spiro-OMeTAD HTM and into the perovskite active layer, causing an irreversible degradation.[70] By inserting a thin layer of Cr between the HTM and the electrode, they were able to hinder the metal ion diffusion, albeit with a noticeable loss in overall device performance due to work function mismatch and increased series resistance. It was expected that graphene's impermeability could help to prevent the diffusion of metal ions (Ag in this case) from the top electrode into the perovskite active layer after exposure to heat. The existence of metal ions within the perovskite lattice induces the formation of unwanted charge trap and recombination sites, which ultimately results in a decrease in the overall device performance. To assess this hypothesis, complete PSCs with and without a graphene barrier layer were fabricated, tested for solar cell performance, placed on a hot plate set to 85℃ for 12 hours in the dark, and then removed and retested once cooled to room temperature. A temperature of 85 ℃ was chosen here as this is (1) the IEC 61 656

climatic chamber test temperature standard for thermal stability and (2) below the decomposition temperature for $MAPbI_3$. The devices were not removed from the nitrogen glovebox for the entirety of this procedure to ensure any changes noticed were due solely to the heat treatment. The average device performance parameters for those PSCs with and without a graphene barrier layer before and after the heat treatment are shown in Figures 46a and 46b.

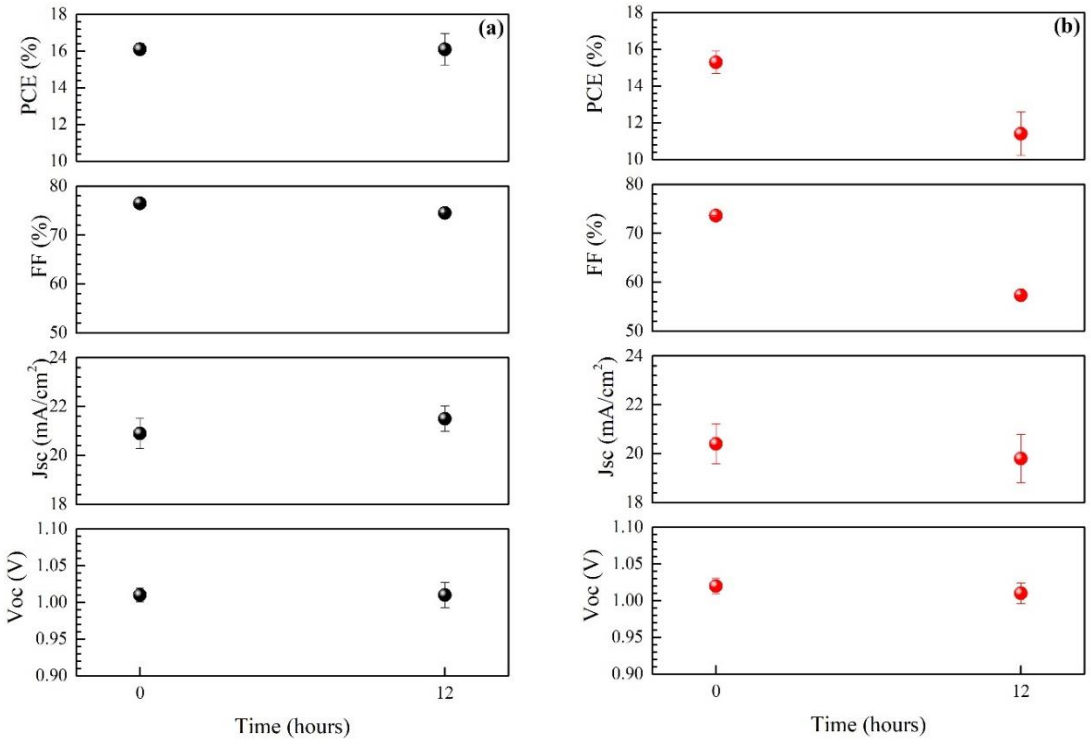

Figure 46. Average device performance metrics for PSCs with (a) and without (b) a graphene barrier layer before and after being subjected to an inert atmosphere heat treatment of 85°C for 12 hours in the dark.

Aside from a slight increase in the average J_{sc} from 20.9 mA/cm^2 to 21.5 mA/cm^2 as well as a slight decrease in the average FF from 76.5% to 74.5%, the average V_{oc} and PCE for the devices with the graphene barrier layer remained constant after the heat treatment (1.01 V and 16.1%, respectively), indicating little to no effect from the heat treatment on the

PSCs with a graphene barrier layer. On the other hand, the average PCE for the PSCs without the graphene barrier layer decreased from 15.3% to 11.4% after the heat treatment, due primarily to a decrease in FF from 73.6% to 57.3%. However, unlike the large decrease in average J_{sc} observed in the moisture stability study, there was only a slight reduction in the average J_{sc} from 20.4 mA/cm^2 to 19.8 mA/cm^2 observed in PSCs without a graphene barrier layer after the heat treatment. One would expect to see a decrease in the average J_{sc} with $MAPbI_3$ degradation to PbI_2 due to the larger band gap of PbI_2; therefore, it is reasonable to suggest that some other factor is causing the decrease in performance for those PSCs without a graphene barrier layer. Additionally, XRD analysis revealed no significant degradation to PbI_2 for either $MAPbI_3$ film with or without the graphene barrier layer (Figure 47).

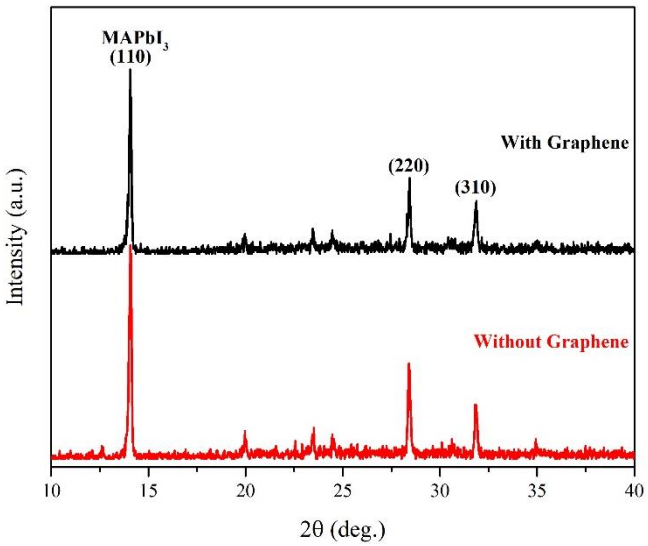

Figure 47. XRD patterns for $MAPbI_3$ films with and without a graphene barrier layer after being subjected to an inert atmosphere heat treatment of 85°C for 12 hours in the dark.

The presence of Ag metal ions in a pure $MAPbI_3$ lattice are defects that create trap states in the absorber material, which lowers the overall achievable FF for the device but may not

necessarily have a large effect on V_{oc} or J_{sc}. As such, it was hypothesized that the cause for the decrease in FF, and thus device performance, for the PSCs without a graphene barrier layer was due to the presence of Ag metal ions in the lattice that had diffused from the top Ag electrode. Inductively coupled plasma mass spectroscopy (ICP-MS) was performed on samples derived from complete PSCs with and without a graphene barrier layer that had been subjected to an inert atmosphere heat treatment of 85°C for 12 hours in the dark. Samples from PSCs with a graphene barrier layer showed an average of 5.8 ± 2.9 ng Ag/mL of solution, whereas samples from PSCs without a graphene barrier layer showed and average of 49.7 ± 14.4 ng Ag/mL of solution. A reference sample derived from a PSC without a graphene barrier layer that was not subjected to the heat treatment showed an Ag content of 0.9 ± 0.2 ng Ag/mL of solution. These results indicate that Ag has certainly diffused from the top electrode into the perovskite active layer for PSCs without a graphene barrier layer and is likely the cause for the observed decrease in performance. The small amount of Ag present in the PSCs with a graphene barrier layer combined with the unchanged average performance for these devices post heat treatment indicate that graphene can successfully prevent the diffusion of Ag metal ions into the perovskite active layer. Of course, that there was any Ag present in the perovskite active layer for PSCs with a graphene barrier layer could suggest the presence of minor defects or tears within the graphene that may have formed during the growth and/or transfer process.

7.4 Conclusions

In conclusion, an orthogonal solvent-assisted pseudo dry transfer method was used to successfully adhere continuous, monolayer graphene to the surface of a $MAPbI_3$ perovskite

film without damaging the underlying perovskite layer. It was found that a single layer of graphene can greatly improve the moisture and thermal stability of $MAPbI_3$ perovskite films. After exposure to 30-50% ambient relative humidity for one week, only minute amounts of PbI_2 were observed in perovskite films with graphene, whereas those films without graphene completely degraded to PbI_2. Completed PSCs with graphene maintained 93% of their initial average PCE after exposure to 30-50% ambient relative humidity for one week, while devices without graphene decreased to 46% of their initial average PCE due to drops in both J_{sc} and FF. After being subjected to an inert atmosphere heat treatment of 85°C for 12 hours in the dark, complete PSCs with graphene showed no decrease in average PCE, whereas those without graphene decreased to about 75% of their initial average PCE due primarily to a drop in FF. ICP-MS data revealed that the $MAPbI_3$ active layer of PSCs without graphene after exposure to heat showed 49.7 ± 14.4 ng Ag/mL of sample solution, while those with graphene showed only 5.8 ± 2.9 ng Ag/mL of solution. These results show that monolayer graphene can be effectively used in PSCs to improve their moisture and thermal stability without significantly compromising their overall performance. Due to graphene's resilience to multiple bending cycles and its roll-to-roll compatibility, an exploration into the use of graphene in flexible and large area PSCs is warranted to further promote its effectiveness in these photovoltaic systems.

CHAPTER 8

FUTURE WORK

8.1 CuI:CuSCN Blends as the HTM in n-i-p PSCs

We have shown that p-i-n PSCs employing a CuI HTM (spin-coated from a 15 mg/mL solution in MeCN onto ITO-coated glass and annealed at 100 °C) yield superior performance compared to those p-i-n PSCs with a PEDOT:PSS, CuSCN, or CuI:CuSCN composite HTM. Additionally, we have shown that p-i-n PSCs with a CuI from MeCN HTM exhibit improved stability over 1032 hours in an inert atmosphere compared to those p-i-n PCSs with a PEDOT:PSS HTM. Economically speaking, a solution-processable inorganic HTM like CuI is preferred over an organic HTM like PEDOT:PSS, especially if it also leads to higher solar cell performance and improved stability when used in complete devices.

The low-cost, high conductivity properties of CuI is what drew Christians and co-workers to use this material in place of the organic spiro-OMeTAD HTM in n-i-p PSCs.[145] The complete devices with a CuI HTM exhibited improved stability and (owing to its higher electrical conductivity) higher FF's compared to those devices with a spiro-OMeTAD HTM. Nevertheless, the n-i-p PSCs with a spiro-OMeTAD HTM still showed higher efficiencies than those with a CuI HTM due to their higher V_{oc}. The CuI-based n-i-p PSCs exhibited significant charge recombination compared to their spiro-OMeTAD-based counterparts, which led to their lower V_{oc} values. Since the CuI was deposited from a mixed di-n-propyl sulfide:chlorobenzene solvent using a syringe pump method (not spin-coating), it is possible that the increased recombination observed in the thicker (~2 μm) CuI-based n-i-p PSCs was due to their poorer film morphology relative to the thinner (~300 nm) spiro-

OMeTAD. Nevertheless, this study did show that CuI was a promising low-cost HTM alternative for n-i-p PSCs and promoted future studies on this topic.

Nearly 4 years later, and again in an effort to find an alternative to the expensive and unstable spiro-OMeTAD, Arora *et al.* investigated the use of CuSCN as an HTM in n-i-p PSCs due to its low-cost, high hole mobility, good thermal stability, and well-aligned work function to that of the perovskite active layer. Due in part to an optimized spin-coating deposition strategy that improved CuSCN film morphology, the performances of n-i-p PSCs employing a CuSCN HTM (19.22% on average) rivaled those employing a spiro-OMeTAD HTM (19.6% on average). Additionally, with the help of a reduced graphene oxide (rGO) spacer between the HTM and the Au electrode, the CuSCN-based PSCs showed improved stability over the spiro-OMeTAD-based PSCs.[171] This study was essential in that it proved that a properly optimized CuSCN inorganic thin film could rival one of the best and most widely-used organic thin films in terms of HTM performance in an n-i-p PSC. It also exposed some of the weaknesses of using Cu-based HTMs in n-i-p PSCs and offered alternatives to circumvent these issues for researchers looking to implement this material in their devices.

Though our work has focused strictly on p-i-n PSCs, we recognize that the results from our study with Cu-based HTMs could help to improve the performance and stability of n-i-p PSCs. Figure 48 is an image of various Cu-based HTMs spin-coated onto the surface of $MAPbI_3$ perovskite films.

Figure 48. Films of $MAPbI_3$/Cu-based HTM after having different Cu-based HTMs deposited onto the perovskite surface.

Unfortunately, it appears as though the best performing Cu-based HTM from our study (CuI from MeCN) cannot be used as an HTM atop the perovskite layer in n-i-p architectures since the MeCN solvent degrades the perovskite active layer. Fortunately, it appears as though the DES solvent does not degrade the underlying perovskite layer during deposition. The study from Arora *et al.* showed that CuSCN is a promising inorganic HTM replacement for organic spiro-OMeTAD in highly efficient n-i-p PSCs[171]; however, our study revealed that while PSCs fabricated using CuSCN from DES HTMs outperformed those PSCs fabricated using CuI from DES HTMs, all PSCs with CuI:CuSCN (3:1, 1:1, and 1:3 v:v) composite HTMs outperformed those with CuSCN HTMs. Therefore, it would be worthwhile to study these CuI:CuSCN composite HTMs in n-i-p PSCs, especially since, at least to our knowledge, there have been no reports of CuI:CuSCN composites being used as the HTM in n-i-p PSCs.

Once film thicknesses and spin-coating conditions for the Cu-based HTMs from DES are optimized for deposition atop $MAPbI_3$ perovskites, complete n-i-p PSCs will be fabricated using CuI:CuSCN (1:0, 3:1, 1:1, 1:3, 0:1 v:v) HTMs as well as a control HTM (e.g. spiro-OMeTAD). The results will be compared, and then, similar to our study for the p-i-n PSCs, various studies on the optical, crystalline/conductive, morphological, and band-level alignment properties will be performed. We suspect that optics will play less of a role in

this architecture since the HTM film is now above the perovskite layer, making efficient light transmittance by the Cu-based film less of an issue and allowing for the fabrication of thicker films if necessary (and possible). With optics being less of a factor, we believe that the 1:3 CuI:CuSCN from DES HTM will lead to the highest performing n-i-p PSC due to its superior crystallinity/charge transport potential properties and well-aligned VB level to that of the perovskite active layer (relative to the other Cu-based HTMs that will be studied). Additionally, films of 1:3 CuI:CuSCN from DES had excellent morphological properties when deposited on a rough ITO surface, with only CuSCN and PEDOT:PSS exhibiting superior film morphologies. To avoid direct contact between the top electrode and the perovskite active layer, we expect that HTM film morphology will play a major role in this architecture. Lastly, due to the unfavorable interactions of CuI and CuSCN with Ag or Au electrodes, we expect that, for stability purposes, it may be necessary to include an interlayer similar to the rGO employed by Arora and co-workers.[171] We suspect that monolayer graphene atop the perovskite or HTM layer could work well here as we have already shown that it can help improve the thermal stability of PSCs due to its impermeable properties.

8.2 The Effect of Graphene Overlayers on the Light Stability of PSCs

We have shown that monolayer graphene can be successfully incorporated into a complete PSC atop the perovskite film without damaging the underlying perovskite active layer. The presence of the impermeable graphene within the device helps to thwart moisture-induced perovskite degradation as well as heat-induced metal ion diffusion from the top electrode to the perovskite active layer. Since charges can easily tunnel through the single-atom-thick graphene film, the graphene can improve the moisture and thermal stability without

hindering the charge transport, and, thus, the overall performance of the PSC. Because of graphene's high molecular impermeability, we postulate that it could also help to improve the light stability of complete PSC's.

Photoinduced ion migration within the perovskite active layer has been linked to device degradation and current-voltage hysteresis during device operation. For $MAPbI_3$, the ions I^-, MA^+, and Pb^{2+} are the possible mobile species, with I^- and MA^+ being the most likely candidates for ion migration owing to their fast time scales associated with ion mobility. Bag *et al.* used electrochemical impedance spectroscopy (EIS) to study photoinduced ion migration within PSC's.[108] In the dark under applied bias, they observed only electronic charge transport within the perovskite device; that is, only a single semi-circle in the high-frequency region of the Nyquist plot. However, under illumination and applied bias, the Nyquist plots from EIS gave rise to a Warburg diffusion component in the low frequency region typically associated with ion diffusion. Because iodide ion mobility is on the time scale of less than 1 μs, it was concluded that evidence of iodide ion transport would be masked by the semi-circle of the high frequency region. Therefore, the mobile ion identified by the Warburg branch of the Nyquist plots was likely MA^+. Owing once again to its molecular impermeability, graphene could be a promising candidate to prevent ion diffusion originating from the perovskite active layer. By placing monolayer graphene above, below, or both above and below the perovskite active layer of a complete PSC, we can use EIS to observe any possible ion diffusion. It is expected that the graphene encapsulation of the perovskite active layer will prevent the diffusion of the MA^+ ion, which will translate to no observable Warburg component in the resulting Nyquist plots.

It is not known to what degree ion mobility is necessary within PSC's for optimum performance, so while the graphene may prevent intrinsic ion diffusion, it will be interesting to see the effect its presence has on the overall device performance. Since CuI from MeCN will likely be used as the HTM in these complete devices due to its ability to be successfully deposited on graphene (Figure 49), light-stability measurements (using both EIS and J-V measurements) of PSCs with CuI from MeCN HTMs should first be performed as a control.

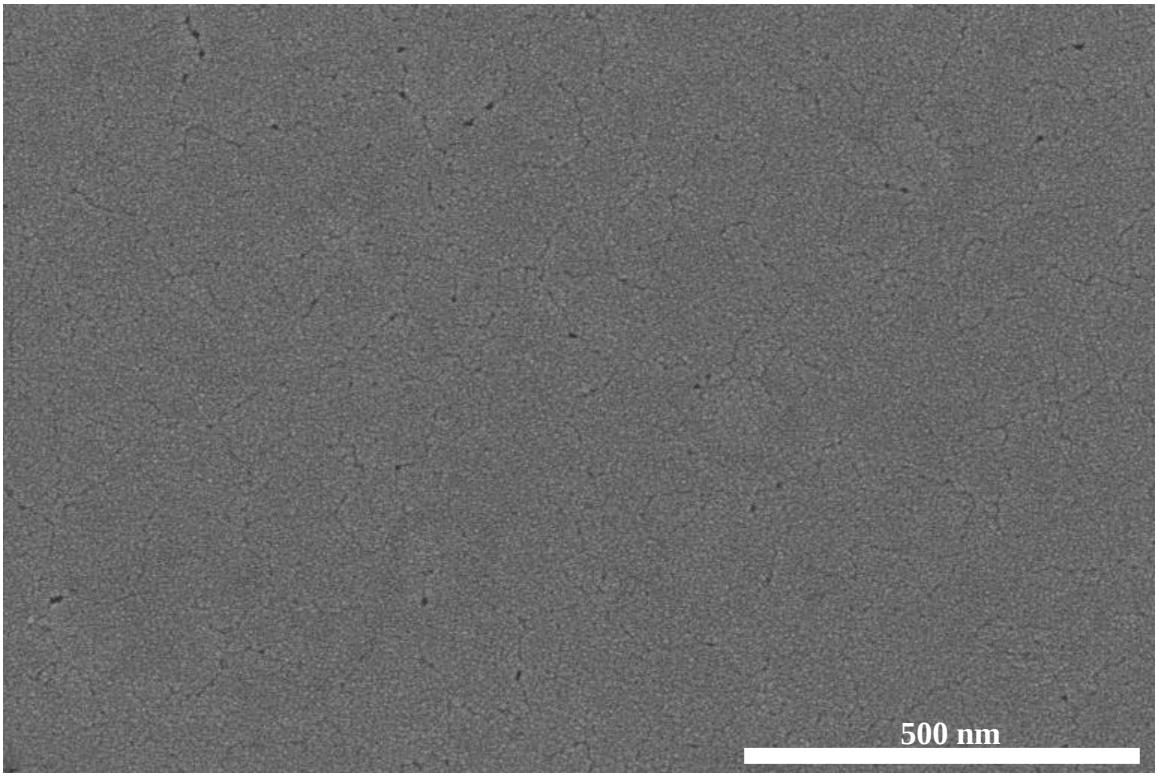

Figure 49. SEM image of CuI deposited atop a graphene surface. The CuI (15 mg/mL in MeCN) was spin-coated onto the graphene at 3000 rpm for 60 sec and annealed at 100 °C for 10 mins. Note the improved surface morphology of CuI films on smooth graphene compared to that of CuI films on rough ITO (Figure 22a).

Due to the presence of mobile iodine in CuI films, it is expected that there will be at least some light-induced instability within the control. If the light instability is too severe with PSCs employing CuI HTMs, however, then it may be necessary to switch to a more light-

stable HTM (one that can still be successfully deposited on graphene) for the benefit of future tests. Once a suitable HTM has been identified and the aforementioned EIS measurements have been performed on the control and graphene-containing complete PSCs, then performance measurements will be done on the control and graphene-containing PSCs to gain further insight onto the effect of suppressed ion diffusion on the performance of PSCs. Of course, additional device characterization techniques should be performed should questions continue to remain after the EIS and performance tests have been completed.

BIBLIOGRAPHY

(1) US Department of Commerce, N. E. S. R. L. ESRL Global Monitoring Division - Global Greenhouse Gas Reference Network.

(2) Why we go solar - Solaflect Energy: Tracker Mounted Solar Panels http://www.solaflect.com/why-we-go-solar-5/ (accessed Sep 26, 2019).

(3) EIA projects 28% increase in world energy use by 2040 - Today in Energy - U.S. Energy Information Administration (EIA) https://www.eia.gov/todayinenergy/detail.php?id=32912 (accessed Sep 26, 2019).

(4) History of Solar Power - IER https://www.instituteforenergyresearch.org/renewable/solar/history-of-solar-power/#_ftn6 (accessed Sep 26, 2019).

(5) Best Research-Cell Efficiency Chart | Photovoltaic Research | NREL https://www.nrel.gov/pv/cell-efficiency.html (accessed Sep 26, 2019).

(6) Shockley, W.; Queisser, H. J. Detailed Balance Limit of Efficiency of P-n Junction Solar Cells. *Journal of Applied Physics* **1961**, *32* (3), 510–519. https://doi.org/10.1063/1.1736034.

(7) Polman, A.; Knight, M.; Garnett, E. C.; Ehrler, B.; Sinke, W. C. Photovoltaic Materials: Present Efficiencies and Future Challenges. *Science*. American Association for the Advancement of Science April 15, 2016. https://doi.org/10.1126/science.aad4424.

(8) Green, M. A. *Third Generation Photovoltaics : Advanced Solar Energy Conversion*; Springer, 2006.

(9) Wenk. *Minerals: Their Constitution and Origin-Minerals: Their Constitution and Origin Hans-Rudolf Wenk and Andrei Bulakh Frontmatter More Information*; 1996.

(10) Green, M. A.; Ho-Baillie, A.; Snaith, H. J. The Emergence of Perovskite Solar Cells. *Nature Photonics* **2014**, *8* (7), 506–514. https://doi.org/10.1038/nphoton.2014.134.

(11) Goldschmidt, V. M. Die Gesetze Der Krystallochemie. *Die Naturwissenschaften* **1926**, *14* (21), 477–485. https://doi.org/10.1007/BF01507527.

(12) Kronmuller, H.; Parkin, S. *Handbook of Magnetism and Advanced Magnetic Materials. Volume 3: Novel Techniques for Characterizing and Preparing Samples*; Kronmuller, H., Parkin, S., Eds.; John Wiley & Sons, Ltd., 2007.

(13) Etgar, L. The Merit of Perovskite's Dimensionality; Can This Replace the 3D Halide Perovskite? *Energy and Environmental Science* **2018**, *11* (2), 234–242. https://doi.org/10.1039/c7ee03397d.

(14) Mitzi, D. B.; Wang, S.; Feild, C. A.; Chess, C. A.; Guloy, A. M. Conducting Layered Organic-Inorganic Halides Containing 〈110〉 -Oriented Perovskite Sheets. *Science* **1995**, *267* (5203), 1473–1476. https://doi.org/10.1126/science.267.5203.1473.

(15) Mitzi, D. B. Synthesis , Crystal Structure , and Optical and Thermal Properties of (C 4 H 9 NH 3) 2 MI 4 (M) Ge , Sn , Pb). **1996**, No. 4, 791–800.

(16) Kagan, C. R.; Mitzi, D. B.; Dimitrakopoulos, C. D. Organic-Inorganic Hybrid Materials as Semiconducting Channels in Thin- Film Field-Effect Transistors. *Science* **1999**, *286* (5441), 945–947. https://doi.org/10.1126/science.286.5441.945.

(17) Mitzi, D. B.; Liang, K. Preparation and Properties of (C4H9NH3)2EuI4: A Luminescent Organic-Inorganic Perovskite with a Divalent Rare-Earth Metal Halide Framework. *Chemistry of Materials* **1997**, *9* (12), 2990–2995.

(18) Snaith, H. J. Perovskites: The Emergence of a New Era for Low-Cost, High-Efficiency Solar Cells. *Journal of Physical Chemistry Letters* **2013**, *4* (21), 3623–3630. https://doi.org/10.1021/jz4020162.

(19) Liang, K.; Mitzi, D. B.; Prikas, M. T. Synthesis and Characterization of Organic-Inorganic Perovskite Thin Films Prepared Using a Versatile Two-Step Dipping Technique. *Chemistry of Materials* **1998**, *10* (1), 403–411. https://doi.org/10.1021/cm970568f.

(20) Kojima, A.; Teshima, K.; Shirai, Y.; Miyasaka, T. Organometal Halide Perovskites as Visible-Light Sensitizers for Photovoltaic Cells. *Journal of the American Chemical Society* **2009**, *131* (17), 6050–6051. https://doi.org/10.1021/ja809598r.

(21) Im, J. H.; Lee, C. R.; Lee, J. W.; Park, S. W.; Park, N. G. 6.5% Efficient Perovskite Quantum-Dot-Sensitized Solar Cell. *Nanoscale* **2011**, *3* (10), 4088–4093. https://doi.org/10.1039/c1nr10867k.

(22) Chung, I.; Lee, B.; He, J.; Chang, R. P. H.; Kanatzidis, M. G. All-Solid-State Dye-Sensitized Solar Cells with High Efficiency. *Nature* **2012**, *485* (7399), 486–489. https://doi.org/10.1038/nature11067.

(23) Lee, M. M.; Teuscher, J.; Miyasaka, T.; Murakami, T. N.; Snaith, H. J. Efficient Hybrid Solar Cells Based on Meso-Superstructured Organometal Halide Perovskites. *Science* **2012**, *338* (6107), 643–647. https://doi.org/10.1126/science.1228604.

(24) Liang, W. Y. Excitons. *Physics Education* **1970**, *5* (4), 003. https://doi.org/10.1088/0031-9120/5/4/003.

(25) Huang, J.; Yuan, Y.; Shao, Y.; Yan, Y. Understanding the Physical Properties of Hybrid Perovskites for Photovoltaic Applications. *Nature Reviews Materials*. Nature Publishing Group July 4, 2017. https://doi.org/10.1038/natrevmats.2017.42.

(26) Absorption Coefficient | PVEducation https://www.pveducation.org/pvcdrom/pn-junctions/absorption-coefficient (accessed Sep 29, 2019).

(27) Park, N. G. Perovskite Solar Cells: An Emerging Photovoltaic Technology. *Materials Today* **2015**, *18* (2), 65–72. https://doi.org/10.1016/j.mattod.2014.07.007.

(28) Noh, J. H.; Im, S. H.; Heo, J. H.; Mandal, T. N.; Seok, S. il. Chemical Management for Colorful, Efficient, and Stable Inorganic-Organic Hybrid Nanostructured Solar Cells. *Nano Letters* **2013**, *13* (4), 1764–1769. https://doi.org/10.1021/nl400349b.

(29) Kanhere, P.; Chakraborty, S.; Rupp, C. J.; Ahuja, R.; Chen, Z. Substitution Induced Band Structure Shape Tuning in Hybrid Perovskites (CH 3 NH 3 Pb 1-x Sn x I 3) for Efficient Solar Cell Applications. *RSC Advances* **2015**, *5* (130), 107497–107502. https://doi.org/10.1039/c5ra19778c.

(30) Jung, H. S.; Park, N. G. Perovskite Solar Cells: From Materials to Devices. *Small*. Wiley-VCH Verlag January 7, 2015, pp 10–25. https://doi.org/10.1002/smll.201402767.

(31) Eperon, G. E.; Stranks, S. D.; Menelaou, C.; Johnston, M. B.; Herz, L. M.; Snaith, H. J. Formamidinium Lead Trihalide: A Broadly Tunable Perovskite for Efficient Planar Heterojunction Solar Cells. *Energy and Environmental Science* **2014**, *7* (3), 982–988. https://doi.org/10.1039/c3ee43822h.

(32) Ball, J. M.; Lee, M. M.; Hey, A.; Snaith, H. J. Low-Temperature Processed Meso-Superstructured to Thin-Film Perovskite Solar Cells. *Energy and Environmental Science* **2013**, *6* (6), 1739–1743. https://doi.org/10.1039/c3ee40810h.

(33) Etgar, L.; Gao, P.; Xue, Z.; Peng, Q.; Chandiran, A. K.; Liu, B.; Nazeeruddin, M. K.; Grätzel, M. Mesoscopic CH 3NH 3PbI 3/TiO 2 Heterojunction Solar Cells. *Journal of the American Chemical Society* **2012**, *134* (42), 17396–17399. https://doi.org/10.1021/ja307789s.

(34) Xing, G.; Mathews, N.; Sun, S.; Lim, S. S.; Lam, Y. M.; Graẗzel, M.; Mhaisalkar, S.; Sum, T. C. Long-Range Balanced Electron-and Hole-Transport Lengths in Organic-Inorganic CH3NH3PbI3. *Science* **2013**, *342* (6156), 344–347. https://doi.org/10.1126/science.1243167.

(35) Stranks, S. D.; Eperon, G. E.; Grancini, G.; Menelaou, C.; Alcocer, M. J. P.; Leijtens, T.; Herz, L. M.; Petrozza, A.; Snaith, H. J. Electron-Hole Diffusion Lengths Exceeding 1 Micrometer in an Organometal Trihalide Perovskite Absorber. *Science* **2013**, *342* (6156), 341–344. https://doi.org/10.1126/science.1243982.

(36) Fan, Z.; Sun, K.; Wang, J. Perovskites for Photovoltaics: A Combined Review of Organic-Inorganic Halide Perovskites and Ferroelectric Oxide Perovskites. *Journal of Materials Chemistry A* **2015**, *3* (37), 18809–18828. https://doi.org/10.1039/c5ta04235f.

(37) Ansari, M. I. H.; Qurashi, A.; Nazeeruddin, M. K. Frontiers, Opportunities, and Challenges in Perovskite Solar Cells: A Critical Review. *Journal of Photochemistry and Photobiology C: Photochemistry Reviews*. Elsevier B.V. June 1, 2018, pp 1–24. https://doi.org/10.1016/j.jphotochemrev.2017.11.002.

(38) Zuo, C.; Bolink, H. J.; Han, H.; Huang, J.; Cahen, D.; Ding, L.; Zuo, C.; Ding, L.; Cahen, D.; Bolink, H. J.; et al. Advances in Perovskite Solar Cells. **2016**. https://doi.org/10.1002/advs.201500324.

(39) Park, N. G.; Grätzel, M.; Miyasaka, T.; Zhu, K.; Emery, K. Towards Stable and Commercially Available Perovskite Solar Cells. *Nature Energy*. Nature Publishing Group September 19, 2016. https://doi.org/10.1038/nenergy.2016.152.

(40) Zhou, H.; Chen, Q.; Li, G.; Luo, S.; Song, T. B.; Duan, H. S.; Hong, Z.; You, J.; Liu, Y.; Yang, Y. Interface Engineering of Highly Efficient Perovskite Solar Cells. *Science* **2014**, *345* (6196), 542–546. https://doi.org/10.1126/science.1254050.

(41) Momblona, C.; Gil-Escrig, L.; Bandiello, E.; Hutter, E. M.; Sessolo, M.; Lederer, K.; Blochwitz-Nimoth, J.; Bolink, H. J. Efficient Vacuum Deposited P-i-n and n-i-p Perovskite Solar Cells Employing Doped Charge Transport Layers. *Energy and Environmental Science* **2016**, *9* (11), 3456–3463. https://doi.org/10.1039/c6ee02100j.

(42) Jeng, J. Y.; Chiang, Y. F.; Lee, M. H.; Peng, S. R.; Guo, T. F.; Chen, P.; Wen, T. C. CH3NH3PbI3 Perovskite/Fullerene Planar-Heterojunction Hybrid Solar Cells. *Advanced Materials* **2013**, *25* (27), 3727–3732. https://doi.org/10.1002/adma.201301327.

(43) Lee, H.; Stephenson, J. C.; Richter, L. J.; McNeill, C. R.; Gann, E.; Thomsen, L.; Park, S.; Jeong, J.; Yi, Y.; DeLongchamp, D. M.; et al. The Structural Origin of Electron Injection Enhancements with Fulleropyrrolidine Interlayers. *Advanced Materials Interfaces* **2016**, *3* (10). https://doi.org/10.1002/admi.201500852.

(44) Wang, K. C.; Jeng, J. Y.; Shen, P. S.; Chang, Y. C.; Diau, E. W. G.; Tsai, C. H.; Chao, T. Y.; Hsu, H. C.; Lin, P. Y.; Chen, P.; et al. P-Type Mesoscopic Nickel

Oxide/Organometallic Perovskite Heterojunction Solar Cells. *Scientific Reports* **2014**, *4*. https://doi.org/10.1038/srep04756.

(45) Zheng, X.; Chen, B.; Dai, J.; Fang, Y.; Bai, Y.; Lin, Y.; Wei, H.; Zeng, X. C.; Huang, J. Defect Passivation in Hybrid Perovskite Solar Cells Using Quaternary Ammonium Halide Anions and Cations. *Nature Energy* **2017**, *2* (7), 1–17. https://doi.org/10.1038/nenergy.2017.102.

(46) Tavakoli, M. M.; Dastjerdi, H. T.; Prochowicz, D.; Yadav, P.; Tavakoli, R.; Saliba, M.; Fan, Z. Highly Efficient and Stable Inverted Perovskite Solar Cells Using Down-Shifting Quantum Dots as a Light Management Layer and Moisture-Assisted Film Growth. *Journal of Materials Chemistry A* **2019**, *7* (24), 14753–14760. https://doi.org/10.1039/c9ta03131f.

(47) Edri, E.; Kirmayer, S.; Henning, A.; Mukhopadhyay, S.; Gartsman, K.; Rosenwaks, Y.; Hodes, G.; Cahen, D. Why Lead Methylammonium Tri-Iodide Perovskite-Based Solar Cells Require a Mesoporous Electron Transporting Scaffold (but Not Necessarily a Hole Conductor). *Nano Letters* **2014**, *14* (2), 1000–1004. https://doi.org/10.1021/nl404454h.

(48) Liu, D.; Yang, J.; Kelly, T. L. Compact Layer Free Perovskite Solar Cells with 13.5% Efficiency. *Journal of the American Chemical Society* **2014**, *136* (49), 17116–17122. https://doi.org/10.1021/ja508758k.

(49) Amherst ScholarWorks, Um.; Amherst Doctoral Dissertations Dissertations, Um.; Han, X. *Theoretical Studies of Atomic Transport in Ternary Theoretical Studies of Atomic Transport in Ternary Semiconductor Quantum Dots and Charge Transport in Organic Semiconductor Quantum Dots and Charge Transport in Organic Photovoltaic Active Layers Photovoltaic Active Layers*; 2016.

(50) Zhou, Y.; Gray-Weale, A. A Numerical Model for Charge Transport and Energy Conversion of Perovskite Solar Cells. *Physical Chemistry Chemical Physics* **2016**, *18* (6), 4476–4486. https://doi.org/10.1039/c5cp05371d.

(51) Herz, L. M. Charge-Carrier Dynamics in Organic-Inorganic Metal Halide Perovskites. *Annual Review of Physical Chemistry* **2016**, *67* (1), 65–89. https://doi.org/10.1146/annurev-physchem-040215-112222.

(52) Marinova, N.; Valero, S.; Delgado, J. L. Organic and Perovskite Solar Cells: Working Principles, Materials and Interfaces. *Journal of Colloid and Interface Science*. Academic Press Inc. February 15, 2017, pp 373–389. https://doi.org/10.1016/j.jcis.2016.11.021.

(53) Ihly, R.; Dowgiallo, A. M.; Yang, M.; Schulz, P.; Stanton, N. J.; Reid, O. G.; Ferguson, A. J.; Zhu, K.; Berry, J. J.; Blackburn, J. L. Efficient Charge Extraction and Slow Recombination in Organic-Inorganic Perovskites Capped with

Semiconducting Single-Walled Carbon Nanotubes. *Energy and Environmental Science* **2016**, *9* (4), 1439–1449. https://doi.org/10.1039/c5ee03806e.

(54) Philippe, B.; Park, B. W.; Lindblad, R.; Oscarsson, J.; Ahmadi, S.; Johansson, E. M. J.; Rensmo, H. Chemical and Electronic Structure Characterization of Lead Halide Perovskites and Stability Behavior under Different Exposures-A Photoelectron Spectroscopy Investigation. *Chemistry of Materials* **2015**, *27* (5), 1720–1731. https://doi.org/10.1021/acs.chemmater.5b00348.

(55) Supasai, T.; Rujisamphan, N.; Ullrich, K.; Chemseddine, A.; Dittrich, T. Formation of a Passivating CH 3 NH 3 PbI 3 /PbI 2 Interface during Moderate Heating of CH 3 NH 3 PbI 3 Layers. *Applied Physics Letters* **2013**, *103* (18). https://doi.org/10.1063/1.4826116.

(56) Qin, C.; Matsushima, T.; Fujihara, T.; Potscavage, W. J.; Adachi, C. Degradation Mechanisms of Solution-Processed Planar Perovskite Solar Cells: Thermally Stimulated Current Measurement for Analysis of Carrier Traps. *Advanced Materials* **2016**, *28* (3), 466–471. https://doi.org/10.1002/adma.201502610.

(57) Leijtens, T.; Eperon, G. E.; Pathak, S.; Abate, A.; Lee, M. M.; Snaith, H. J. Overcoming Ultraviolet Light Instability of Sensitized TiO2 with Meso-Superstructured Organometal Tri-Halide Perovskite Solar Cells. *Nature Communications* **2013**, *4*. https://doi.org/10.1038/ncomms3885.

(58) Aristidou, N.; Sanchez-Molina, I.; Chotchuangchutchaval, T.; Brown, M.; Martinez, L.; Rath, T.; Haque, S. A. The Role of Oxygen in the Degradation of Methylammonium Lead Trihalide Perovskite Photoactive Layers. *Angewandte Chemie - International Edition* **2015**, *54* (28), 8208–8212. https://doi.org/10.1002/anie.201503153.

(59) Bag, M.; Renna, L. A.; Adhikari, R. Y.; Karak, S.; Liu, F.; Lahti, P. M.; Russell, T. P.; Tuominen, M. T.; Venkataraman, D. Kinetics of Ion Transport in Perovskite Active Layers and Its Implications for Active Layer Stability. *Journal of the American Chemical Society* **2015**, *137* (40), 13130–13137. https://doi.org/10.1021/jacs.5b08535.

(60) Smith, E. C.; Ellis, C. L. C.; Javaid, H.; Renna, L. A.; Liu, Y.; Russell, T. P.; Bag, M.; Venkataraman, D. Interplay between Ion Transport, Applied Bias, and Degradation under Illumination in Hybrid Perovskite p-i-n Devices. *Journal of Physical Chemistry C* **2018**, *122* (25), 13986–13994. https://doi.org/10.1021/acs.jpcc.8b01121.

(61) Frost, J. M.; Butler, K. T.; Brivio, F.; Hendon, C. H.; van Schilfgaarde, M.; Walsh, A. Atomistic Origins of High-Performance in Hybrid Halide Perovskite Solar Cells. *Nano Letters* **2014**, *14* (5), 2584–2590. https://doi.org/10.1021/nl500390f.

(62) Manser, J. S.; Saidaminov, M. I.; Christians, J. A.; Bakr, O. M.; Kamat, P. v. Making and Breaking of Lead Halide Perovskites. *Accounts of Chemical Research* **2016**, *49* (2), 330–338. https://doi.org/10.1021/acs.accounts.5b00455.

(63) Christians, J. A.; Miranda Herrera, P. A.; Kamat, P. v. Transformation of the Excited State and Photovoltaic Efficiency of CH3NH3PbI3 Perovskite upon Controlled Exposure to Humidified Air. *Journal of the American Chemical Society* **2015**, *137* (4), 1530–1538. https://doi.org/10.1021/ja511132a.

(64) Wang, D.; Wright, M.; Elumalai, N. K.; Uddin, A. Stability of Perovskite Solar Cells. *Solar Energy Materials and Solar Cells*. Elsevier April 1, 2016, pp 255–275. https://doi.org/10.1016/j.solmat.2015.12.025.

(65) Wang, R.; Mujahid, M.; Duan, Y.; Wang, Z. K.; Xue, J.; Yang, Y. A Review of Perovskites Solar Cell Stability. *Advanced Functional Materials*. Wiley-VCH Verlag 2019. https://doi.org/10.1002/adfm.201808843.

(66) Mosconi, E.; de Angelis, F. Mobile Ions in Organohalide Perovskites: Interplay of Electronic Structure and Dynamics. *ACS Energy Letters*. American Chemical Society July 8, 2016, pp 182–188. https://doi.org/10.1021/acsenergylett.6b00108.

(67) Kato, Y.; Ono, L. K.; Lee, M. v.; Wang, S.; Raga, S. R.; Qi, Y. Silver Iodide Formation in Methyl Ammonium Lead Iodide Perovskite Solar Cells with Silver Top Electrodes. *Advanced Materials Interfaces* **2015**, *2* (13). https://doi.org/10.1002/admi.201500195.

(68) Chen, B.; Yang, M.; Priya, S.; Zhu, K. Origin of J-V Hysteresis in Perovskite Solar Cells. *Journal of Physical Chemistry Letters*. American Chemical Society March 3, 2016, pp 905–917. https://doi.org/10.1021/acs.jpclett.6b00215.

(69) Zhang, T.; Meng, X.; Bai, Y.; Xiao, S.; Hu, C.; Yang, Y.; Chen, H.; Yang, S. Profiling the Organic Cation-Dependent Degradation of Organolead Halide Perovskite Solar Cells. *Journal of Materials Chemistry A* **2017**, *5* (3), 1103–1111. https://doi.org/10.1039/C6TA09687E.

(70) Domanski, K.; Correa-Baena, J. P.; Mine, N.; Nazeeruddin, M. K.; Abate, A.; Saliba, M.; Tress, W.; Hagfeldt, A.; Grätzel, M. Not All That Glitters Is Gold: Metal-Migration-Induced Degradation in Perovskite Solar Cells. *ACS Nano* **2016**, *10* (6), 6306–6314. https://doi.org/10.1021/acsnano.6b02613.

(71) Jeon, N. J.; Noh, J. H.; Yang, W. S.; Kim, Y. C.; Ryu, S.; Seo, J.; Seok, S. il. Compositional Engineering of Perovskite Materials for High-Performance Solar Cells. *Nature* **2015**, *517* (7535), 476–480. https://doi.org/10.1038/nature14133.

(72) Lee, J. W.; Kim, D. H.; Kim, H. S.; Seo, S. W.; Cho, S. M.; Park, N. G. Formamidinium and Cesium Hybridization for Photo- and Moisture-Stable Perovskite Solar Cell. *Advanced Energy Materials* **2015**, *5* (20). https://doi.org/10.1002/aenm.201501310.

(73) Saliba, M.; Matsui, T.; Seo, J. Y.; Domanski, K.; Correa-Baena, J. P.; Nazeeruddin, M. K.; Zakeeruddin, S. M.; Tress, W.; Abate, A.; Hagfeldt, A.; et al. Cesium-Containing Triple Cation Perovskite Solar Cells: Improved Stability, Reproducibility and High Efficiency. *Energy and Environmental Science* **2016**, *9* (6), 1989–1997. https://doi.org/10.1039/c5ee03874j.

(74) Cao, D. H.; Stoumpos, C. C.; Farha, O. K.; Hupp, J. T.; Kanatzidis, M. G. 2D Homologous Perovskites as Light-Absorbing Materials for Solar Cell Applications. *Journal of the American Chemical Society* **2015**, *137* (24), 7843–7850. https://doi.org/10.1021/jacs.5b03796.

(75) Grancini, G.; Roldán-Carmona, C.; Zimmermann, I.; Mosconi, E.; Lee, X.; Martineau, D.; Narbey, S.; Oswald, F.; de Angelis, F.; Graetzel, M.; et al. One-Year Stable Perovskite Solar Cells by 2D/3D Interface Engineering. *Nature Communications* **2017**, *8*. https://doi.org/10.1038/ncomms15684.

(76) Habisreutinger, S. N.; Leijtens, T.; Eperon, G. E.; Stranks, S. D.; Nicholas, R. J.; Snaith, H. J. Carbon Nanotube/Polymer Composites as a Highly Stable Hole Collection Layer in Perovskite Solar Cells. *Nano Letters* **2014**, *14* (10), 5561–5568. https://doi.org/10.1021/nl501982b.

(77) Wang, Q.; Dong, Q.; Li, T.; Gruverman, A.; Huang, J. Thin Insulating Tunneling Contacts for Efficient and Water-Resistant Perovskite Solar Cells. *Advanced Materials* **2016**, 6734–6739. https://doi.org/10.1002/adma.201600969.

(78) Zheng, X.; Chen, B.; Dai, J.; Fang, Y.; Bai, Y.; Lin, Y.; Wei, H.; Zeng, X. C.; Huang, J. Defect Passivation in Hybrid Perovskite Solar Cells Using Quaternary Ammonium Halide Anions and Cations. *Nature Energy* **2017**, *2* (7). https://doi.org/10.1038/nenergy.2017.102.

(79) Niu, T.; Lu, J.; Munir, R.; Li, J.; Barrit, D.; Zhang, X.; Hu, H.; Yang, Z.; Amassian, A.; Zhao, K.; et al. Stable High-Performance Perovskite Solar Cells via Grain Boundary Passivation. *Advanced Materials* **2018**, *30* (16). https://doi.org/10.1002/adma.201706576.

(80) Hoefler, S. F.; Trimmel, G.; Rath, T. Progress on Lead-Free Metal Halide Perovskites for Photovoltaic Applications: A Review. *Monatshefte fur Chemie*. Springer-Verlag Wien May 1, 2017, pp 795–826. https://doi.org/10.1007/s00706-017-1933-9.

(81) 2019 RoHS Compliance Guide: Regulations, 10 Substances, Exemptions https://www.rohsguide.com/ (accessed Sep 29, 2019).

(82) Bae, S. Y.; Lee, S. Y.; Kim, J. wan; Umh, H. N.; Jeong, J.; Bae, S.; Yi, J.; Kim, Y.; Choi, J. Hazard Potential of Perovskite Solar Cell Technology for Potential Implementation of "Safe-by-Design" Approach. *Scientific Reports* **2019**, *9* (1). https://doi.org/10.1038/s41598-018-37229-8.

(83) Petrus, M. L.; Schlipf, J.; Li, C.; Gujar, T. P.; Giesbrecht, N.; Müller-Buschbaum, P.; Thelakkat, M.; Bein, T.; Hüttner, S.; Docampo, P. Capturing the Sun: A Review of the Challenges and Perspectives of Perovskite Solar Cells. *Advanced Energy Materials*. Wiley-VCH Verlag August 23, 2017. https://doi.org/10.1002/aenm.201700264.

(84) Shi, Z.; Jayatissa, A. H. Perovskites-Based Solar Cells: A Review of Recent Progress, Materials and Processing Methods. *Materials*. MDPI AG May 4, 2018. https://doi.org/10.3390/ma11050729.

(85) Nie, W.; Tsai, H.; Asadpour, R.; Neukirch, A. J.; Gupta, G.; Crochet, J. J.; Chhowalla, M.; Tretiak, S.; Alam, M. A.; Wang, H. High-Efficiency Solution-Processed Perovskite Solar Cells with Millimeter-Scale Grains. **2015**, *347* (6221), 522–526.

(86) Song, T. bin; Chen, Q.; Zhou, H.; Jiang, C.; Wang, H. H.; Yang, Y. M.; Liu, Y.; You, J.; Yang, Y. Perovskite Solar Cells: Film Formation and Properties. *Journal of Materials Chemistry A* **2015**, *3* (17), 9032–9050. https://doi.org/10.1039/c4ta05246c.

(87) Ahn, N.; Son, D. Y.; Jang, I. H.; Kang, S. M.; Choi, M.; Park, N. G. Highly Reproducible Perovskite Solar Cells with Average Efficiency of 18.3% and Best Efficiency of 19.7% Fabricated via Lewis Base Adduct of Lead(II) Iodide. *Journal of the American Chemical Society* **2015**, *137* (27), 8696–8699. https://doi.org/10.1021/jacs.5b04930.

(88) Kim, H.-S.; Lee, C.-R.; Im, J.-H.; Lee, K.-B.; Moehl, T.; Marchioro, A.; Moon, S.-J.; Humphry-Baker, R.; Yum, J.-H.; Moser, J. E.; et al. Lead Iodide Perovskite Sensitized All-Solid-State Submicron Thin Film Mesoscopic Solar Cell with Efficiency Exceeding 9%. *Scientific reports* **2012**, *2*, 591. https://doi.org/10.1038/srep00591.

(89) Im, J. H.; Jang, I. H.; Pellet, N.; Grätzel, M.; Park, N. G. Growth of CH3 NH3 PbI3 Cuboids with Controlled Size for High-Efficiency Perovskite Solar Cells. *Nature Nanotechnology* **2014**, *9* (11), 927–932. https://doi.org/10.1038/nnano.2014.181.

(90) Burschka, J.; Pellet, N.; Moon, S. J.; Humphry-Baker, R.; Gao, P.; Nazeeruddin, M. K.; Grätzel, M. Sequential Deposition as a Route to High-Performance Perovskite-Sensitized Solar Cells. *Nature* **2013**, *499* (7458), 316–319. https://doi.org/10.1038/nature12340.

(91) Chen, Q.; Zhou, H.; Hong, Z.; Luo, S.; Duan, H. S.; Wang, H. H.; Liu, Y.; Li, G.; Yang, Y. Planar Heterojunction Perovskite Solar Cells via Vapor-Assisted Solution Process. *Journal of the American Chemical Society* **2014**, *136* (2), 622–625. https://doi.org/10.1021/ja411509g.

(92) Liu, M.; Johnston, M. B.; Snaith, H. J. Efficient Planar Heterojunction Perovskite Solar Cells by Vapour Deposition. *Nature* **2013**, *501* (7467), 395–398. https://doi.org/10.1038/nature12509.

(93) Xiao, M.; Huang, F.; Huang, W.; Dkhissi, Y.; Zhu, Y.; Etheridge, J.; Gray-Weale, A.; Bach, U.; Cheng, Y. B.; Spiccia, L. A Fast Deposition-Crystallization Procedure for Highly Efficient Lead Iodide Perovskite Thin-Film Solar Cells. *Angewandte Chemie - International Edition* **2014**, *53* (37), 9898–9903. https://doi.org/10.1002/anie.201405334.

(94) Jeon, N. J.; Noh, J. H.; Kim, Y. C.; Yang, W. S.; Ryu, S.; Seok, S. il. Solvent Engineering for High-Performance Inorganic-Organic Hybrid Perovskite Solar Cells. *Nature Materials* **2014**, *13* (9), 897–903. https://doi.org/10.1038/nmat4014.

(95) Jeon, N. J.; Noh, J. H.; Yang, W. S.; Kim, Y. C.; Ryu, S.; Seo, J.; Seok, S. il. Compositional Engineering of Perovskite Materials for High-Performance Solar Cells. *Nature* **2015**, *517* (7535), 476–480. https://doi.org/10.1038/nature14133.

(96) Liang, P. W.; Liao, C. Y.; Chueh, C. C.; Zuo, F.; Williams, S. T.; Xin, X. K.; Lin, J.; Jen, A. K. Y. Additive Enhanced Crystallization of Solution-Processed Perovskite for Highly Efficient Planar-Heterojunction Solar Cells. *Advanced Materials* **2014**, *26* (22), 3748–3754. https://doi.org/10.1002/adma.201400231.

(97) Dunham, B.; Vattipalli, V.; Dimitrakopoulos, C. Evaporation-Induced Self-Assembly of Semi-Crystalline PbI2(DMSO) Complex Films as a Facile Route to Reproducible and Efficient Planar p-i-n Perovskite Solar Cells. In *MRS Advances*; Materials Research Society, 2018; Vol. 3, pp 1807–1817. https://doi.org/10.1557/adv.2018.137.

(98) Xiao, Z.; Bi, C.; Shao, Y.; Dong, Q.; Wang, Q.; Yuan, Y.; Wang, C.; Gao, Y.; Huang, J. Efficient High Yield Perovskite Photovoltaic Devices Grown by Interdiffustion of Solution-Processed Precursor Stacking Layers.Pdf. **2014**, 1–4.

(99) Wu, Y.; Islam, A.; Yang, X.; Qin, C.; Liu, J.; Zhang, K.; Peng, W.; Han, L. Retarding the Crystallization of PbI2 for Highly Reproducible Planar-Structured Perovskite Solar Cells via Sequential Deposition. *Energy and Environmental Science* **2014**, *7* (9), 2934–2938. https://doi.org/10.1039/c4ee01624f.

(100) Li, W.; Fan, J.; Li, J.; Mai, Y.; Wang, L. Controllable Grain Morphology of Perovskite Absorber Film by Molecular Self-Assembly toward Efficient Solar Cell Exceeding 17%. *Journal of the American Chemical Society* **2015**, *137* (32), 10399–10405. https://doi.org/10.1021/jacs.5b06444.

(101) Chiang, C. H.; Tseng, Z. L.; Wu, C. G. Planar Heterojunction Perovskite/PC71BM Solar Cells with Enhanced Open-Circuit Voltage via a (2/1)-Step Spin-Coating Process. *Journal of Materials Chemistry A* **2014**, *2* (38), 15897–15903. https://doi.org/10.1039/c4ta03674c.

(102) Yang, W. S.; Noh, J. H.; Jeon, N. J.; Kim, Y. C.; Ryu, S.; Seo, J.; Seok, S. il. High-Performance Photovoltaic Perovskite Layers Fabricated through Intramolecular Exchange. *Science* **2015**, *348* (6240), 1234–1237. https://doi.org/10.1126/science.aaa9272.

(103) Jo, Y.; Oh, K. S.; Kim, M.; Kim, K. H.; Lee, H.; Lee, C. W.; Kim, D. S. High Performance of Planar Perovskite Solar Cells Produced from PbI 2 (DMSO) and PbI 2 (NMP) Complexes by Intramolecular Exchange. *Advanced Materials Interfaces* **2016**, *3* (10). https://doi.org/10.1002/admi.201500768.

(104) Docampo, P.; Ball, J. M.; Darwich, M.; Eperon, G. E.; Snaith, H. J. Efficient Organometal Trihalide Perovskite Planar-Heterojunction Solar Cells on Flexible Polymer Substrates. *Nature Communications* **2013**, *4*, 1–6. https://doi.org/10.1038/ncomms3761.

(105) You, J.; Hong, Z.; Yang, Y. M.; Chen, Q.; Cai, M.; Song, T.; Chen, C. Perovskite Solar Cells with High E Ffi Ciency and Flexibility. **2014**, No. Xx.

(106) Heo, J. H.; Han, H. J.; Kim, D.; Ahn, T. K.; Im, S. H. Hysteresis-Less Inverted CH<inf>3</Inf>NH<inf>3</Inf>PbI<inf>3</Inf> Planar Perovskite Hybrid Solar Cells with 18.1% Power Conversion Efficiency. *Energy and Environmental Science* **2015**, *8* (5), 1602–1608. https://doi.org/10.1039/c5ee00120j.

(107) Wu, C. G.; Chiang, C. H.; Tseng, Z. L.; Nazeeruddin, M. K.; Hagfeldt, A.; Grätzel, M. High Efficiency Stable Inverted Perovskite Solar Cells without Current Hysteresis. *Energy and Environmental Science* **2015**, *8* (9), 2725–2733. https://doi.org/10.1039/c5ee00645g.

(108) Bag, M.; Renna, L. A.; Adhikari, R. Y.; Karak, S.; Liu, F.; Lahti, P. M.; Russell, T. P.; Tuominen, M. T.; Venkataraman, D. Kinetics of Ion Transport in Perovskite Active Layers and Its Implications for Active Layer Stability. *Journal of the American Chemical Society* **2015**, *137* (40), 13130–13137. https://doi.org/10.1021/jacs.5b08535.

(109) Xue, Q.; Hu, Z.; Liu, J.; Lin, J.; Sun, C.; Chen, Z.; Duan, C.; Wang, J.; Liao, C.; Lau, W. M.; et al. Highly Efficient Fullerene/Perovskite Planar Heterojunction Solar Cells via Cathode Modification with an Amino-Functionalized Polymer Interlayer. *Journal of Materials Chemistry A* **2014**, *2* (46), 19598–19603. https://doi.org/10.1039/c4ta05352d.

(110) Min, J.; Zhang, Z. G.; Hou, Y.; Quiroz, C. O. R.; Przybilla, T.; Bronnbauer, C.; Guo, F.; Forberich, K.; Azimi, H.; Ameri, T.; et al. Interface Engineering of Perovskite Hybrid Solar Cells with Solution-Processed Perylene-Diimide Heterojunctions toward High Performance. *Chemistry of Materials* **2015**, *27* (1), 227–234. https://doi.org/10.1021/cm5037919.

(111) Liu, Y.; Bag, M.; Renna, L. A.; Page, Z. A.; Kim, P.; Emrick, T.; Venkataraman, D.; Russell, T. P. Understanding Interface Engineering for High-Performance Fullerene/Perovskite Planar Heterojunction Solar Cells. *Advanced Energy Materials* **2016**, *6* (2), 1–7. https://doi.org/10.1002/aenm.201501606.

(112) Wu, Y.; Islam, A.; Yang, X.; Qin, C.; Liu, J.; Zhang, K.; Peng, W.; Han, L. Retarding the Crystallization of {PbI} {\textbackslash}textlesssub{\textbackslash}textgreater2{\textbackslash}textless/Sub{\textbackslash}textgreater for Highly Reproducible Planar-Structured Perovskite Solar Cells via Sequential Deposition. *Energy Environ. Sci.* **2014**, *7* (9), 2934. https://doi.org/10.1039/C4EE01624F.

(113) Li, W.; Fan, J.; Li, J.; Mai, Y.; Wang, L. Supporting Information Film by Molecular Self-Assembly toward Efficient Solar Cell. 1–5.

(114) Scharber, M. C.; Sariciftci, N. S. Efficiency of Bulk-Heterojunction Organic Solar Cells. *Progress in Polymer Science*. December 2013, pp 1929–1940. https://doi.org/10.1016/j.progpolymsci.2013.05.001.

(115) Khan, T. M.; Zhou, Y.; Dindar, A.; Shim, J. W.; Fuentes-Hernandez, C.; Kippelen, B. Organic Photovoltaic Cells with Stable Top Metal Electrodes Modified with Polyethylenimine. In *ACS Applied Materials and Interfaces*; American Chemical Society, 2014; Vol. 6, pp 6202–6207. https://doi.org/10.1021/am501236z.

(116) Liu, T.; Chen, K.; Hu, Q.; Zhu, R.; Gong, Q. Inverted Perovskite Solar Cells: Progresses and Perspectives. *Advanced Energy Materials* **2016**, *6* (17). https://doi.org/10.1002/aenm.201600457.

(117) Krebs, F. C. Polymer Solar Cell Modules Prepared Using Roll-to-Roll Methods: Knife-over-Edge Coating, Slot-Die Coating and Screen Printing. *Solar Energy Materials and Solar Cells* **2009**, *93* (4), 465–475. https://doi.org/10.1016/j.solmat.2008.12.012.

(118) Krebs, F. C.; Gevorgyan, S. A.; Alstrup, J. A Roll-to-Roll Process to Flexible Polymer Solar Cells: Model Studies, Manufacture and Operational Stability Studies. *Journal of Materials Chemistry* **2009**, *19* (30), 5442–5451. https://doi.org/10.1039/b823001c.

(119) Guo, F.; Zhu, X.; Forberich, K.; Krantz, J.; Stubhan, T.; Salinas, M.; Halik, M.; Spallek, S.; Butz, B.; Spiecker, E.; et al. ITO-Free and Fully Solution-Processed Semitransparent Organic Solar Cells with High Fill Factors. *Advanced Energy Materials* **2013**, *3* (8), 1062–1067. https://doi.org/10.1002/aenm.201300100.

(120) Yip, H. L.; Jen, A. K. Y. Recent Advances in Solution-Processed Interfacial Materials for Efficient and Stable Polymer Solar Cells. *Energy and Environmental Science* **2012**, *5* (3), 5994–6011. https://doi.org/10.1039/c2ee02806a.

(121) Duan, C.; Zhang, K.; Zhong, C.; Huang, F.; Cao, Y. Recent Advances in Water/Alcohol-Soluble π-Conjugated Materials: New Materials and Growing Applications in Solar Cells. *Chemical Society Reviews*. Royal Society of Chemistry December 7, 2013, pp 9071–9104. https://doi.org/10.1039/c3cs60200a.

(122) Gu, C.; Chen, Y.; Zhang, Z.; Xue, S.; Sun, S.; Zhong, C.; Zhang, H.; Lv, Y.; Li, F.; Huang, F.; et al. Achieving High Efficiency of PTB7-Based Polymer Solar Cells via Integrated Optimization of Both Anode and Cathode Interlayers. *Advanced Energy Materials* **2014**, *4* (8). https://doi.org/10.1002/aenm.201301771.

(123) Page, Z. A.; Liu, Y.; Duzhko, V. v.; Russell, T. P.; Emrick, T. Fulleropyrrolidine Interlayers: Tailoring Electrodes to Raise Organic Solar Cell Efficiency. *Science* **2014**, *346* (6208), 441–444. https://doi.org/10.1126/science.1255826.

(124) Page, Z. A.; Liu, Y.; Duzhko, V. v.; Russell, T. P.; Emrick, T. Fulleropyrrolidine Interlayers: Tailoring Electrodes to Raise Organic Solar Cell Efficiency. *Science* **2014**, *346* (6208), 441–444. https://doi.org/10.1126/science.1255826.

(125) Duzhko, V. v.; Dunham, B.; Rosa, S. J.; Cole, M. D.; Paul, A.; Page, Z. A.; Dimitrakopoulos, C.; Emrick, T. N-Doped Zwitterionic Fullerenes as Interlayers in Organic and Perovskite Photovoltaic Devices. *ACS Energy Letters* **2017**, *2* (5), 957–963. https://doi.org/10.1021/acsenergylett.7b00147.

(126) Chang, S. H.; Lin, K. F.; Chiu, K. Y.; Tsai, C. L.; Cheng, H. M.; Yeh, S. C.; Wu, W. T.; Chen, W. N.; Chen, C. T.; Chen, S. H.; et al. Improving the Efficiency of CH3NH3PbI3 Based Photovoltaics by Tuning the Work Function of the PEDOT: PSS Hole Transport Layer. *Solar Energy* **2015**, *122*, 892–899. https://doi.org/10.1016/j.solener.2015.10.018.

(127) Stöcker, T.; Köhler, A.; Moos, R. Why Does the Electrical Conductivity in PEDOT:PSS Decrease with PSS Content? A Study Combining Thermoelectric Measurements with Impedance Spectroscopy. *Journal of Polymer Science, Part B: Polymer Physics* **2012**, *50* (14), 976–983. https://doi.org/10.1002/polb.23089.

(128) Zhou, J.; Anjum, D. H.; Chen, L.; Xu, X.; Ventura, I. A.; Jiang, L.; Lubineau, G. The Temperature-Dependent Microstructure of PEDOT/PSS Films: Insights from Morphological, Mechanical and Electrical Analyses. *Journal of Materials Chemistry C* **2014**, *2* (46), 9903–9910. https://doi.org/10.1039/c4tc01593b.

(129) Hu, L.; Li, M.; Yang, K.; Xiong, Z.; Yang, B.; Wang, M.; Tang, X.; Zang, Z.; Liu, X.; Li, B.; et al. PEDOT:PSS Monolayers to Enhance the Hole Extraction and Stability of Perovskite Solar Cells. *Journal of Materials Chemistry A* **2018**, *6* (34), 16583–16589. https://doi.org/10.1039/c8ta05234d.

(130) Suzuki, A.; Kida, T.; Takagi, T.; Oku, T. Effects of Hole-Transporting Layers of Perovskite-Based Solar Cells. *Japanese Journal of Applied Physics* **2016**, *55* (2). https://doi.org/10.7567/JJAP.55.02BF01.

(131) Bai, Y.; Dong, Q.; Shao, Y.; Deng, Y.; Wang, Q.; Shen, L.; Wang, D.; Wei, W.; Huang, J. Enhancing Stability and Efficiency of Perovskite Solar Cells with Crosslinkable Silane-Functionalized and Doped Fullerene. *Nature Communications* **2016**, *7*. https://doi.org/10.1038/ncomms12806.

(132) Serpetzoglou, E.; Konidakis, I.; Kakavelakis, G.; Maksudov, T.; Kymakis, E.; Stratakis, E. Improved Carrier Transport in Perovskite Solar Cells Probed by Femtosecond Transient Absorption Spectroscopy. *ACS Applied Materials and Interfaces* **2017**, *9* (50), 43910–43919. https://doi.org/10.1021/acsami.7b15195.

(133) Wang, Q.; Bi, C.; Huang, J. Doped Hole Transport Layer for Efficiency Enhancement in Planar Heterojunction Organolead Trihalide Perovskite Solar Cells. *Nano Energy* **2015**, *15*, 275–280. https://doi.org/10.1016/j.nanoen.2015.04.029.

(134) Xu, X.; Ma, C.; Cheng, Y.; Xie, Y. M.; Yi, X.; Gautam, B.; Chen, S.; Li, H. W.; Lee, C. S.; So, F.; et al. Ultraviolet-Ozone Surface Modification for Non-Wetting Hole Transport Materials Based Inverted Planar Perovskite Solar Cells with Efficiency Exceeding 18%. *Journal of Power Sources* **2017**, *360*, 157–165. https://doi.org/10.1016/j.jpowsour.2017.06.013.

(135) Arabpour Roghabadi, F.; Ahmadi, N.; Ahmadi, V.; di Carlo, A.; Oniy Aghmiuni, K.; Shokrolahzadeh Tehrani, A.; Ghoreishi, F. S.; Payandeh, M.; Mansour Rezaei Fumani, N. Bulk Heterojunction Polymer Solar Cell and Perovskite Solar Cell: Concepts, Materials, Current Status, and Opto-Electronic Properties. *Solar Energy*. Elsevier Ltd October 1, 2018, pp 407–424. https://doi.org/10.1016/j.solener.2018.07.058.

(136) Gatti, T.; Casaluci, S.; Prato, M.; Salerno, M.; di Stasio, F.; Ansaldo, A.; Menna, E.; di Carlo, A.; Bonaccorso, F. Boosting Perovskite Solar Cells Performance and Stability through Doping a Poly-3(Hexylthiophene) Hole Transporting Material with Organic Functionalized Carbon Nanostructures. *Advanced Functional Materials* **2016**, *26* (41), 7443–7453. https://doi.org/10.1002/adfm.201602803.

(137) Heo, J. H.; Im, S. H.; Noh, J. H.; Mandal, T. N.; Lim, C. S.; Chang, J. A.; Lee, Y. H.; Kim, H. J.; Sarkar, A.; Nazeeruddin, M. K.; et al. Efficient Inorganic-Organic Hybrid Heterojunction Solar Cells Containing Perovskite Compound and Polymeric Hole Conductors. *Nature Photonics* **2013**, *7* (6), 486–491. https://doi.org/10.1038/nphoton.2013.80.

(138) Abdollahi Nejand, B.; Ahmadi, V.; Shahverdi, H. R. New Physical Deposition Approach for Low Cost Inorganic Hole Transport Layer in Normal Architecture of

Durable Perovskite Solar Cells. *ACS Applied Materials and Interfaces* **2015**, *7* (39), 21807–21818. https://doi.org/10.1021/acsami.5b05477.

(139) Gharibzadeh, S.; Nejand, B. A.; Moshaii, A.; Mohammadian, N.; Alizadeh, A. H.; Mohammadpour, R.; Ahmadi, V.; Alizadeh, A. Two-Step Physical Deposition of a Compact Cui Hole-Transport Layer and the Formation of an Interfacial Species in Perovskite Solar Cells. *ChemSusChem* **2016**, *9* (15), 1929–1937. https://doi.org/10.1002/cssc.201600132.

(140) Nejand, B. A.; Ahmadi, V.; Gharibzadeh, S.; Shahverdi, H. R. Cuprous Oxide as a Potential Low-Cost Hole-Transport Material for Stable Perovskite Solar Cells. *ChemSusChem* **2016**, *9* (3), 302–313. https://doi.org/10.1002/cssc.201501273.

(141) Zuo, C.; Ding, L. Solution-Processed Cu2O and CuO as Hole Transport Materials for Efficient Perovskite Solar Cells. *Small* **2015**, *11* (41), 5528–5532. https://doi.org/10.1002/smll.201501330.

(142) Jung, M.; Kim, Y. C.; Jeon, N. J.; Yang, W. S.; Seo, J.; Noh, J. H.; il Seok, S. Thermal Stability of CuSCN Hole Conductor-Based Perovskite Solar Cells. *ChemSusChem* **2016**, *9* (18), 2592–2596. https://doi.org/10.1002/cssc.201600957.

(143) Yang, I. S.; Sohn, M. R.; Sung, S. do; Kim, Y. J.; Yoo, Y. J.; Kim, J.; Lee, W. I. Formation of Pristine CuSCN Layer by Spray Deposition Method for Efficient Perovskite Solar Cell with Extended Stability. *Nano Energy* **2017**, *32*, 414–421. https://doi.org/10.1016/j.nanoen.2016.12.059.

(144) Sun, W.; Ye, S.; Rao, H.; Li, Y.; Liu, Z.; Xiao, L.; Chen, Z.; Bian, Z.; Huang, C. Room-Temperature and Solution-Processed Copper Iodide as the Hole Transport Layer for Inverted Planar Perovskite Solar Cells. *Nanoscale* **2016**, *8* (35), 15954–15960. https://doi.org/10.1039/c6nr04288k.

(145) Christians, J. A.; Fung, R. C. M.; Kamat, P. v. An Inorganic Hole Conductor for Organo-Lead Halide Perovskite Solar Cells. Improved Hole Conductivity with Copper Iodide. *Journal of the American Chemical Society* **2014**, *136* (2), 758–764. https://doi.org/10.1021/ja411014k.

(146) Zhao, K.; Munir, R.; Yan, B.; Yang, Y.; Kim, T.; Amassian, A. Solution-Processed Inorganic Copper (I) Thiocyanate (CuSCN) Hole Transporting Layer for Efficient p-i-n Perovskite Solar Cells. **2015**, No. I, 1–3.

(147) Chen, W. Y.; Deng, L. L.; Dai, S. M.; Wang, X.; Tian, C. B.; Zhan, X. X.; Xie, S. Y.; Huang, R. bin; Zheng, L. S. Low-Cost Solution-Processed Copper Iodide as an Alternative to PEDOT:PSS Hole Transport Layer for Efficient and Stable Inverted Planar Heterojunction Perovskite Solar Cells. *Journal of Materials Chemistry A* **2015**, *3* (38), 19353–19359. https://doi.org/10.1039/c5ta05286f.

(148) Hu, W. D.; Dall'Agnesel, C.; Wang, X. F.; Chen, G.; Li, M. Z.; Song, J. X.; Wei, Y. J.; Miyasaka, T. Copper Iodide-PEDOT:PSS Double Hole Transport

Layers for Improved Efficiency and Stability in Perovskite Solar Cells. *Journal of Photochemistry and Photobiology A: Chemistry* **2018**, *357*, 36–40. https://doi.org/10.1016/j.jphotochem.2018.02.018.

(149) Luo, W.; Zeng, C.; Du, X.; Leng, C.; Yao, W.; Shi, H.; Wei, X.; Du, C.; Lu, S. Copper Thiocyanate/Copper Iodide Based Hole Transport Composites with Balanced Properties for Efficient Polymer Light-Emitting Diodes. *Journal of Materials Chemistry C* **2018**, *6* (18), 4895–4902. https://doi.org/10.1039/c7tc04842d.

(150) Noh, J. H.; Im, S. H.; Heo, J. H.; Mandal, T. N.; Seok, S. il. Chemical Management for Colorful, Efficient, and Stable Inorganic-Organic Hybrid Nanostructured Solar Cells. *Nano Letters* **2013**, *13* (4), 1764–1769. https://doi.org/10.1021/nl400349b.

(151) Frost, J. M.; Butler, K. T.; Brivio, F.; Hendon, C. H.; van Schilfgaarde, M.; Walsh, A. Atomistic Origins of High-Performance in Hybrid Halide Perovskite Solar Cells. *Nano Letters* **2014**, *14* (5), 2584–2590. https://doi.org/10.1021/nl500390f.

(152) Manser, J. S.; Saidaminov, M. I.; Christians, J. A.; Bakr, O. M.; Kamat, P. v. Making and Breaking of Lead Halide Perovskites. *Accounts of Chemical Research* **2016**, *49* (2), 330–338. https://doi.org/10.1021/acs.accounts.5b00455.

(153) Christians, J. A.; Miranda Herrera, P. A.; Kamat, P. v. Transformation of the Excited State and Photovoltaic Efficiency of CH3NH3PbI3 Perovskite upon Controlled Exposure to Humidified Air. *Journal of the American Chemical Society* **2015**, *137* (4), 1530–1538. https://doi.org/10.1021/ja511132a.

(154) Philippe, B.; Park, B. W.; Lindblad, R.; Oscarsson, J.; Ahmadi, S.; Johansson, E. M. J.; Rensmo, H. Chemical and Electronic Structure Characterization of Lead Halide Perovskites and Stability Behavior under Different Exposures-A Photoelectron Spectroscopy Investigation. *Chemistry of Materials* **2015**, *27* (5), 1720–1731. https://doi.org/10.1021/acs.chemmater.5b00348.

(155) Supasai, T.; Rujisamphan, N.; Ullrich, K.; Chemseddine, A.; Dittrich, T. Formation of a Passivating CH 3 NH 3 PbI 3 /PbI 2 Interface during Moderate Heating of CH 3 NH 3 PbI 3 Layers. *Applied Physics Letters* **2013**, *103* (18), 1–4. https://doi.org/10.1063/1.4826116.

(156) Qin, C.; Matsushima, T.; Fujihara, T.; Potscavage, W. J.; Adachi, C. Degradation Mechanisms of Solution-Processed Planar Perovskite Solar Cells: Thermally Stimulated Current Measurement for Analysis of Carrier Traps. *Advanced Materials* **2016**, *28* (3), 466–471. https://doi.org/10.1002/adma.201502610.

(157) Leijtens, T.; Eperon, G. E.; Pathak, S.; Abate, A.; Lee, M. M.; Snaith, H. J. Overcoming Ultraviolet Light Instability of Sensitized TiO2 with Meso-Superstructured Organometal Tri-Halide Perovskite Solar Cells. *Nature Communications* **2013**, *4*, 1–8. https://doi.org/10.1038/ncomms3885.

(158) Aristidou, N.; Sanchez-Molina, I.; Chotchuangchutchaval, T.; Brown, M.; Martinez, L.; Rath, T.; Haque, S. A. The Role of Oxygen in the Degradation of Methylammonium Lead Trihalide Perovskite Photoactive Layers. *Angewandte Chemie - International Edition* **2015**, *54* (28), 8208–8212. https://doi.org/10.1002/anie.201503153.

(159) Smith, E. C.; Ellis, C. L. C.; Javaid, H.; Renna, L. A.; Liu, Y.; Russell, T. P.; Bag, M.; Venkataraman, D. Interplay between Ion Transport, Applied Bias, and Degradation under Illumination in Hybrid Perovskite p-i-n Devices. *Journal of Physical Chemistry C* **2018**, *122* (25), 13986–13994. https://doi.org/10.1021/acs.jpcc.8b01121.

(160) Novoselov, K. S.; Geim, A. K.; Morozov, S. v.; Jiang, D.; Zhang, Y.; Dubonos, S. v.; Grigorieva, I. v.; Firsov, A. A. Electric Field in Atomically Thin Carbon Films. *Science* **2004**, *306* (5696), 666–669. https://doi.org/10.1126/science.1102896.

(161) Liu, Z.; You, P.; Xie, C.; Tang, G.; Yan, F. Ultrathin and Flexible Perovskite Solar Cells with Graphene Transparent Electrodes. *Nano Energy* **2016**, *28*, 151–157. https://doi.org/10.1016/j.nanoen.2016.08.038.

(162) Chen, S.; Brown, L.; Levendorf, M.; Cai, W.; Ju, S. Y.; Edgeworth, J.; Li, X.; Magnuson, C. W.; Velamakanni, A.; Piner, R. D.; et al. Oxidation Resistance of Graphene-Coated Cu and Cu/Ni Alloy. *ACS Nano* **2011**, *5* (2), 1321–1327. https://doi.org/10.1021/nn103028d.

(163) Wang, G.; Kim, Y.; Choe, M.; Kim, T. W.; Lee, T. A New Approach for Molecular Electronic Junctions with a Multilayer Graphene Electrode. *Advanced Materials* **2011**, *23* (6), 755–760. https://doi.org/10.1002/adma.201003178.

(164) Bae, S.; Kim, H.; Lee, Y.; Xu, X.; Park, J. S.; Zheng, Y.; Balakrishnan, J.; Lei, T.; Ri Kim, H.; Song, Y. il; et al. Roll-to-Roll Production of 30-Inch Graphene Films for Transparent Electrodes. *Nature Nanotechnology* **2010**, *5* (8), 574–578. https://doi.org/10.1038/nnano.2010.132.

(165) Kidambi, P. R.; Mariappan, D. D.; Dee, N. T.; Vyatskikh, A.; Zhang, S.; Karnik, R.; Hart, A. J. A Scalable Route to Nanoporous Large-Area Atomically Thin Graphene Membranes by Roll-to-Roll Chemical Vapor Deposition and Polymer Support Casting. *ACS Applied Materials and Interfaces* **2018**, *10* (12), 10369–10378. https://doi.org/10.1021/acsami.8b00846.

(166) Reina, A.; Jia, X.; Ho, J.; Nezich, D.; Son, H.; Bulovic, V.; Dresselhaus, M. S.; Jing, K. Large Area, Few-Layer Graphene Films on Arbitrary Substrates by Chemical Vapor Deposition. *Nano Letters* **2009**, *9* (1), 30–35. https://doi.org/10.1021/nl801827v.

(167) Dong, X.; Wang, P.; Fang, W.; Su, C. Y.; Chen, Y. H.; Li, L. J.; Huang, W.; Chen, P. Growth of Large-Sized Graphene Thin-Films by Liquid Precursor-Based Chemical Vapor Deposition under Atmospheric Pressure. *Carbon* **2011**, *49* (11), 3672–3678. https://doi.org/10.1016/j.carbon.2011.04.069.

(168) Barin, G. B.; Song, Y.; Gimenez, I. D. F.; Filho, A. G. S.; Barreto, L. S.; Kong, J. Optimized Graphene Transfer: Influence of Polymethylmethacrylate (PMMA) Layer Concentration and Baking Time on Grapheme Final Performance. *Carbon* **2015**, *84* (C), 82–90. https://doi.org/10.1016/j.carbon.2014.11.040.

(169) Auchter, E.; Marquez, J.; Yarbro, S. L.; Dervishi, E. A Facile Alternative Technique for Large-Area Graphene Transfer via Sacrificial Polymer. *AIP Advances* **2017**, *7* (12). https://doi.org/10.1063/1.4986780.

(170) Shao, Y.; Xiao, Z.; Bi, C.; Yuan, Y.; Huang, J. Origin and Elimination of Photocurrent Hysteresis by Fullerene Passivation in CH3NH3PbI3 Planar Heterojunction Solar Cells. *Nature Communications* **2014**, *5*, 1–7. https://doi.org/10.1038/ncomms6784.

(171) Arora, N.; Dar, M. I.; Hinderhofer, A.; Pellet, N.; Schreiber, F.; Zakeeruddin, S. M.; Grätzel, M. Perovskite Solar Cells with CuSCN Hole Extraction Layers Yield Stabilized Efficiencies Greater than 20%. *Science* **2017**, *358* (6364), 768–771. https://doi.org/10.1126/science.aam5655.